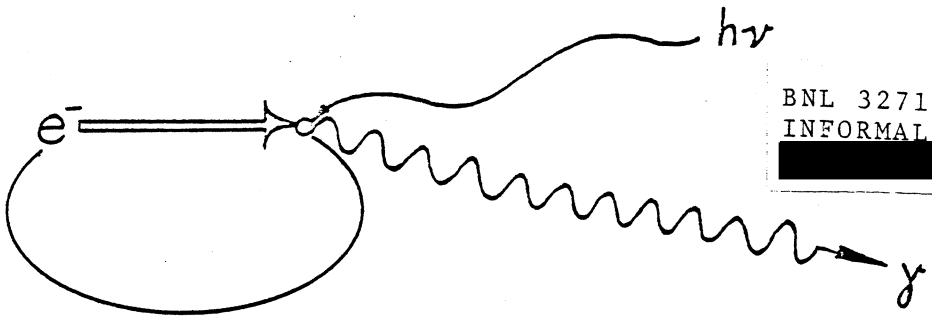

BNL 32717
INFORMAL REPORT

A PROPOSAL

TO THE DEPARTMENT OF ENERGY

FOR

THE FABRICATION OF A VERY HIGH ENERGY POLARIZED GAMMA RAY BEAM FACILITY AND A PROGRAM OF MEDIUM ENERGY PHYSICS RESEARCH AT THE NATIONAL SYNCHROTRON LIGHT SOURCE

Department of Physics
Brookhaven National Laboratory, Upton, New York 11973

(September 1982)

CONTRIBUTORS

A.M.Sandorfi
M.J.LeVine
C.E.Thorn
G.Giordano
G.Matone

DISCLAIMER

This report was prepared as an account of work sponsored by an agency of the United States Government. Neither the United States Government nor any agency thereof, nor any of their employees, nor any of their contractors, subcontractors, or their employees makes any warranty, express or implied, or assumes any legal liability or responsibility for the accuracy, completeness, or usefulness of any information, apparatus, product or process disclosed, or represents that its use would not infringe privately owned rights. Reference herein to any specific commercial product, process, or service by trade name, trademark, manufacturer, or otherwise, does not necessarily constitute or imply its endorsement, recommendation, or favoring by the United States Government or any agency thereof. The views and opinions of authors expressed herein do not necessarily state or reflect those of the United States Government or any agency, contractor, or subcontractor thereof.

ABSTRACT

This proposal requests support for the fabrication and operation of a modest facility that would provide relatively intense beams of monochromatic and polarized photons with energies in the range of several hundreds of MeV. These γ rays would be produced by Compton backscattering laser light from the electrons circulating in the 2.5-3.0 GeV "X-RAY" storage ring of the National Synchrotron Light Source (NSLS) at Brookhaven National Laboratory. The excellent emittance, phase space, and high current of this state-of-the-art storage ring will allow the production of 2×10^7 γ rays per second. These photons would be tagged by detecting the scattered electrons, thereby determining the energy to 2.7 MeV for all γ-ray energies. The efficiency of this tagging procedure is 100% and the γ-ray beam would be essentially background free. Tagging will also allow the flexibility of operating with a dynamic range as large as 200 MeV in photon energy while still preserving high resolution and polarization. These beams will permit a fruitful study of important questions in medium-energy nuclear physics. The initial goals of this program are to reach reliable operation with photon energies up to 300 MeV and to develop γ-ray beams with energies up to about 500 MeV. To demonstrate reliable operation, a modest physics program is planned that, for the most part, utilizes existing magnets and detector systems but nonetheless addresses several important outstanding problems. Gamma ray beams of the versatility, intensity, energy, and resolution that can be achieved at this facility are not currently available at any other world facility either existing or under construction.

Furthermore, the proposed program would produce the first intense source of medium-energy γ rays that are polarized. Because of the difficulties in producing such polarized beams, it is very unlikely that viable alternate sources can be developed in the near future; at present, no others are planned.

TABLE OF CONTENTS

I. Introduction

The proposed facility would be capable of producing fluxes of 2×10^7 polarized (linearly or circularly) and monochromatic γ rays per second in the energy range of 100 to 500 MeV. The technical considerations involved in producing these γ rays by backscattering laser light from high energy electrons are discussed in Sections II and III. The different modes of operation that can produce these γ ray fluxes are discussed in Section III, and the initial Medium Energy physics program demonstrating the versatility of these γ ray beams is outlined in Section IV. Capital and operating costs, along with the time schedule for construction, are given in Section V. The general motivation for and phases in the development of this γ ray facility are now summarized below. The scientific personnel involved in the development of the facility are listed at the end of this section.

I.1 General Scientific Justification

During the past few years there have been several studies and many conferences* devoted exclusively to outlining the important questions that should be addressed in electro- and photo-nuclear

*See, for example:

1) Proc. of the "Symposium on Perspectives in Electro- and Photo-Nuclear Physics", Saclay (1980); available as Nucl. Phys. A358 (1981).

2) Proc. of the Workshop on "Intermediate Energy Nuclear Physics with Monochromatic and Polarized Photons", Frascati (1980); available from Frascati National Laboratories.

3) Report of the Workshop on "Future Directions in Electromagnetic Nuclear Physics" (1981); available from the Physics department at the Massachusetts Institute of Technology.

physics over the next one or two decades. A conclusion common to all of these studies is that a very high-energy, high-duty factor electron accelerator would provide the maximum versatility for research in this field. A large subset of these important problems can be studied with real photons, and in fact all conceptual designs of this new electron facility include a bremsstrahlung monochromator for producing high resolution γ-ray beams. This is in part because of a general desire to have complementary measurements with both real and virtual photons, but is also because there is a large class of problems for which the real photon is in fact a better probe. Studies in this class make use of the fact that the form factor for photon interactions is significantly different from that for electron interactions. (For example, in the term dominating the electron scattering form factor, the matrix elements are multiplied by $e \cdot e_i$, where e is the electron charge and e_i is the charge of a nuclear constituent. When summed over i, the contributions from negative and positive virtual pions nearly cancel. In contrast, the matrix elements in the dominant term of high-energy photon scattering are multiplied by e_i^2 so that the effects of negative and positive pions add.) This difference between photons and electrons, combined with the simplicity of the electromagnetic probe, proves advantageous in a number of areas. For example:

(1) Recent calculations (Bo81) have suggested that about one-half of the Gamow-Teller sum rule strength, which appears to be missing from the low-lying giant resonance, may be absorbed in a giant collective nuclear-delta excitation. In reaction channels, a

broad peak in the region of the delta is always expected from purely single-nucleon excitations, and collective enhancements would be extremely difficult to disentangle. However, the form factor for elastic photon scattering is quite sensitive to collective effects, and the cross sections at large angles can change by up to two orders of magnitude if a "giant" component is present in the region of the delta (Le81).

(2) In the region below the delta (E_γ~200 MeV), meson exchange currents are expected to enhance elastic photon scattering by more than a factor of ten (Ch80). This is principally due to the cumulative effect of scattering from the virtual pions. (Large meson effects have already been observed in photon scattering from deuterium (De81) and from ^{208}Pb (Le81) below 100 MeV.) Very high electron energies (several GeV) and coincidence measurements requiring high-duty-factor would be required to obtain a comparable sensitivity to meson currents.

(3) Because real photon interactions are so strongly affected by the pion field, photo-induced reactions, particularly (γ,π^+), have been suggested as the ideal method of searching for critical opalescence, the precursor of pion condensation (Jd80). An enhancement of the virtual pion field from such a phenomenon would, for example, increase the $^{12}C(\gamma,\pi^+)$ 90° differential cross section, for E_γ between 200 and 300 MeV, by more

than a factor of 10. Such effects are most dramatically studied with linearly polarized photons since backgrounds from competing processes can be made very small. (In particular, the seagull diagram, that containing a single $\gamma N \pi$ vertex, could interfere with the opalescence effect. However, it cannot contribute when the charged pion is emitted perpendicular to the polarization vector of the incident γ ray.)

(4) The (π^-,π^o) reaction has been used recently to uncover the first candidate for a giant-isovector-monopole resonance (Bo82), a collective mode in which neutrons and protons undergo separate density oscillations that are out of phase. In addition to the large backgrounds encountered in these experiments, the (π^-,π^o) and (π^+,π^o) cross sections, leading to the same residual nuclei, show unexpected differences. Furthermore, the isovector quadrupole resonance, which should be as strongly excited as the T=1 monopole, is completely absent from these data. The same $\Delta T=1$ modes should be strongly excited in (γ,π) reactions, and with photons the non-resonant backgrounds may be very much reduced. Furthermore, the (γ,π^+) and (γ,π^-) reactions may be used to separately excite the proton and neutron density distributions, with a mechanism that is much easier to model theoretically.

(5) The mass and lifetime of excited baryons such as the delta are strongly altered by the presence of the

nuclear medium. These alterations are caused by a number of effects which generally are difficult to isolate and study independently. However, one of these effects, rescattering, which completely dominates pion-induced reactions, can be dramatically reduced with real transverse photons (Os79). The treatment of the remaining effects within a Δ-hole model calculation is then quite sensitive to photon induced reactions. Only a very small amount of data, having very large uncertainties, has been accumulated on total photoabsorption and on the coherent (γ,π^o) process in the region of the Δ. Nonetheless, the data suggest several serious discrepancies with the Δ-hole model. In addition to putting these questions on a much firmer experimental footing, new measurements with polarized photons could provide direct information on the strength of the Δ-hole force.

(6) Several QCD calculations have independently concluded that the delta itself must be deformed and must have a sizeable (30%-50%) d-state component in its wavefunction (Br81). Electron scattering experiments on hydrogen, $H(e,e'\pi)N$, have been proposed to measure this deformation by determining the E2/M1 ratio in the region of the delta (Se81), and similar measurements with polarized photon beams have also been considered (Ga82). A recent analysis of existing data (Ga82) puts the average value of this ratio at 0.014 ± 0.016. All of

the new proposed experiments would be potentially very difficult to interpret, due to an uncertainty in calculating a recoil correction. The latter arises because, following the decay of the Δ, the moving charged pion creates an effective E2 moment that is of the same order as the moment expected from the deformation. Although the recoil correction is difficult to calculate, it may be possible to drastically reduce its contribution by transferring the minimum amount of momentum; i.e., by using elastic photon scattering $(\vec{\gamma},\gamma)$.

(7) QCD calculations also predict that 6-quark states should exist. Many of these states are expected to be of high spin and are most accessible through polarization measurements. There are several candidates for such dibaryons, but all are controversial. A recent dibaryon candidate of unprecedented narrowness (40 MeV) was reported in the disintegration of deuterium with unpolarized photons (Ar81). Measurements with polarized γ rays are needed to explore this structure and determine its spin before comparisons can be made with QCD. If this structure does indeed prove to be consistent with a dibaryon, then several other such resonances should exist and a search over a larger energy range could prove fruitful.

(8) Photon scattering from virtual electron-positron pairs, Delbrück scattering, is represented in QED as

scattering from the vacuum polarization cloud associated with the charged nucleus. The Feynman graphs for this process form a unique set of third order diagrams. Measurements at forward angles, where the Delbrück amplitudes peak, show systematic deviations from QED calculations (Pa75). A key experimental difficulty involves the separation of Delbrück scattering from other processes. However, the Delbrück amplitudes are very sensitive to the polarization of the incident photon. Small angle measurements with a polarized beam over a large range of energies would provide a unique opportunity to investigate this problem.

(9) In the Weinberg-Salam-Glashow (WSG) theory, any electromagnetic process described by the exchange of a virtual photon is accompanied by an identical diagram in which a Z_o is exchanged. The interference of this weak-neutral-current with the electromagnetic interaction is of great interest. In the absence of this interference, bremsstrahlung is completely unpolarized at 0^o and plane polarized off axis. A recent measurement of the circular polarization of 0^o bremsstrahlung generated by 300 MeV electrons, has reported a component that is two orders of magnitude larger than the WSG prediction (Zi82). Pair production by circularly polarized γ rays provides an independent yet related mechanism for studying these effects.

Measurements of the polarization asymmetry in pair production could test the WSG theory in a way that would be less sensitive to spurious asymmetry-producing sources. If the enhancements in bremsstrahlung over the WSG predictions are correct, the effect upon pair production should be quite dramatic.

The above problems, as well as many others that would be complementary to future studies with the high-energy high-duty-factor electron accelerator when it becomes available, could be addressed in the very immediate future with the proposed facility. High resolution in a flexible dynamic range would be achieved by tagging the 100 to 500 MeV γ rays produced by laser backscattering against electrons. The production mechanism permits this tagging to be 100% efficient so that, very unlike conventional tagged-bremsstrahlung, no background γ rays of unknown energy would accompany the tagged beam. The beams from the proposed facility would be greater than 90% polarized, either linearly or circularly depending upon the requirements of the experiment, and would have a flux that is comparable to if not greater than what might be achievable with a bremsstrahlung monochromator at a high duty factor electron facility. The costs involved in constructing the proposed backscattering facility are extremely minimal because the first essential part, a state-of-the-art electron storage ring, already exists, and because the other essential ingredients, the laser system and the optical cavity, are trivial compared with the cost of an accelerator.

From the above considerations it is clear that there would be a strong motivation to proceed with this facility even if the envisioned

high-energy high-duty-factor electron accelerator, together with a 100-500 MeV unpolarized bremsstrahlung monochromator*, existed today. In the absence of such an electron accelerator, the motivation is overwhelming.

*A component of plane-polarized γ rays is present in bremsstrahlung ($\theta_\gamma > 0^\circ$), but only with several orders of magnitude lower intensity than the primary beam.

I.2 Stages of Development

The development and utilization of the backscattered γ-ray beam is planned to occur in three distinct phases.

PHASE I: An existing high-powered CW Ar-Ion Laser would be used in the visible region at 5145 Å and in the UV at 3511 Å. These photons would collide with the 2.5 GeV electrons in the injection-straight-section of the NSLS X-RAY ring, producing up to 300 MeV γ rays. These γ rays would be tagged by detecting the electrons that interacted with the laser light. The tagging spectrometer consists of the existing 22.5° dipole magnet that follows the straight section and a set of septum magnets with a net dynamic range extending from 175 MeV to 300 MeV in photon energy. This system will provide a resolution of about 2.7 MeV for all γ ray energies. The polarization of the beam would be greater than 90%. The storage ring would operate in the standard (OPTICS) tune, and the tagged flux will be about 1×10^{7} photons per second. The decrease in the lifetime of the stored beam due to the laser-electron collisions represents only a small perturbation on the expected beam lifetime, so that the γ ray production operates simply as one of many passive uses of the National Synchrotron Light Source. The γ-ray beam would be studied with detectors located within the existing building at a distance of about 20 meters from the laser-electron interaction region. The development of PHASE I is expected to occupy the first year of the project with the first tagged γ-ray beam scheduled for the end of that year.

The energy range achieved in this phase encompasses the region of the nuclear delta resonance. The initial physics program thus concentrates on searching for giant delta resonances in elastic photon scattering, and on studying the modifications to the delta due to the presence of the nuclear medium via total photo-absorption measurements.

The detectors for the initial PHASE I tests and experiments are fairly compact and can be accommodated within the existing building. However, the currently available space is far too restrictive for our full medium-energy physics program which must utilize large solid-angle magnetic spectrometers.

PHASE II: A modest extension would be added to the existing NSLS building to provide adequate space for large spectrometers, electronics,and data-acquisition equipment. The construction of this 'γ-ray lab' is planned for the first half of the second year. Part of the PHASE I experimental program would continue during this period. During the final stages of construction, a new ultra-high-power Ar-Ion laser would be installed which would more than double the flux of γ rays up to 300 MeV in energy. A $\pi^{\pm}$ spectrometer and π^{o} detectors will be installed in the new γ-ray lab with the nuclear target now located about 35 meters from the laser-electron collision region.

The physics program in PHASE II will expand to include a number of new experiments, the first being the coherent $(\vec{\gamma},\pi^{o})$ reaction which

tests in some detail the ability of the delta-hole model to account for modifications to the properties of the delta in nuclear matter. The second is a search for critical opalescence in coherent $(\vec{\gamma},\pi^+)$. If the data suggest that such a phenomenon is indeed present, then further $(\vec{\gamma},\pi^o)$ measurements will be necessary to properly separate the effect of the delta. Measurements of forward angle Delbrück scattering would also be undertaken during this phase, along with an attempt to detect the effect of neutral-Z_o-currents in $(\vec{\gamma},e^+e^-)$.

PHASE III: To obtain higher energy γ-ray beams, the Free Electron Laser, mounted on the VUV Ring, will be tuned down in wavelength, initially to 2500 Å, and ultimately to about 2000 Å. These laser photons will be transported to the injection-straight section of the X-RAY Ring and will collide with 2.5 GeV electrons to produce 400 MeV and about 500 MeV γ rays, repectively. This technique is possible only at the NSLS because of the proximity of the two storage rings, and because both rings can be run from the same Rf oscillator and can thus be synchronized in time. (This mode of operation could extend the γ-ray beam energy up to about 700 MeV when the X-RAY Ring achieves 3 GeV.) The γ-ray flux obtained in PHASE III depends critically on the gain of the Free electron Laser. Present best estimates put the expected flux above 10^7 tagged photons per second. The construction of the optical transport system necessary to couple the two storage rings is scheduled for the latter part of the second year of the program. The first beam tests would take place at the end of that year. The physics program could utilize this beam during the third year.

The PHASE III beam will be used to extend the absorption measurements to 500 MeV, and to search for and study Dibaryon resonances in the $^{2}H(\vec{\gamma},p\pi^{-})p$ reaction. The latter experiment requires a liquid deuterium target. The installation of this would be completed early in the third year of the project.

I.3 Personnel

The scientific personnel who have been involved in the design of this gamma ray facility and the planned medium-energy physics program are listed below.

PRINCIPAL INVESTIGATORS

Physics Department - BNL:	A.M. Sandorfi
	M.J. LeVine
	C.E. Thorn
INFN - Frascati:	G. Giordano
	G. Matone

Additional personnel committed to an involvement in the development of this facility are:

Univ. of Rome:	C. Schaerf
Univ. of Illinois:	A.M. Nathan

We are indebted to several staff members of the National Synchrotron Light Source at BNL, particularly S. Krinsky, A. Luccio, C. Pellegrini and A. van Steenbergen, for their technical support during the design of this project. We acknowledge, in advance, their necessary and very valuable support during the development of PHASES I and II of this gamma ray facility. We look forward to their participation as collaborators in the development of the PHASE III γ ray beam which utilizes both VUV and X-RAY storage rings, simultaneously.

We are indebted to several members of the BNL physics department, particularly C. Dover and J. Weneser for many valuable suggestions toward the medium-energy physics program, and to A.Z. Schwarzschild for his enthusiastic support as Chairman of the Department. We gratefully acknowledge the continued interest of J. McTague, Head of the National Synchrotron Light Source Division, in this unique application of the NSLS electron rings.

II. High Energy γ Ray Production by Laser Backscattering from Relativistic Electrons

Collisions between relativistic electrons and visible photons from starlight had been considered as a likely source of the high energy gamma-ray components in cosmic rays as early as 1948 (Fe48). In 1963, Milburn (Mi63), and Arutyunian and Tumanian (Ar63), pointed out that the same mechanism of backward Compton scattering applied to collisions between laser light and a high-energy electron beam might produce useful yields of nearly monochromatic polarized photons.

II.1 Production Mechanism

The scattering process is shown schematically in Fig. 1. The laser photon and the electron approach each other at some small relative angle ϕ. After backscattering, the γ ray emerges at a small angle θ relative to the electron beam direction. The Lorentz transformations for arbitrary ϕ and θ are outlined in Fig. 2. In the frame in which the electron is initially at rest, the laser photon is boosted up in energy by a factor of about 2γ, where $\gamma=E_e/mc^2$. At the same time, any angular divergences in the initial laser beam or electron beam (represented by ϕ) are collapsed. In this frame the photon, now an x-ray, Compton scatters from the stationary electron. After backscattering, the x-ray is boosted up in energy by another factor of about 2γ when viewed in the laboratory. At the same time, the angular spread of the outgoing γ ray again experiences a collapse in transforming to the laboratory. The dependence of the final γ-ray energy upon angle comes chiefly from the Compton scattering process itself. For a laser of energy ε_ℓ and an electron beam of energy γmc^2, the γ-ray energy is given by

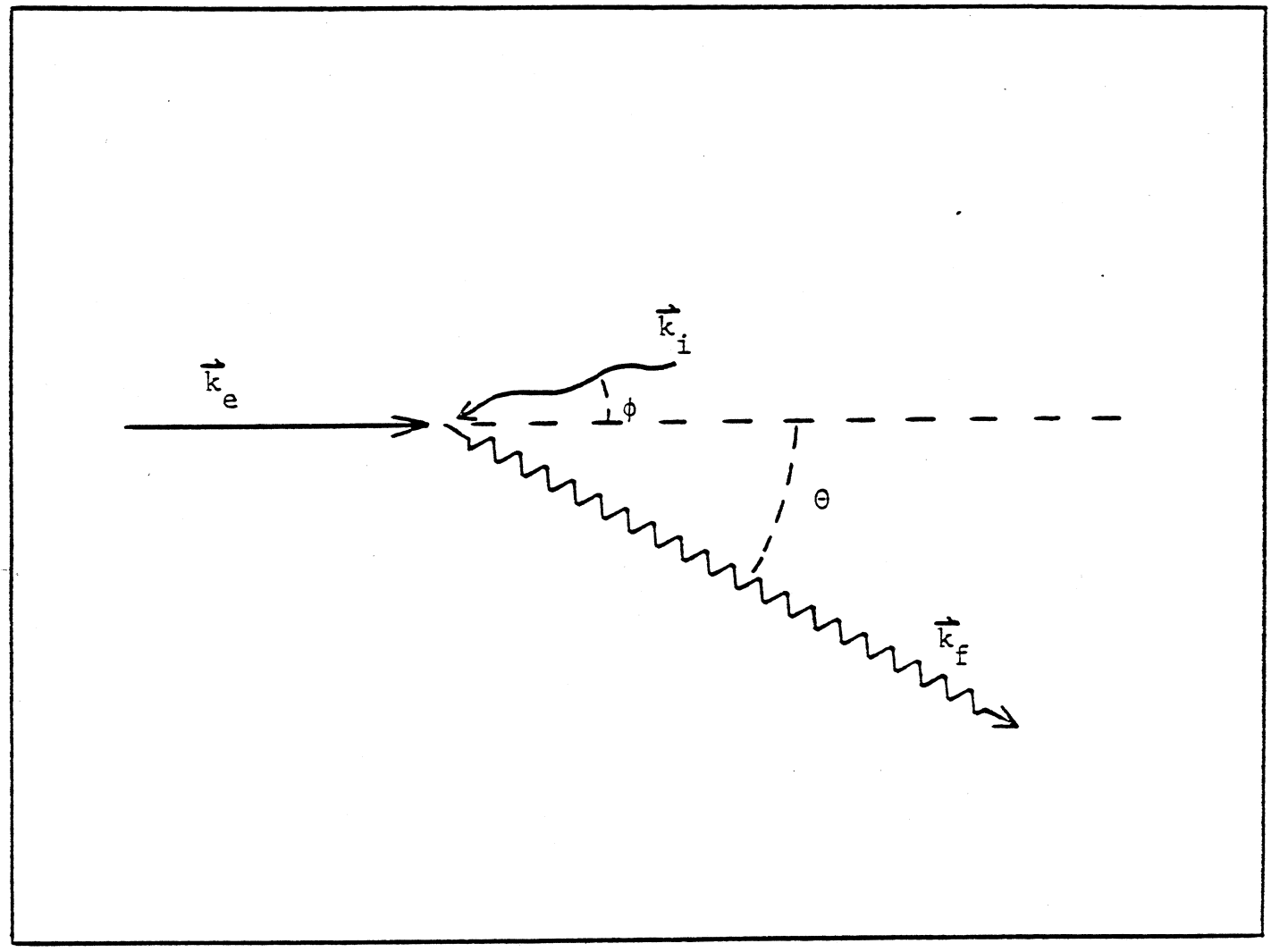

FIG. 1: Definition of the angles in the backscattering of laser photons of momenta $\vec{k}_i$ from electrons of momenta $\vec{k}_e$. The resulting γ ray carries away a momentum $\vec{k}_f$. (Angles are shown greatly magnified.)

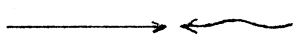

BEFORE SCATTERING

AFTER SCATTERING

LAB

e REST FRAME

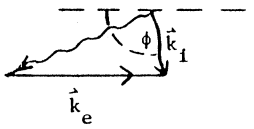

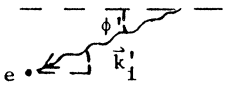

$\phi' << \phi$

$$\cos\phi' = \frac{\gamma(\cos\phi+\beta)}{\left[\sin^2\phi + \gamma^2(\cos\phi+\beta)^2\right]^{1/2}}$$

e.g. for $\gamma = 5000$

$0^o \leq \phi \leq 180^o \longrightarrow \phi' < 0.012^o$

$$k'_i c = \gamma(k_i c - (\beta c)[-k_i \cos\phi])$$
$$= \gamma k_i c\,(1+\beta\cos\phi)$$

e REST FRAME

LAB

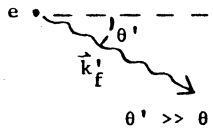

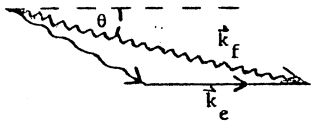

$\theta' >> \theta$

$$\cos\theta' = \frac{\gamma(\cos\theta-\beta)}{\left[\sin^2\theta + \gamma^2(\cos\theta-\beta)^2\right]^{1/2}}$$

e.g. for $\gamma = 5000$

$0 \leq \theta' \leq 179^o \longrightarrow \theta < 1.40^o$

$$k_f c = \gamma(k'_f c - (-\beta c)[k'_f \cos\theta'])$$
$$= \gamma k'_f c\,(1+\beta\cos\theta')$$

FIG. 2: Angle and energy transformations in laser backscattering. As shown schematically in the vector diagrams, angles ϕ between the initial laser and electron directions are collapsed by two successive Lorentz transformations, and have essentially no effect upon the final gamma ray.

$$E = \frac{\gamma^2 \varepsilon_\ell (1+\beta\cos\phi)(1+\beta\cos\theta')}{1 + \frac{\gamma\varepsilon_\ell}{mc^2}(1+\beta\cos\phi)(1+\cos(\phi'+\theta'))} . \qquad (1.1)$$

The relation between ϕ',θ', and the corresponding laboratory angles is given in Fig. 2. Because of the sequential angular compressions from the Lorentz transformations, the final γ-ray energy is completely unaffected by the initial finite divergences, in the laser and electron beams, that contribute to ϕ. To an excellent approximation, Eq. (1.1) may be rewritten as

$$E = \frac{4\gamma^2 \varepsilon_\ell}{1 + \frac{4\gamma\varepsilon_\ell}{mc^2} + \theta^2\gamma^2} . \qquad (1.2)$$

The highest energy γ rays are traveling at $\theta=0^\circ$ relative to the electron direction. The resolution of this γ ray beam could thus be determined by collimation. However, in any practical situation the scattering angle cannot be defined to better than the electron beam divergence (θ_e), and thus for electrons with energy resolution ΔE_e, the resolution attainable with a collimator (whose half-angle is θ_c) is

$$\frac{\Delta E_\gamma}{E_\gamma} \simeq \left[\left(\frac{2\Delta E_e}{E_e}\right)^2 + (\gamma\Delta\theta)^4\right]^{1/2} , \qquad (2.1)$$

where

$$\Delta\theta = \left[\theta_e^2 + \theta_c^2\right]^{1/2} . \qquad (2.2)$$

These γ rays also retain the polarization of the incident laser light. For relativistic electrons, helicity is a good quantum number, and the electron spin flip amplitude is negligible if θ is small. Thus if a laser is used with Brewster windows so that the incident light is plane polarized, the emerging γ rays will also be linearly polarized to the degree

$$P \simeq 1 - (\Delta\theta\gamma)^2, \qquad (3)$$

although this expression only holds for small angles.*

As an example of the above equations, if 3.0 eV laser light backscatters from 2.5 GeV electrons having an angular divergence (θ_e) of 4×10^{-5} radians, then ~255 MeV γ rays are produced. When collimated so that $\theta_c \ll \theta_e$, these γ rays have an energy resolution of 3.5% and a polarization of about 96%. The general dependence of the gamma ray energy upon the incident electron beam (upon γ in Eq. 1) is shown by the solid curves in Fig. 3 for different high-power lasers.

II.2 Previous Successes

Over the past 18 years there have been several attempts to produce γ ray beams by laser backscattering. At the Lebedev Institute, 1.78 eV light from a ruby laser was used with 600 MeV electrons to produce 7 MeV γ rays (KU64). At the Harvard-MIT Synchrotron the same laser line was later used wit 6 GeV electrons to produce 400 MeV γ rays (Be65). Both of these early attempts produced extremely low fluxes and could not be used for either nuclear or particle physics research. The first experiment to actually use laser-backscattered photons as a beam in a physics measurement was conducted at SLAC (Ba69). Here, a massive hydrogen bubble chamber, acting as both target and detector, compensated for the very low fluxes (300 s^{-1}) of 5 GeV γ rays that were produced.

*The polarization is discussed in detail in Section III.1.

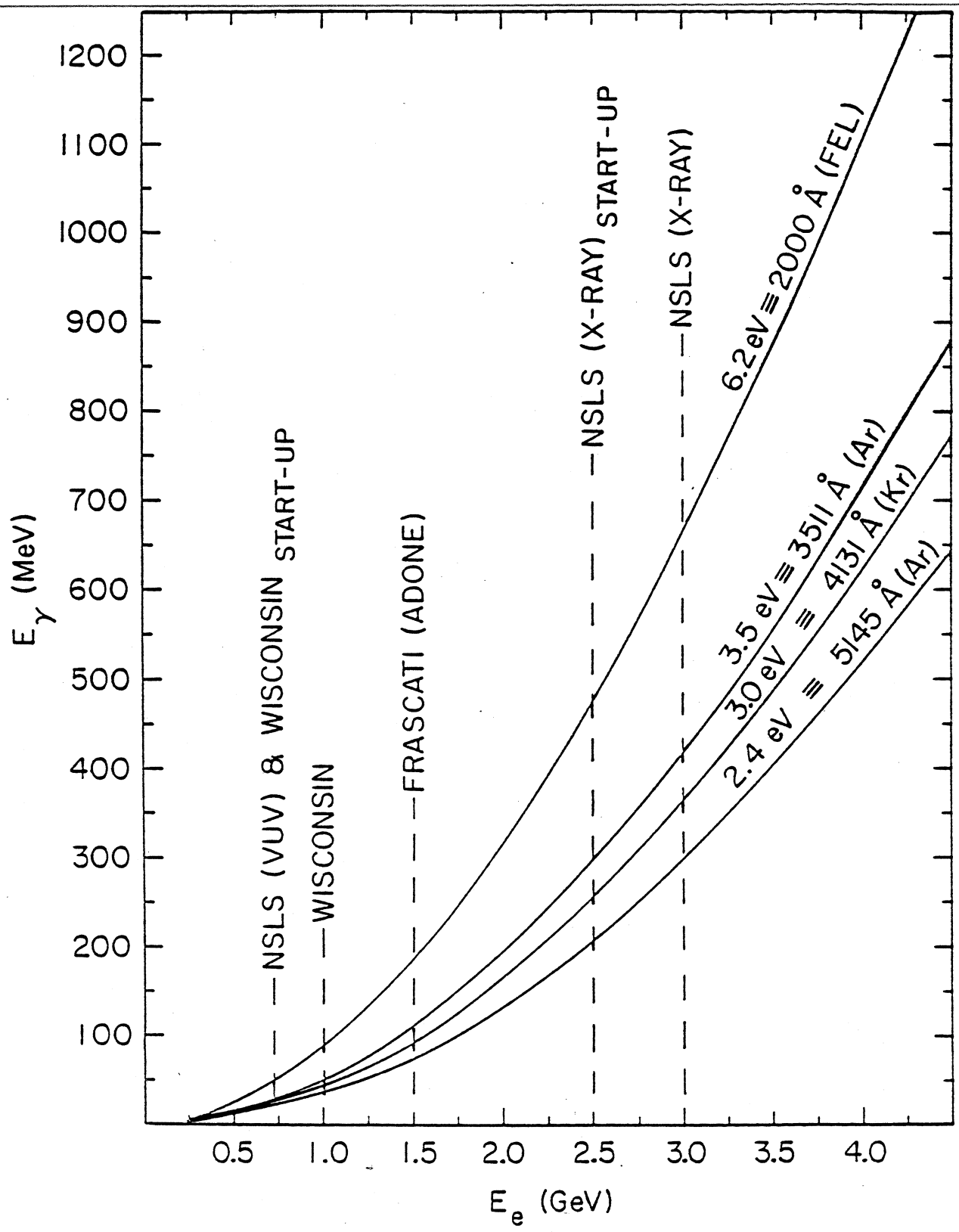

FIG. 3: The dependence of the maximum backscattered photon energy upon the electron beam energy is shown here by the solid curves for the indicated laser lines.

To achieve flux levels in the γ-ray beam that are useful for nuclear physics research, very high electron currents are required - on the order of one ampere. Because of the enormous power levels implied by such a relativistic electron beam (1 GeVx1 Ampere = 1000 M Watts), these currents can only be achieved in storage rings where the same circulating electron makes 10^6 contributions to the charge passing a fixed point in one second. As a further constraint on the storage ring, a straight electron-laser interaction region, in which the angular divergence of the stored beam is small, is required to achieve high luminosity, the γ-ray flux being directly proportional to the length of this region.*

The first real γ-ray "beam" for nuclear physics research was developed at the 1.5 GeV ADONE storage ring at Frascati National Laboratories (Ma77). Their experimental layout is shown in Fig. 4. The 2.41 eV light from an external Argon-Ion laser, pulsed to provide photon bunches at the same frequency as the storage ring, is arranged in time to pass through a straight section between electron pulses, bounce back from a mirror, and then collide with the next electron bunch in the middle of the straight section. The angular divergence of the Adone electron beam is about $1x10^{-4}$ radians, and this defines the minimum collimation angle. At the same time, the diameter of the collimator cannot be smaller than the physical size of the electron beam (~3mm), and should in fact be several times larger so that the source approximates a point. This dimension and angular acceptance puts the collimator at several tens of meters away from the

*See Section III.3

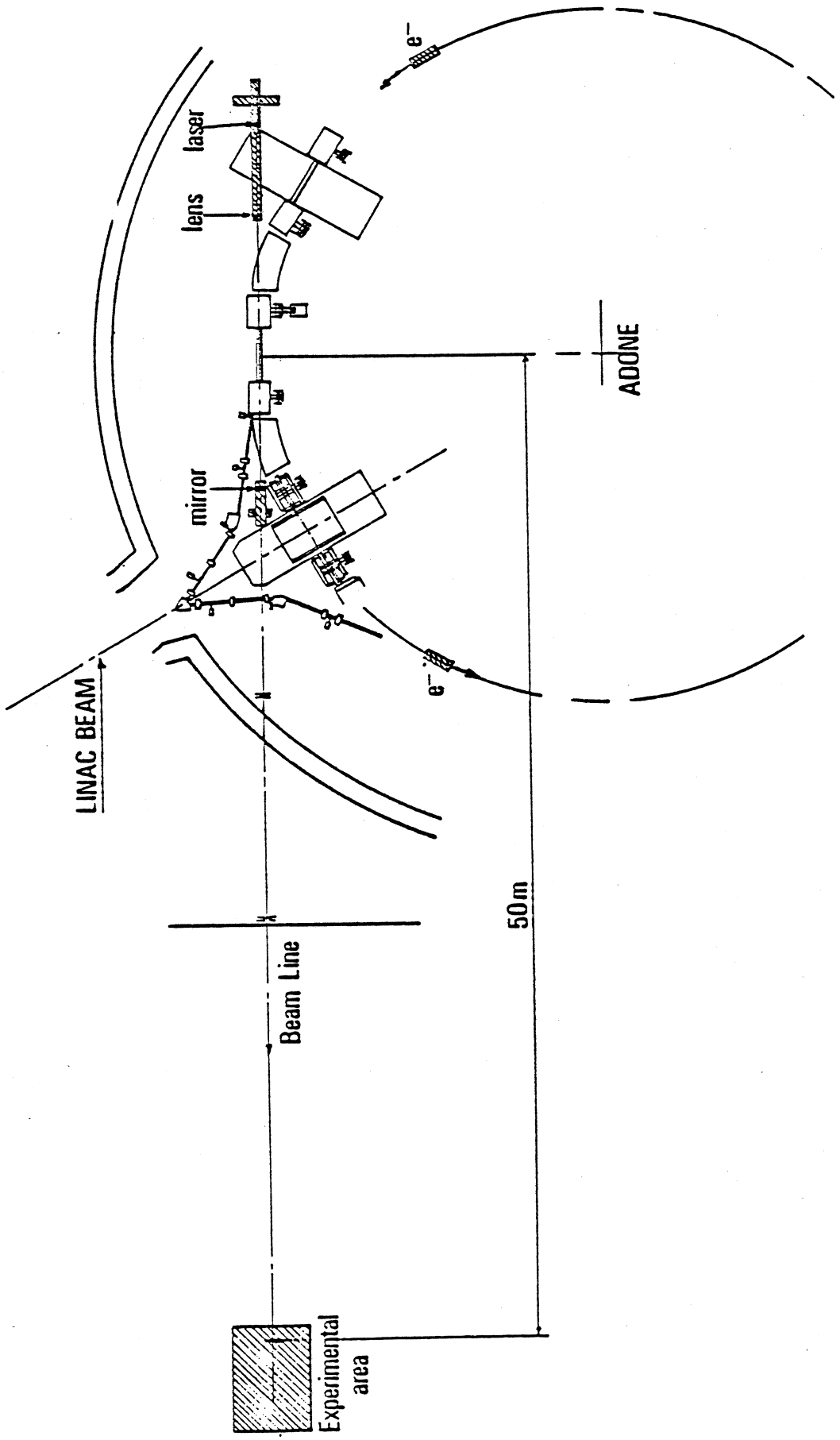

FIG. 4: Layout of the $E_\gamma \leq 80$ MeV laser-backscattered facility at the ADONE storage ring at Frascati.

interaction region. In the arrangement of Fig. 4, the final angle-defining, and hence energy-defining, collimator is located 50 meters from the laser-electron collision region. A typical spectrum of the γ rays emerging from this collimator is shown in Fig. 5. (The long low-energy tail is due mainly to the angular spread of the electron beam in the region of overlap with the laser.) This LADON$^+$-I facility has delivered up to 5×10^4 sec^{-1} polarized γ rays variable in energy up to 80 MeV, and has been used in a recently published study of meson exchange effects in the photodisintegration of deuterium (DE81).

A second phase of the Frascati project is currently under development. In the first phase described above, C.W. Argon-Ion laser, giving the highest power commercially available in this wavelength region, was pulsed with an optical cavity dumper to provide 20 W pulses, 15 ns in length, which were then arranged to collide with electron pulses. A laser can be regarded as being made up of two components: a plasma tube and an optical cavity. The internal laser power, the light intensity outside the plasma tube but inside the optical cavity, is approximately 10 times larger than the external power output. In the LADON-II setup, the optical cavity of the Argon laser has been stretched to 17.5 meters to encompass the straight section and the entrance and exit dipole magnets. The electron beam can now enter the optical cavity and collide with the internal laser power. The laser must still be pulsed so that the collisions with the electrons take place only in the straight section and not in regions

$^+$LADON = Laser on ADONE

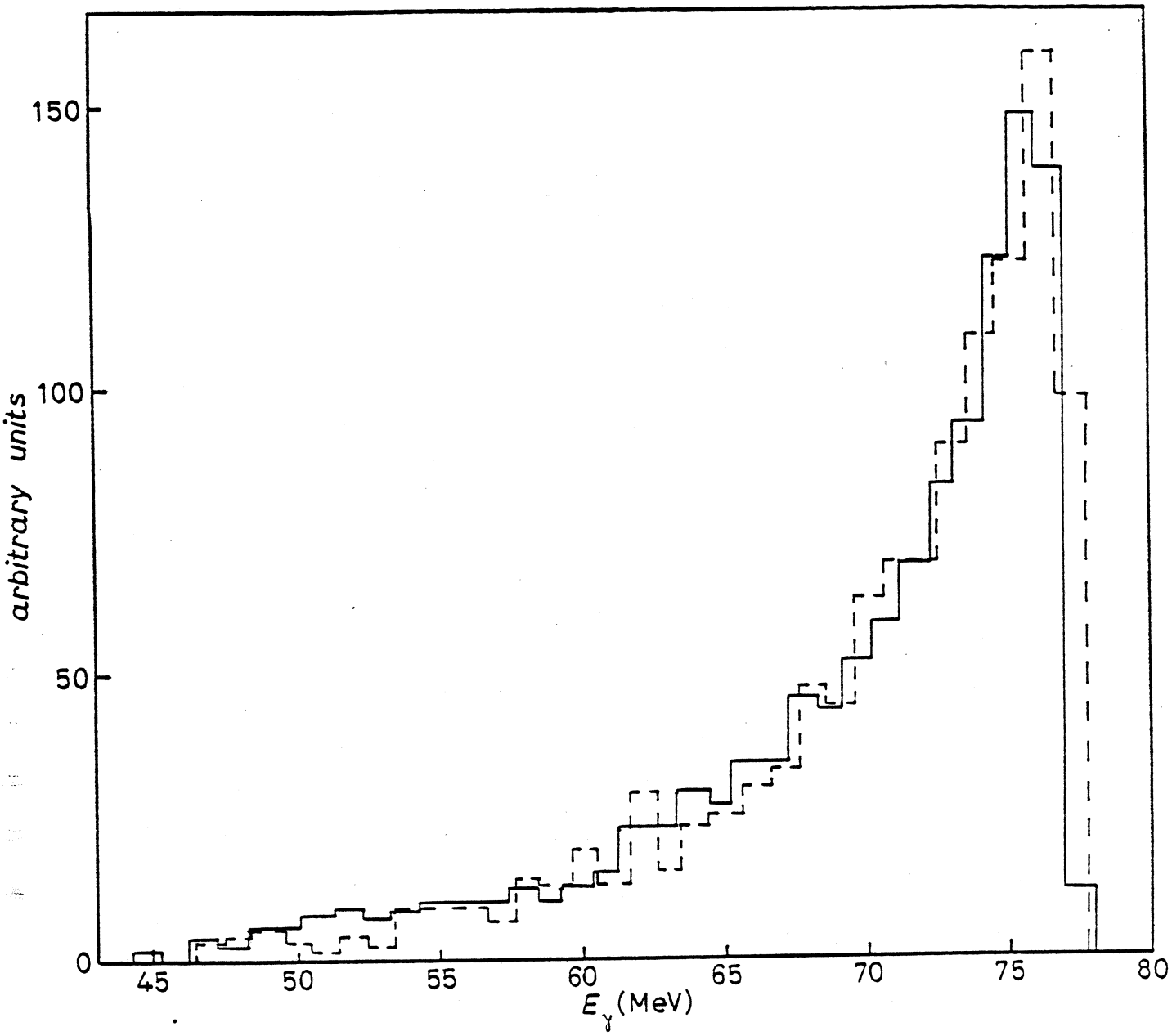

FIG. 5: The quasimonochromatic photon beam obtained at Frascati by collimating the laser-backscattered radiation is shown here (solid lines). The dashed lines are the results of a Monte Carlo calculation that takes into account the finite electron beam dimensions and divergences.

of quadrupoles or dipoles where the angular divergence is worse and where the beam direction is not aligned with the γ-ray collimator. To do this at a high repetition rate while maintaining the high internal laser power, the laser must be mode-locked with an acousto-optic crystal inserted into the cavity. Such a mode-locked Ar-Ion laser, with a 17.5 meter cavity, has been successfully bench tested at Frascati and provides 200 W pulses, 15 ns in length. The laser cavity has recently been installed on the ADONE ring, and is currently undergoing testing. The factor of 10 increase in peak laser power will result in a LADON-II γ-ray flux of about 5×10^5 s^{-1}.

The 1.5 GeV limit on the ADONE ring restricts the LADON facility to the region well below pion threshold. This limitation has prompted members of the Frascati group to join this proposed venture at BNL. The world's supply of high-current electron storage rings, either already operating or soon to come on line, is indicated by the dashed lines in Fig. 3. (The SRS machine at Daresbury is not included here, since it has no straight sections. The SPEAR ring at Stanford and DORIS at Hamburg are also excluded since their stored beams do not have the low emittance over a long straight section that is necessary for high γ ray flux and duty factor, and are limited in current to less than 100 mA.) The "X-RAY" ring of the National Synchrotron Light Source at BNL is presently the only machine capable of producing large fluxes of laser-backscattered γ rays, several hundreds of MeV in energy. The X-RAY ring is a state of the art storage ring with up to a factor of 3 better emittance that ADONE, and with a factor of 5 higher electron current that can be compressed in the straight sections into an area which is smaller than that of ADONE by more than

a factor of 10. The flux levels and γ-ray beam characteristics that we expect to achieve by backscattering laser light from the electrons of this ring are discussed in detail in the next section.

III. High Energy γ Ray Beams from the NSLS

III.1 Cross Sections for Backscattering

In the frame in which the electron is initially at rest (designated as primed), the Compton scattering cross section for linearly polarized photons is given by

$$\frac{d\sigma}{d\Omega'} = \frac{r_o^2}{4}\left(\frac{E'}{\varepsilon'}\right)^2\left[\frac{E'}{\varepsilon'} + \frac{\varepsilon'}{E'} - 2 + 4\cos^2\xi\right], \qquad (4.1)$$

where ξ is the angle between the initial and final polarization vectors, and r_o is the classical radius of the electron, 2.818 fm (BJ64). Here ε' and E' are the photon energies before and after backscattering, measured in the electron's frame. These energies are related by

$$\frac{E'}{\varepsilon'} = \frac{1}{1 + \frac{2\gamma\varepsilon_\ell}{mc^2}(1 + \cos\theta')}, \qquad (4.2)$$

where ε_ℓ is the laser energy in the lab and γmc^2 is the electron beam energy. The scattering angle is defined in Figs. 1 and 2. As mentioned in Section II.1, the dependence upon an initial angle between the incoming laser and electron beams is unmeasurably small, and has been dropped from the above equations. As shown in Fig. 2, the relation between θ' and the corresponding lab angle is

$$\cos\theta' = \frac{\gamma(\cos\theta-\beta)}{[\sin^2\theta + \gamma^2(\cos\theta-\beta)^2]^{1/2}} \tag{4.3}$$

The angle ξ in Eq. (4.1) is a function of the polar and azimuthal angles θ and Φ of the outgoing photon. The cross section for scattering into θ and Φ with a polarization vector parallel to that of the incoming laser light is*

$$\frac{d\sigma_{\parallel}}{d\Omega'} = \frac{r_o^2}{4}\left(\frac{E'}{\varepsilon'}\right)^2 \left[\frac{E'}{\varepsilon'} + \frac{\varepsilon'}{E'} + 2 - 4\sin^2\theta'\cos^2\Phi\right](1-\sin^2\theta'\cos^2\Phi), \tag{5.1}$$

while the total cross section, without regard for the final polarization, is

$$\frac{d\sigma_{TOTAL}}{d\Omega'} = \frac{r_o^2}{2}\left(\frac{E'}{\varepsilon'}\right)^2 \left[\frac{E'}{\varepsilon'} + \frac{\varepsilon'}{E'} - 2\sin^2\theta'\cos^2\Phi\right]. \tag{5.2}$$

The integration of Eq. (5.2) over Φ results in the Klein-Nishina formula (KL29):

$$\frac{1}{2\pi}\int_0^{2\pi} \frac{d\sigma_{TOTAL}}{d\Omega'}\, d\Phi = \frac{r_o^2}{2}\left(\frac{E'}{\varepsilon'}\right)^2 \left[\frac{E'}{\varepsilon'} + \frac{\varepsilon'}{E'} - \sin^2\theta'\right]. \tag{5.3}$$

The laboratory cross sections for backscattering are then simply obtained by multiplying Eq. 5 by the Jacobian:

*If θ is measured relative to the direction of the Lorentz transformation, then $\Phi'=\Phi$.

$$\frac{d\sigma}{d\Omega_{LAB}} = \frac{d\sigma}{d\Omega'} \cdot \frac{d\Omega'}{d\Omega_{LAB}} \quad , \tag{6.1}$$

where

$$\frac{d\Omega'}{d\Omega_{LAB}} = \gamma \frac{[\sin^2\theta + \cos\theta(\cos\theta-\beta)]}{[\sin^2\theta + \gamma^2(\cos\theta-\beta)^2]^{3/2}} \quad . \tag{6.2}$$

The effect of the Lorentz transformations is to compress all of the cross section into a narrow region about $\theta_{lab}=0^{o}$. The extent of this compression increases roughly as the square of the electron energy. This is evident in Fig. 6 where the dependence of the lab cross section [Eq. (5.3) multiplied by the Jacobian of Eq. (6.2)] upon angle is plotted for 3.0 eV laser light incident upon 0.7 GeV electrons (dashed curve) and upon 2.5 GeV electrons (solid curve). The dependence of the backscattered γ-ray energy, determined from Eq. (1), is also shown with its scale on the right (dot-dashed and open-circled curves, respectively). If the γ-rays are collimated to an angle equal to the minimum divergence of the electrons in the NSLS x-ray ring (4×10^{-5} radians, indicated by the dashed vertical line in Fig. 6), the energy variation in the transmitted γ-ray beam is relatively small, about 3.5% at 255 MeV.

As mentioned in Section II.1, the γ-ray beam retains most of the linear polarization of the laser light. The parallel component of

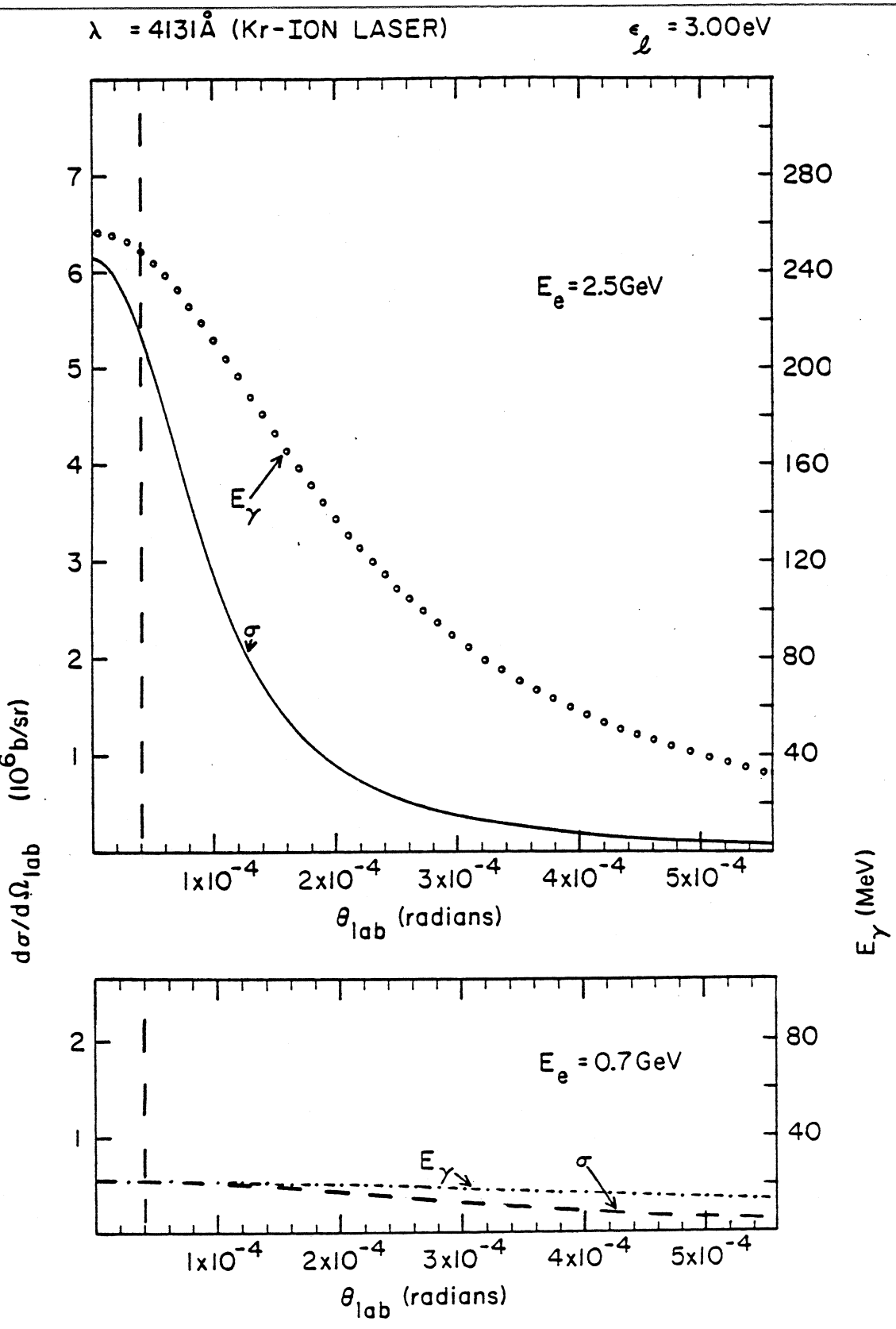

FIG. 6: The cross section for γ ray production by laser backscattering is shown as a function of lab angle relative to the electron beam direction (scale on the left). The corresponding energy variation of the γ rays is also shown (open circled and dot-dashed curves) with their scale on the right. The dashed vertical line indicates the minimum divergence of the X-RAY ring electrons.

the cross section is compared to the total in Fig. 7. The ratio of these two, the polarization, is shown at the bottom of the figure. For angles θ less than 1×10^{-4} radians, the polarization can be approximated by the expression in Eq. 3.

Both total and parallel cross sections peak strongly at $\theta_{lab}=0$. However, this is somewhat misleading since the transmitted γ-ray flux is proportional to the cross section integrated over the angular acceptance of the collimator. This is shown in Fig. 8 for both σ_{total} (solid curve) and $\sigma_{\parallel}$ (dashed curve), assuming a circular collimator. The $\sin\theta$ factor in the integration kills the cross section as θ approaches zero. The integrated cross section rises very rapidly as the collimation angle is increased, but the transmitted γ-ray energy range (open circles with their scale on the right of Fig. 8) also changes quite rapidly with increasing θ. The total γ-ray spectrum produced by 3.0 eV laser light incident upon 2.5 GeV electrons is plotted in Fig. 9. The corresponding angles at which these γ rays emerge are shown by the scale at the top of this figure. All of the γ rays capable of producing nuclear reactions are contained within 10^{-3} radians of the electron beam direction. (This spectrum produced by backscattering is almost flat compared with other methods of producing γ rays, such as electron Bremsstrahlung where the γ-ray intensity decreases as roughly $1/E_{\gamma}$.) If a portion of this spectrum is selected by a circular collimator, then only the highest energy γ rays remain completely polarized. As θ increases, E_{γ} decreases and the degree of polarization drops (bottom of Fig. 7). However, this need not be the case for an asymmetric rectangular collimator. This is illustrated schematically in Fig. 10. If the electron beam direction defines the

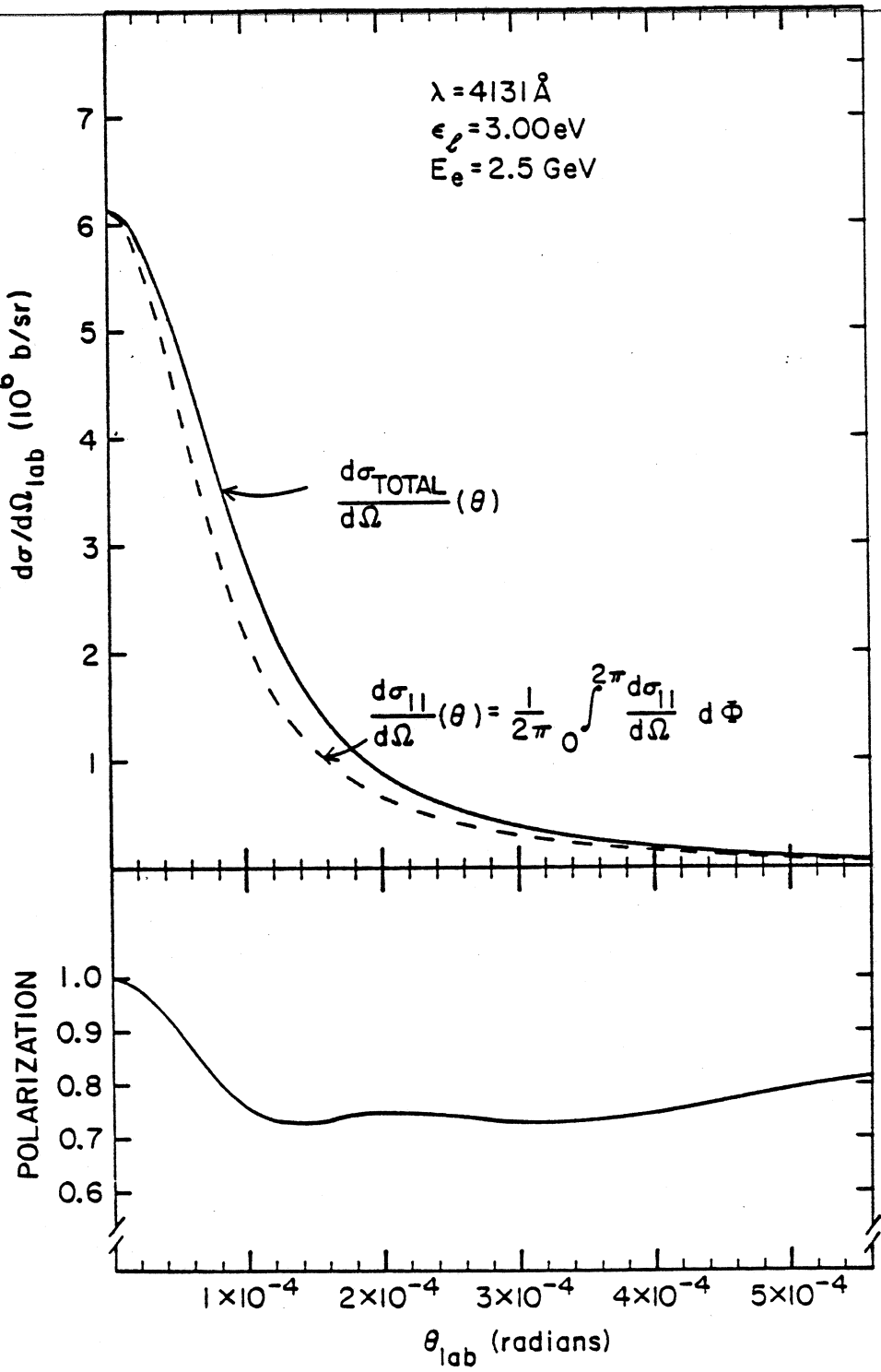

FIG. 7 : The cross section for producing γ rays with linear polarization parallel to the laser polarization is shown by the dashed curve. The total backscattering cross section without regard to polarization (parallel + perpendicular) is shown in the top part of the figure as the solid curve. The ratio of these two cross sections, the γ ray beam polarization, is shown at the bottom.

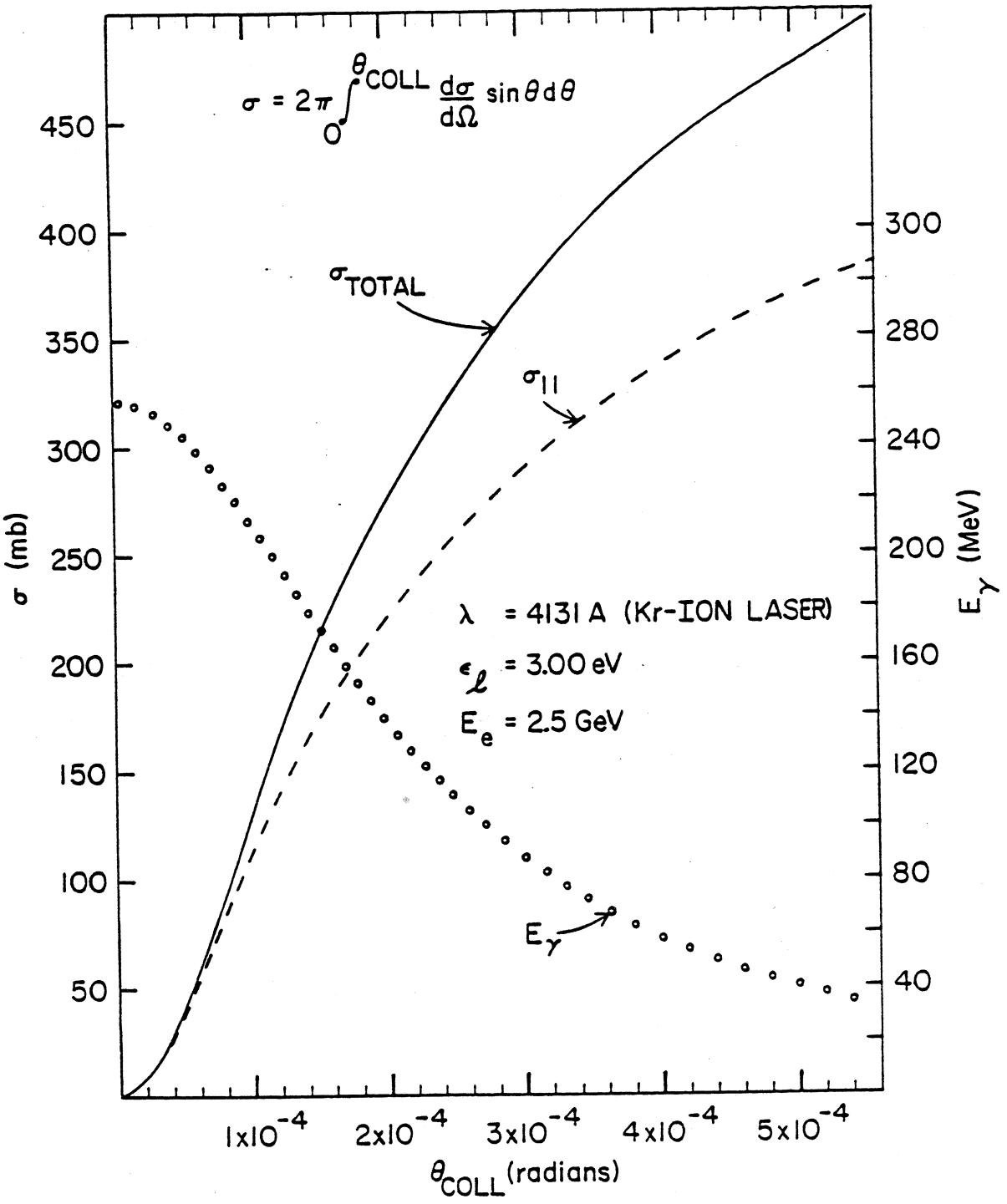

FIG. 8: The behavior of the parallel and total (parallel + perpendicular) cross sections for γ ray production by backscattering, integrated over a circular collimator of half-angle θ_{COLL}, are shown as the dashed and solid curves, respectively. The variation in γ-ray energy across the collimator is also shown as the open-circled curve with its scale on the right.

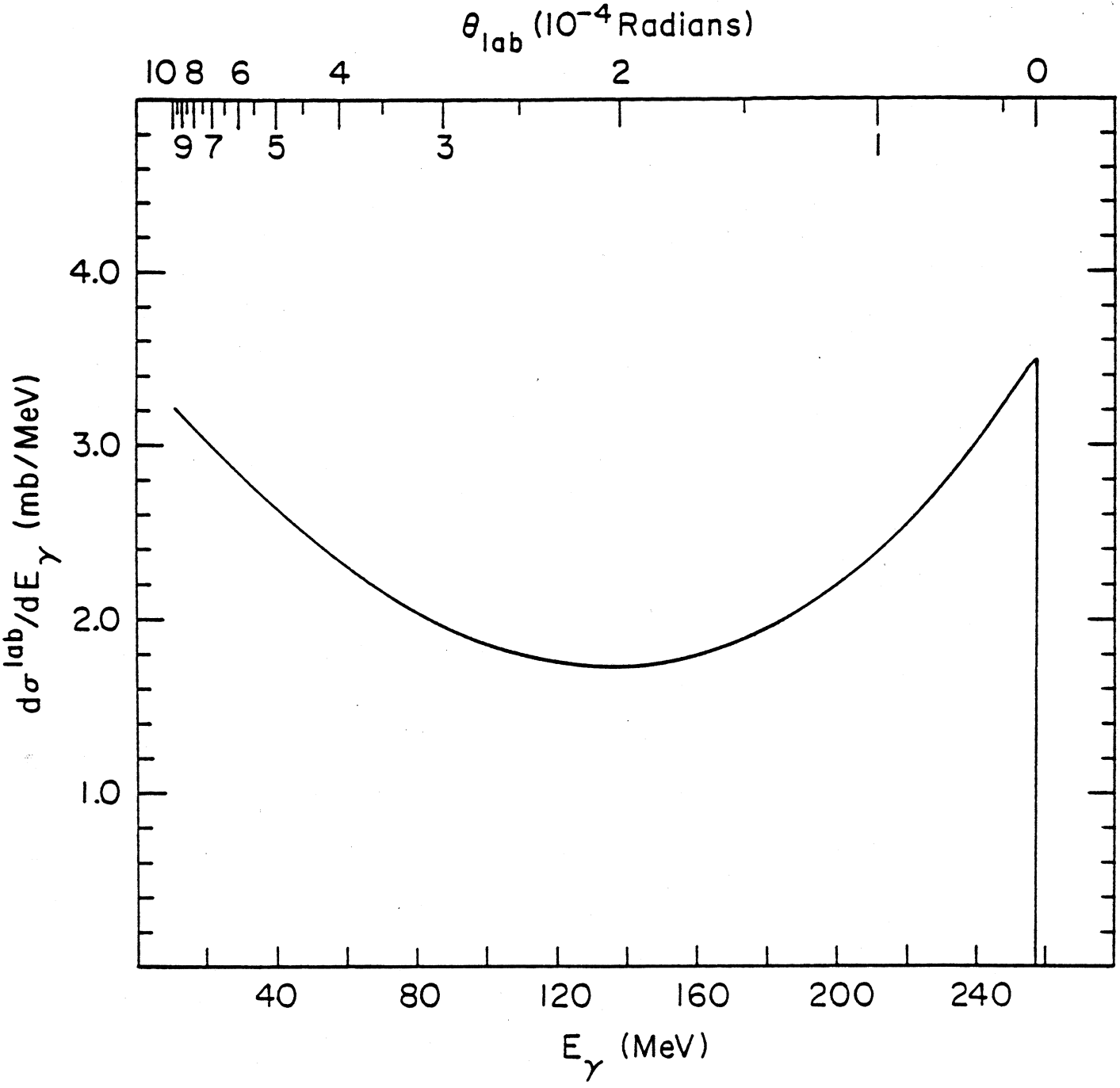

FIG. 9: The γ-ray energy spectrum obtained by backscattering 3.0 eV laser light from 2.5 GeV electrons. (This is effectively the solid curve of Fig. 6, per unit solid angle, plotted against the open-circled curve of Fig. 6.) The angles at which these γ rays emerge relative to the electron beam axis is indicated at the top of the figure.

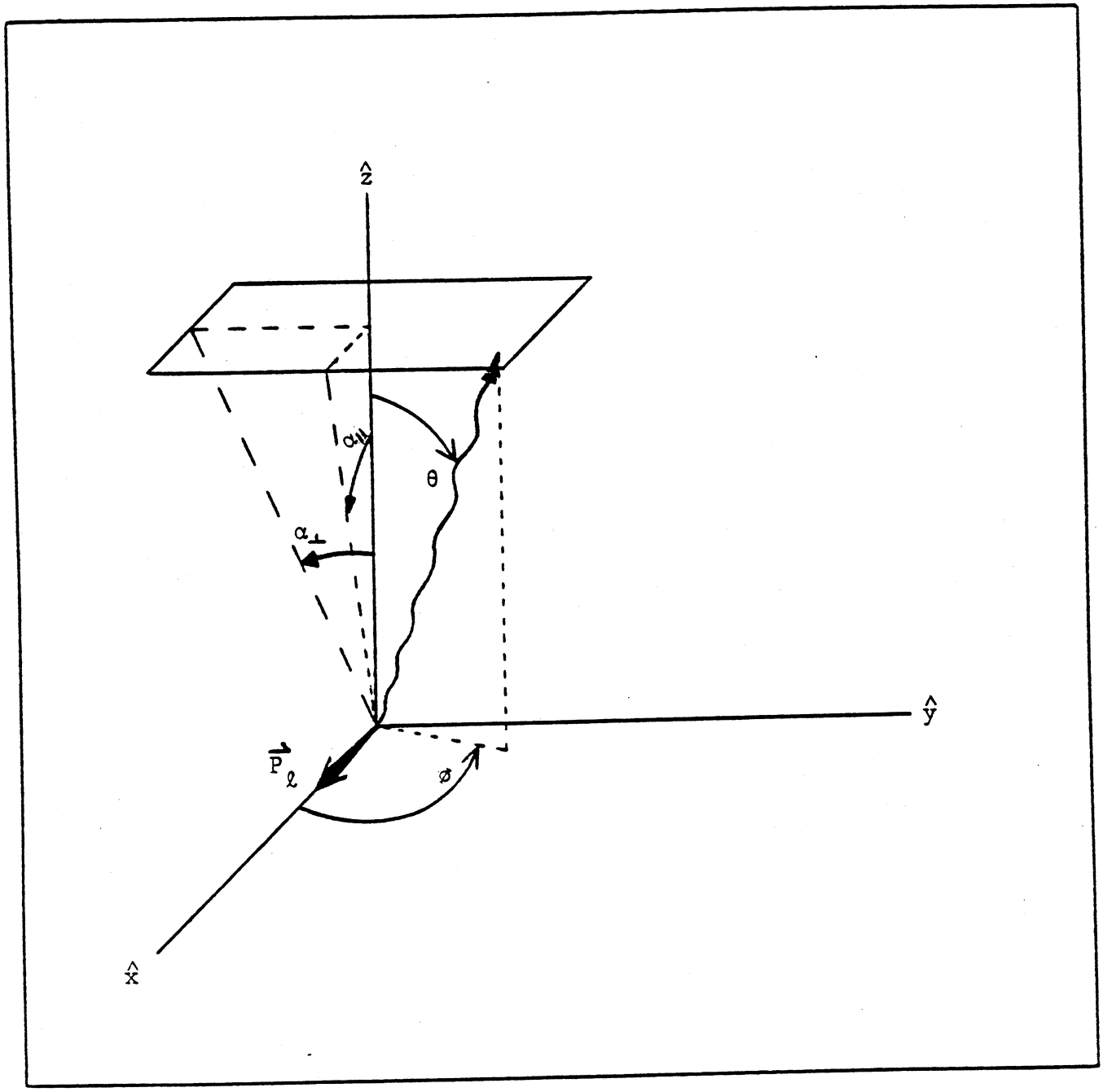

FIG. 10: Schematic representation of a collimator used to increase the polarization of the transmitted γ-ray beam. The electrons are to be considered travelling along $\hat{Z}$, and the laser along $-\hat{Z}$ with polarization $\vec{P}_\ell$ along $\hat{x}$. The γ rays backscatter through the collimator defined by the angles $\alpha_{\parallel}$ (parallel to $\vec{P}_\ell$) and $\alpha_\perp$ (perpendicular to $\vec{P}_\ell$).

z axis and the polarization $\vec{P}_\ell$ of the initial laser light defines the x axis, then γ rays emerging in the <y-z> plane are completely polarized parallel to $\vec{P}_\ell$. The contamination of the beam with γ rays polarized perpendicular to $\vec{P}_\ell$ comes from scattering into azimuthal angles near 0 or π. The collimator shown in Fig. 10 restricts this contamination when it is narrow in the direction $\vec{P}_\ell$. For the example shown in Figs. 7-9, the upper two-thirds of the energy spectrum of Fig. 9 is transmitted through a circular collimator with a half angle of 3×10^{-4} radians. However, most of these γ rays are only 75% polarized. If, instead, a collimator such as shown in Fig. 10 is used with opening angles $\alpha_{\parallel}=3\times10^{-5}$ radians and $\alpha_{\perp}=3\times10^{-4}$ radians, then the backscattering cross section integrated over this collimator is reduced by a factor of 3,but the polarization of the transmitted γ rays is greater than 94% throughout the entire dynamic range (88 to 257 MeV).

III.2 Tagging

The angle η of the scattered electron, Fig. 11(A), that gave up $(E_e-E_{e'})$ of its energy to produce the high-energy γ ray is related to the γ-ray energy and angle by

$$\eta = \left(\frac{E_\gamma}{E_e-E_\gamma}\right)\theta \ . \qquad (7)$$

Thus, for γ rays up to 257 MeV produced by backscattering from 2.5 GeV electrons, the cone of scattered electrons is collapsed a factor of 10 smaller than the already narrow γ-ray cone ($\eta\lesssim10^{-1}\theta$). In fact, the electrons which produced the upper two-thirds of the γ-ray spectrum of Fig. 9 are diverging from the interaction at angles less than twice

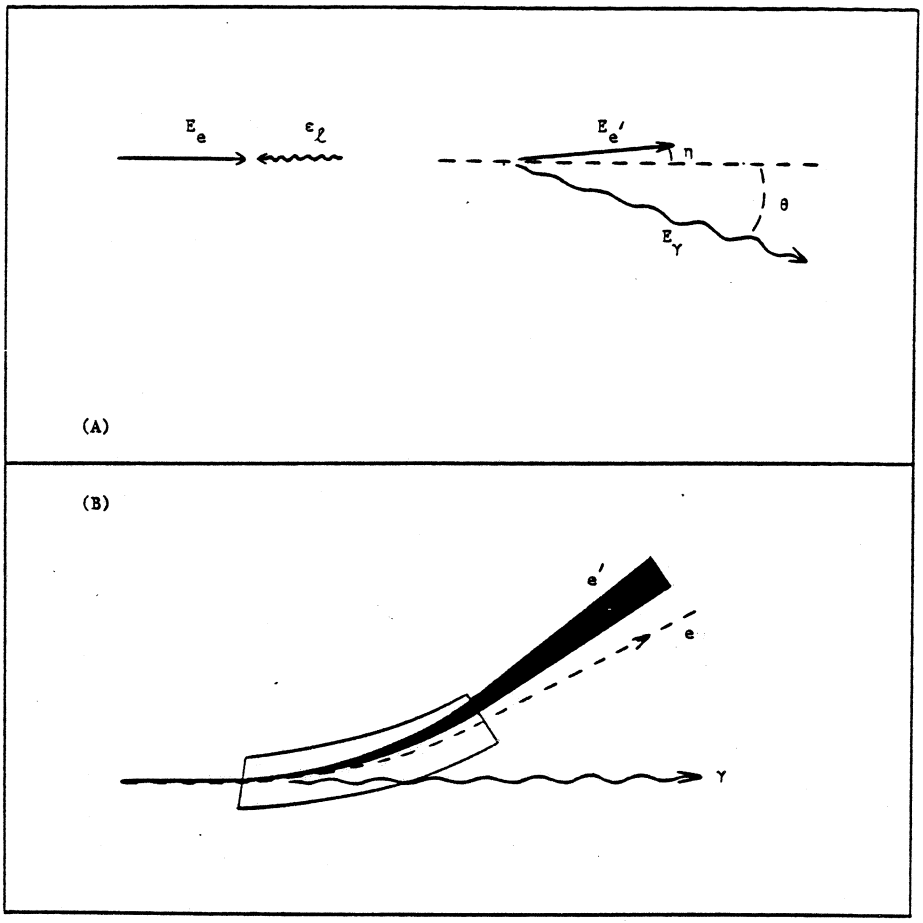

FIG. 11: (A) Definition of the angles of the back-scattered γ ray (θ) and of the electron that gave up some of its energy to produce the γ ray (η).

(B) As shown here schematically, the Compton-scattered electrons have a lower momentum and are separated from the stored beam by the ring dipole following the laser-electron interaction straight.

the intrinsic divergence of the beam in the storage ring. The storage-ring dipole magnet immediately following the straight interaction section momentum analyzes these scattered electrons, as shown schematically in Fig. 11(B). The γ-ray spectrum of Fig. 9 extends down to zero energy, and the corresponding scattered electrons become indistinguishable from the primary beam. However, all of the electrons associated with a high energy portion of the full backscattered spectrum can easily be separated from the primary beam and transported to a focal plane of the dipole magnet. The energy of the γ ray reaching the nuclear target is then defined by the position of its tagging electron on this focal plane. Because of the extremely small divergence of the scattered electrons, the efficiency of this tagging procedure is 100%, within the dynamic range of the tagging spectrometer. For the spectrometer described in section III.4, all γ rays greater than 175 MeV are tagged in the standard mode of operation. (If necessary, this limit can be lowered, but this requires a dedicated operation of the storage ring.) Thus, the energy of almost all γ rays and, in particular, all of the highest energy γ rays reaching the nuclear target is known. This is very different from tagged-Bremsstrahlung beams which are always accompanied by very large numbers of untagged γ rays of unknown energy, which can contribute large random components to nuclear measurements.

There are at least four significant benefits of tagging the backscattered γ-ray beam:

(1) The γ-ray collimation angle may be opened up, resulting in a large increase in backscattering cross section (Fig. 8) and hence in γ-ray flux. These γ rays are

spread over a range of energies. However, since no narrow structures are expected at hundreds of MeV of excitation, it is useful and even desirable to average excitation functions over some reasonable range of photon bombarding energy (~10 MeV). (In general, this cannot be done by simply using a poor resolution γ ray beam since, for many experiments, it is important to separate different final states. This separation must be done with high resolution before yields can be added to obtain an average cross section.) Thus, despite the large energy spread, the increased flux leads to substantial reductions in running time.

(2) Data may be accumulated over a large or small range of γ-ray energies, with appropriate choice of collimator. The tagging system described in Section III.4 can accept more than half (upper half) of the spectrum of Fig. 9, and is always 100% efficient within this interval. Thus almost any desired range of photon energies can be covered by appropriate choices of different lasers (see Fig. 3), without changing the energy of the electron beam in the storage ring. In this mode, the γ-ray backscattering facility can operate as simply another passive user and does not require dedicated use of the ring.

(3) The resolution attainable with tagging is significantly better than can be achieved by collimation. The limit is in fact not the tagging spectrometer, but the

intrinsic resolution of the stored beam, which is 0.1% for the NSLS x-ray ring. This translates to a tagged-γ-ray resolution of about 2.7 MeV that is nearly independent of γ-ray energy.

(4) The tagged γ-ray beam is much less sensitive to the tune of the storage ring, to small changes in electron beam phase space and position, and is almost completely insensitive to the electron divergence. This eliminates low energy tails, such as the one evident in Fig. 5, and leads to a much more efficient use of beam time.

There remains a single limitation on the flux of tagged γ-rays. The tagging that follows laser backscattering is 100% efficient so that if two γ rays,in the energy range defined by the collimator and above the minimum acceptance of the tagging spectrometer (175 MeV), are produced within a single electron pulse, then two counters on the tagging focal plane will fire. Any resulting nuclear event must be discarded since the energy of the incident photon that caused this event is ambiguous. These events cannot be resolved in time since, regardless of the location of the backward Compton scattering within the straight section, all γ rays created within a single electron pulse reach the nuclear target together and, similarly, the asociated electrons reach the focal plane of the tagging spectrometer at the same time. In the standard mode, the ring is operated at the repetition rate of the Rf cavity (ν_{Rf}=52.88 MHz), and electron pulses are separated by 18.9 nsec. If the laser power is sufficient to

produce an average of $\bar{N}$ γ rays that can be tagged (E_γ>175 MeV) per electron pulse, then the probability that K counters of the tagging focal plane will fire is given by a Poisson distribution,

$$P(K) = e^{-\bar{N}} \frac{\bar{N}^K}{K!} . \qquad (8)$$

P(1) is a maximum when $\bar{N}$=1, or when the total tagged rate is 5.288×10^7 sec^{-1}. Under these conditions P(1)=0.37, so that the maximum useful tagged flux is $5.3 \times 10^7 \times 0.37 = 2.0 \times 10^7$ sec^{-1}. For the discussions in the following sections, a useful tagged flux of 2×10^7 sec^{-1} is taken as an upper limit. (This limit can be increased if the kinematics of the nuclear reaction under study can make at least gross distinctions between different possible incident γ ray energies. The number of γ rays-per-MeV of bombarding energy can also be increased by raising the laser power and maintaining the same effective flux within a smaller dynamic range of the tagging spectrometer. However, this is also limited by the requirement that the number of active focal plane counters must not become too small.)

III.3 Expected γ-ray Fluxes and Modes of Operation Below 300 MeV

In the interaction of a pulse of laser light with a pulse of relativistic electrons, the number of backscattered photons is given by

$$N_\gamma = 2\sigma N_L f_L \frac{N_e}{A_e} \cdot f_e , \qquad (9)$$

where N_L and N_e are the number of laser photons and electrons, respectively. The geometrical efficiencies f_L and f_e depend on the cross sectional shapes of the interacting laser and electron pulses: f_L is the fraction of photons in the laser bunch that can collide with an electron, and similarly, f_e is the fraction of electrons that can collide with a laser photon. A_e is the cross sectional area of the electron bunch, and σ is the laboratory cross section for backscattering, integrated over the solid angle of the γ-beam defining collimator. The factor of 2 (actually 1+ cosθ with the angle defined as in Figs. 1 and 2) arises from the transformation of the number of backscattered photons per unit time, from the frame in which the electron was initially at rest, to the laboratory (Mi63). Using Eq. (9), the expected γ-ray flux may be written, in practical units, as

$$Y\ (\text{sec}^{-1}) = \frac{(2.60)I_e(\text{amps})P_L(\text{Watts})\sigma(\text{mb})L_L(\text{cm})}{\varepsilon_L(\text{eV})\ A(\text{cm}^2)}\ , \qquad (10)$$

where P_L is the peak laser power during the light pulse. ε_L is the energy of a laser photon, I_e is the circulating electron current, and L_L is the length of the laser pulse. The area A is $A_e/(f_L \cdot f_e)$. In the simple case where the electron beam is entirely contained within the laser area over the full interaction length L_L, A is just A_L, the cross sectional area of the laser pulse. More generally, if the electron beam has a Gaussian distribution in space characterized by half widths σ_x and σ_y, and if the cylindrical laser beam has a Gaussian power distribution which falls off radially with half width σ_L, then

$$A = 2\pi \sqrt{\sigma_L^2 + \sigma_x^2} \cdot \sqrt{\sigma_L^2 + \sigma_y^2} . \qquad (11)$$

By way of example, the Ar-Ion laser used in the LADON-I facility at Frascati delivered 20 Watts peak power in each 450 cm long laser pulse made up of 2.41 eV photons. The laser pulse was cylindrical with a radius σ_L=0.71 mm. The electron beam was roughly rectangular, with σ_x=2.7 mm and σ_y=1.1 mm, and the stored current was 75 mA. The γ-ray beam was collimated by a circular aperture with a half-angle of 9×10^{-5} radians, and at E_e = 1.2 GeV the backscattering cross section integrated over this collimator is 38 mb. With these parameters, Eq. (10) predicts a flux of 1.2×10^5 sec^{-1}. The observed flux was 5×10^4 sec^{-1} (Ma77).

The number of γ rays backscattered through the beam-defining collimator depends not only upon the areas of the electron and laser beams, but also upon how these areas vary with position along the interaction region, and upon how the angular divergence of the electrons varies along the interaction length. The effects of these variations are not included in Eqs. (10) and (11), and result in a reduction of observed flux from the estimate of Eq. (10).* The region of a straight section in the NSLS X-RAY ring is shown in Fig. 12. The straight length between dipole magnets is 11.3 meters, and the central length free of optical elements is 4.5 meters. (There are 8 such straight sections in this storage ring.) The divergence, size, and shape of the beam in the straight sections is a function of the "tune" in the storage ring (i.e., of the choice for the various sextupole and quadrupole fields necessary to maintain the radiating

*For the LADON-I facility, these effects reduce the observed flux by a factor of 2.4.

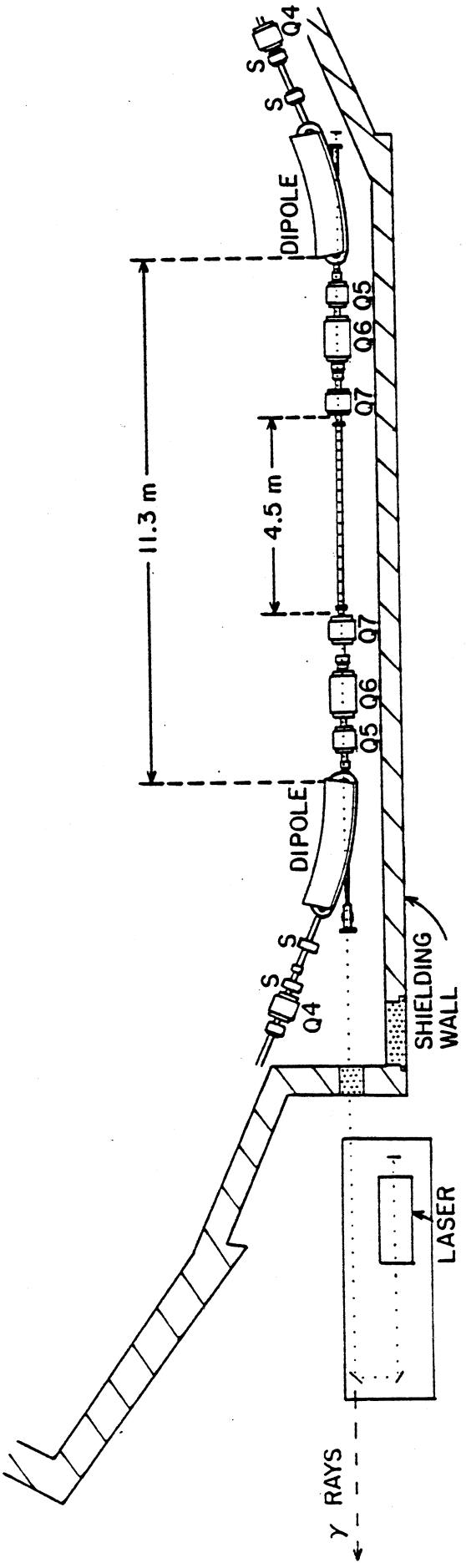

FIG. 12: The region of a straight section of the NSLS X-RAY ring. Quadrupoles are indicated by a Q, and sextupoles by an S.

stored beam in equilibrium with the Rf cavity). The horizontal and vertical divergences of the electrons in a straight section are shown in Fig. 13 for two tunes of the NSLS-X-RAY ring. The horizontal and vertical dimensions* of the beam in these two tunes are plotted in Fig. 14. The solid curves are for a tune which is known in the literature (va80) as the "OPTICS" solution. Here the beam is compressed to a very small flat ribbon with a horizontal divergence of 2.4×10^{-4} radians in the central 4.5 m of the straight section. The vertical divergence is a factor of 5 smaller over the same region. This tune will be used for the standard operation of the X-RAY ring. For comparison, the dashed curves in Figs. 13 and 14 represent an alternate solution called the "high-β" tune. In this tune the beam size is considerably larger, but the horizontal divergence in the central region is much less.

We have performed Monte-Carlo calculations to simulate the effects of varying electron beam size and angular divergence. Collisions with the laser light were assumed to occur throughout the 11.3 meter straight section, although with the "OPTICS" solution (solid lines of Fig. 14) the largest contribution to the γ ray flux comes from the central 4.5 meter section where the electron beam is smallest. (There is no necessity of avoiding the regions of large divergence near the quadrupoles, as was the case in Frascati, since here the resolution of the γ rays will be determined, not by collimation, but by tagging.) The predicted spectrum of γ rays transmitted through a collimator with a half-angle of 4×10^{-4} radians

*The beam is assumed to have a Gaussian distribution in space, and the half-width values are plotted in Fig. 14. Similarly, the angular divergence is assumed to follow a Gaussian distribution, and it is the corresponding half-width values that are plotted in Fig. 13.

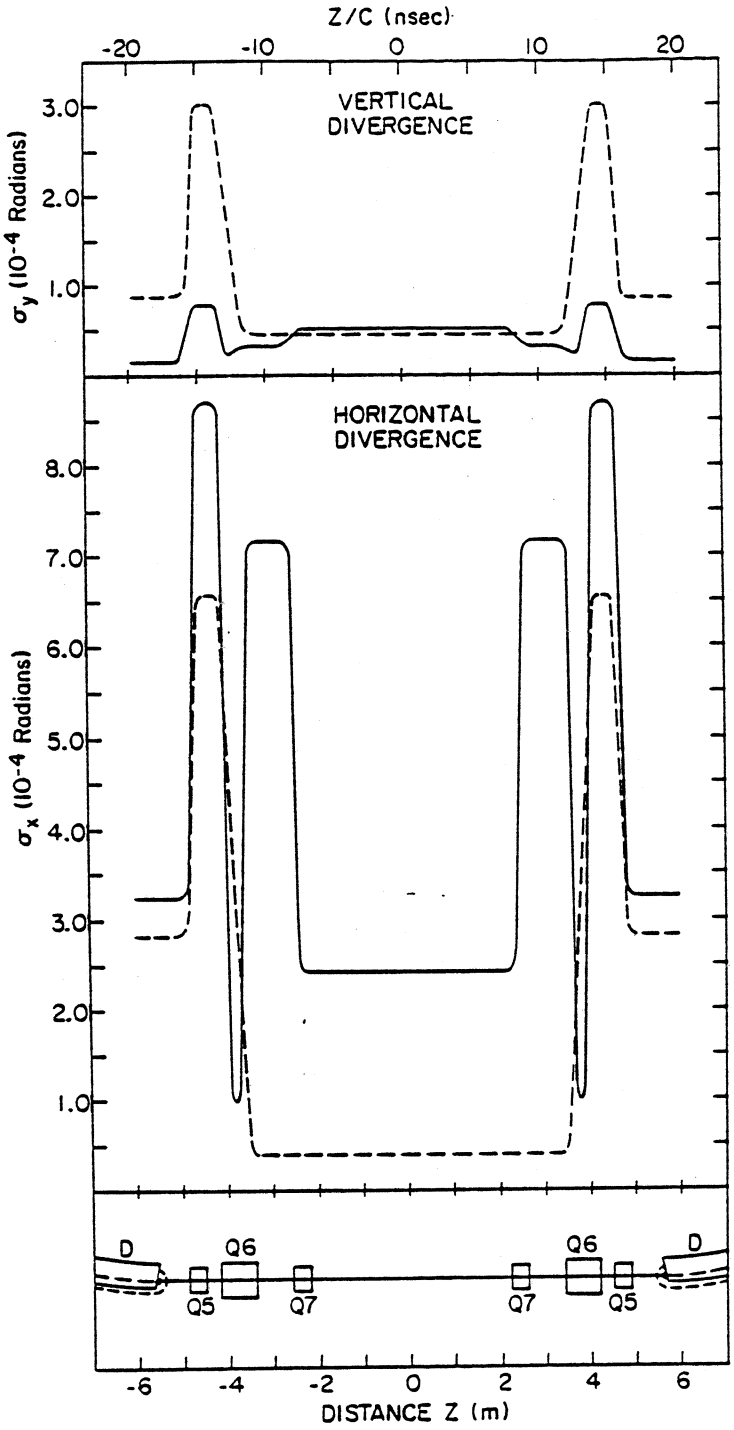

FIG. 13: The horizontal and vertical divergences of the electrons in a straight section of the NSLS X-RAY ring for two tunes of this storage ring: solid curves≡OPTICS tune; dashed curves ≡HIGH-β tune. The divergences follow Gaussian distributions and it is the half-width values that are plotted here.

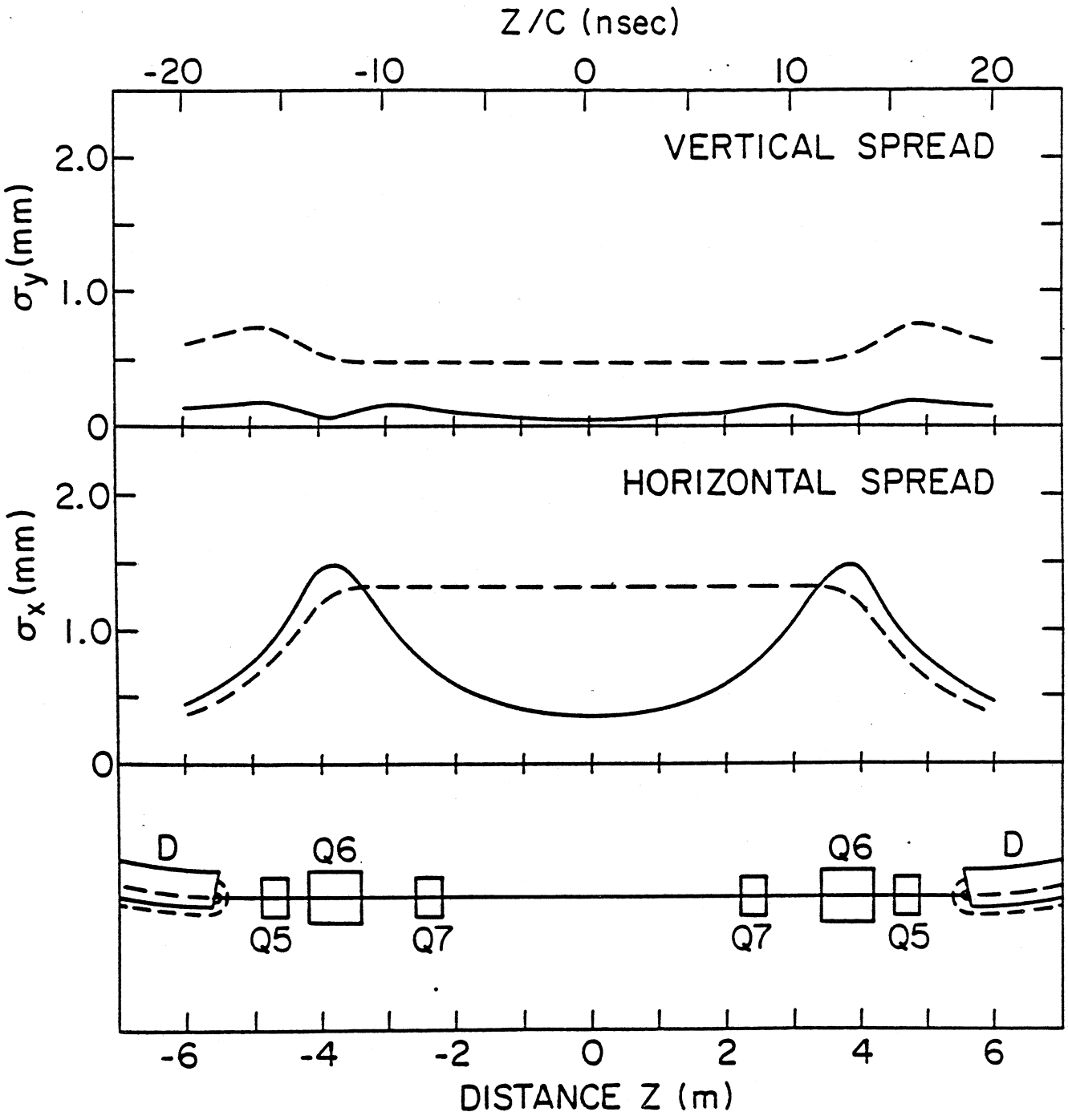

FIG. 14: The horizontal and vertical dimensions of the electrons in a straight section of the NSLS X-RAY ring. (See caption to Fig. 13.)

is shown in Fig. 15(a). The calculation has been performed for an Ar-Ion laser operating at 3511 Å with a beam-radius half-width σ_L=0.3 mm, and 2.5 GeV electrons stored in the "OPTICS" tune. The γ spectrum extends from 298 MeV down to 68 MeV, the photon energy that results from scattering through 4×10^{-4} radians, and tails off below this point. If the collimation angle is reduced to 2.4×10^{-4} radians, the minimum horizontal divergence of the "OPTICS" solution (Fig. 13), then the spectrum shown in Fig. 15(b) is obtained. The photon energy (135 MeV) corresponding to a scattering angle of 2.4×10^{-4} radians is indicated by the arrow, and the spectrum tails considerably below this point. If the electron beam-spot size were negligible at the interaction point, and if all electrons were diverging from this point with the same angle, then the photon scattering angle could still not be defined by collimation to better than this angular divergence (Eq. 2.2). With the Gaussian distributions of vertical and horizontal divergence shown by the solid lines in Fig. 13 (OPTICS tune), the fraction of γ rays transmitted by a circular collimator changes with collimation angle. For example, when the collimation is reduced from the case of Fig. 15(a) to that of Fig. 15(b), the transmitted flux drops by 48%. Proportionately more of the lower energy photons are removed by the smaller collimator. The fraction of tagged γ rays transmitted by the collimator differs by only 35% between the cases of Figs. 15(a) and 15(b). This fraction is shown as a function of collimator half-angle in Fig. 16. The untagged γ rays are <u>always lower in energy</u> and can be logically removed from the spectrum by an electron-veto counter in the tagging spectrometer (see section III.4). The tagged γ-ray flux transmitted by the collimator of Fig. 15(b) is

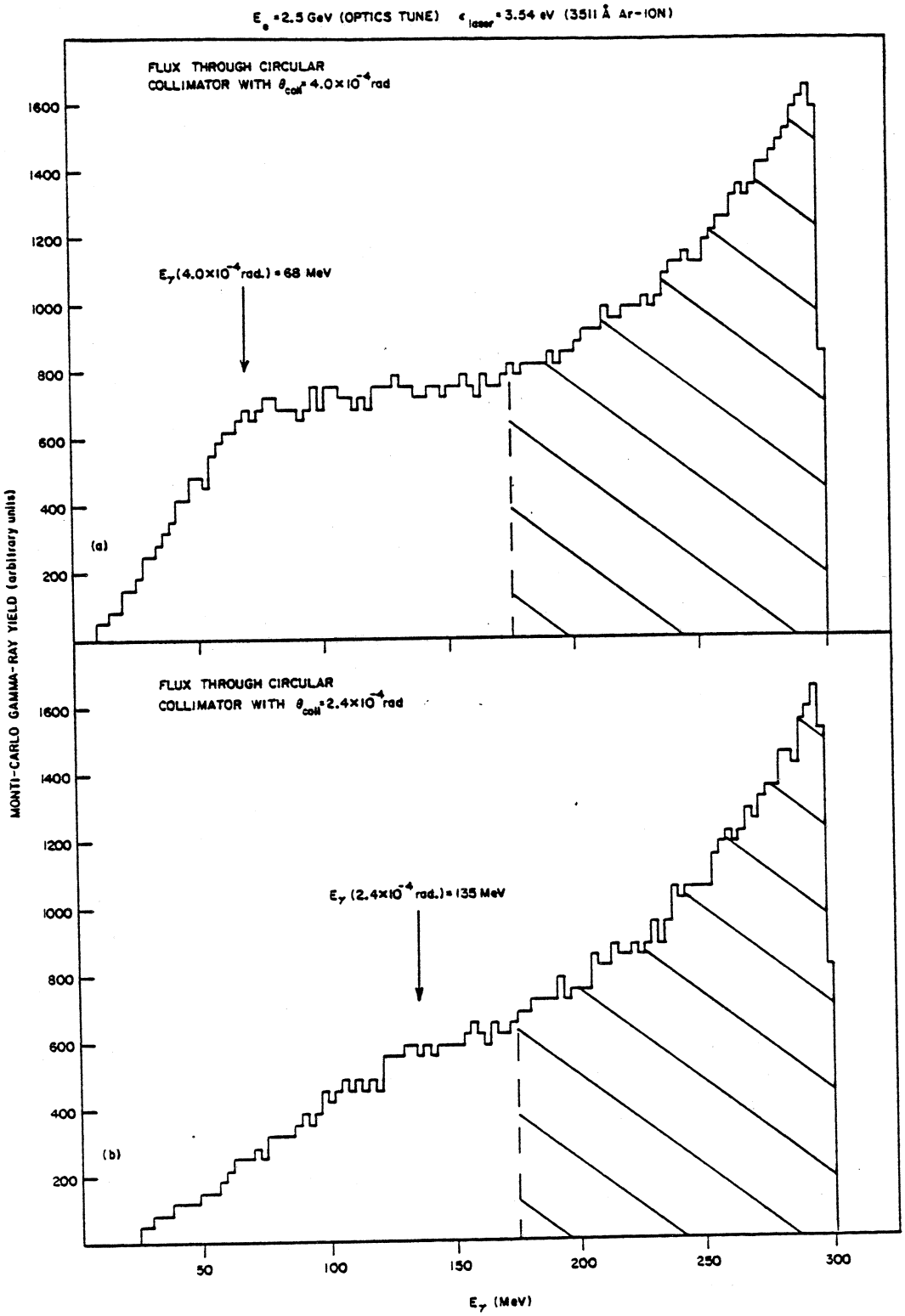

FIG. 15: Monte-Carlo calculations of the γ ray spectrum transmitted by 2 different collimators. The calculations include effects from the variation of the electron beam size and angular divergence along the interaction region. The tagged region of the spectrum is denoted by the hatched area.

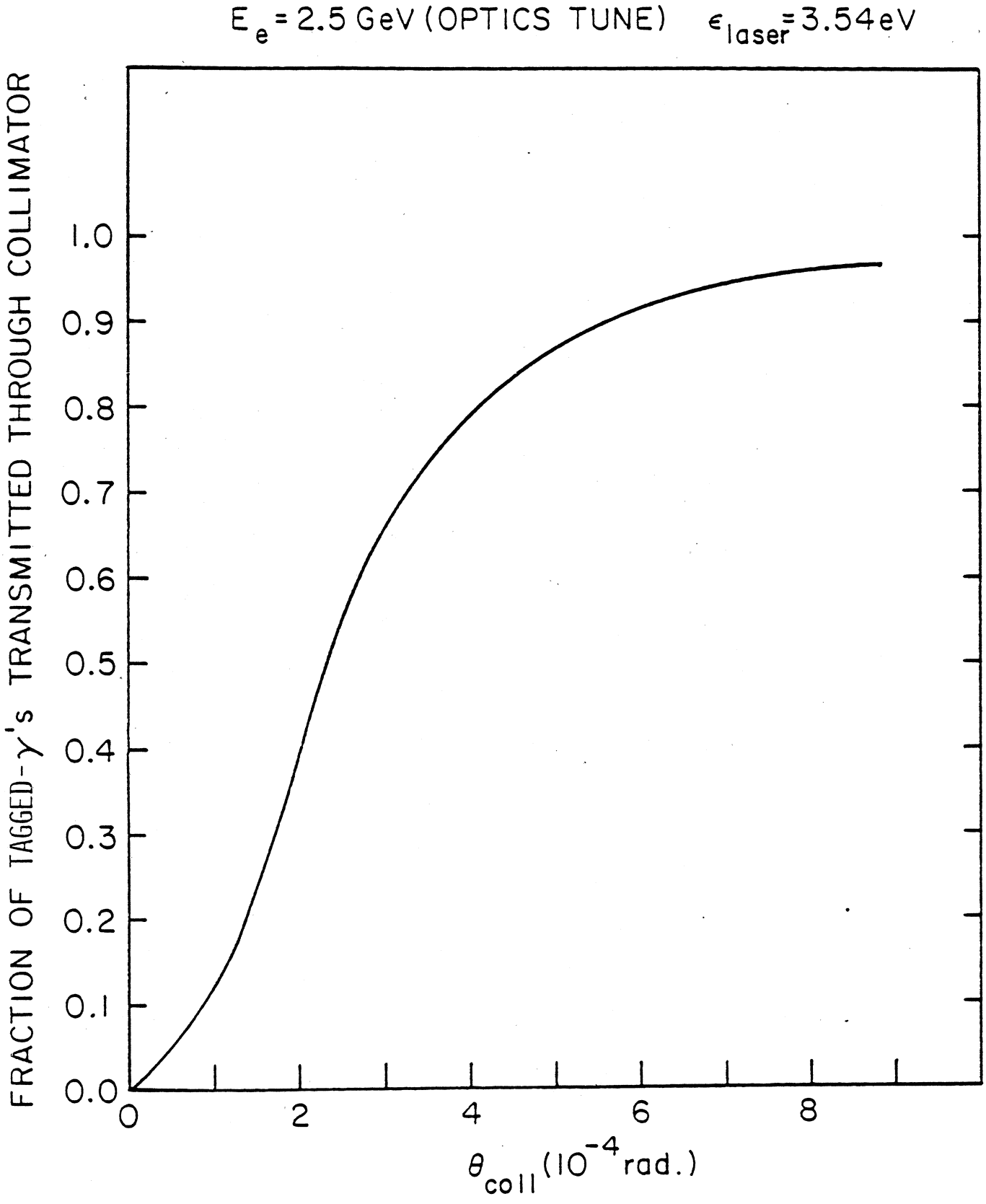

FIG. 16: The results of Monte-Carlo calculations for the fraction of tagged γ rays transmitted by a circular collimator. (See caption to Fig. 15.)

almost a factor of 2 lower than what would be predicted from Eq. (10) neglecting finite beam sizes and divergences.

Unlike the flux, the polarization of the γ rays is <u>not</u> appreciably affected by the finite divergences of the electron beam. This is simply because, for a given collimator geometry, the polarization is determined by the scattering angle. The partition of this scattering angle, between the angle from the γ ray direction to the axis of the straight section and the angle with which the incident electrons diverge from this axis, is irrelevant. Thus, γ rays of a specific energy defined by a tagging window are associated with a specific scattering angle and, for a given collimation, have a predictable polarization. The linear polarization of the tagged flux of Fig. 15(a) is shown in Fig. 17(a). The results of this Monte Carlo simulation are indistinguishable from the analytical calculation of Fig. 7. The beam is greater than 75% polarized at all tagged γ-ray energies. The polarization can be further increased by replacing the circular beam-defining collimator with a rectangular aperture which is narrow in the direction of the electric vector of the initial laser light. This geometry is shown schematically in Fig. 10. In the calculation shown in Fig. 17(b) the vertical aperture has been reduced to the level of the vertical divergence of the electrons in the OPTICS tune. Although this costs a factor of about 2.5 in flux, the γ rays are now more than 90% polarized.

There are two modes of operation that will achieve, or nearly achieve, the maximum useful γ-ray flux that can be properly tagged (2×10^7 sec^{-1}). In both modes, the OPTICS tune is used at full

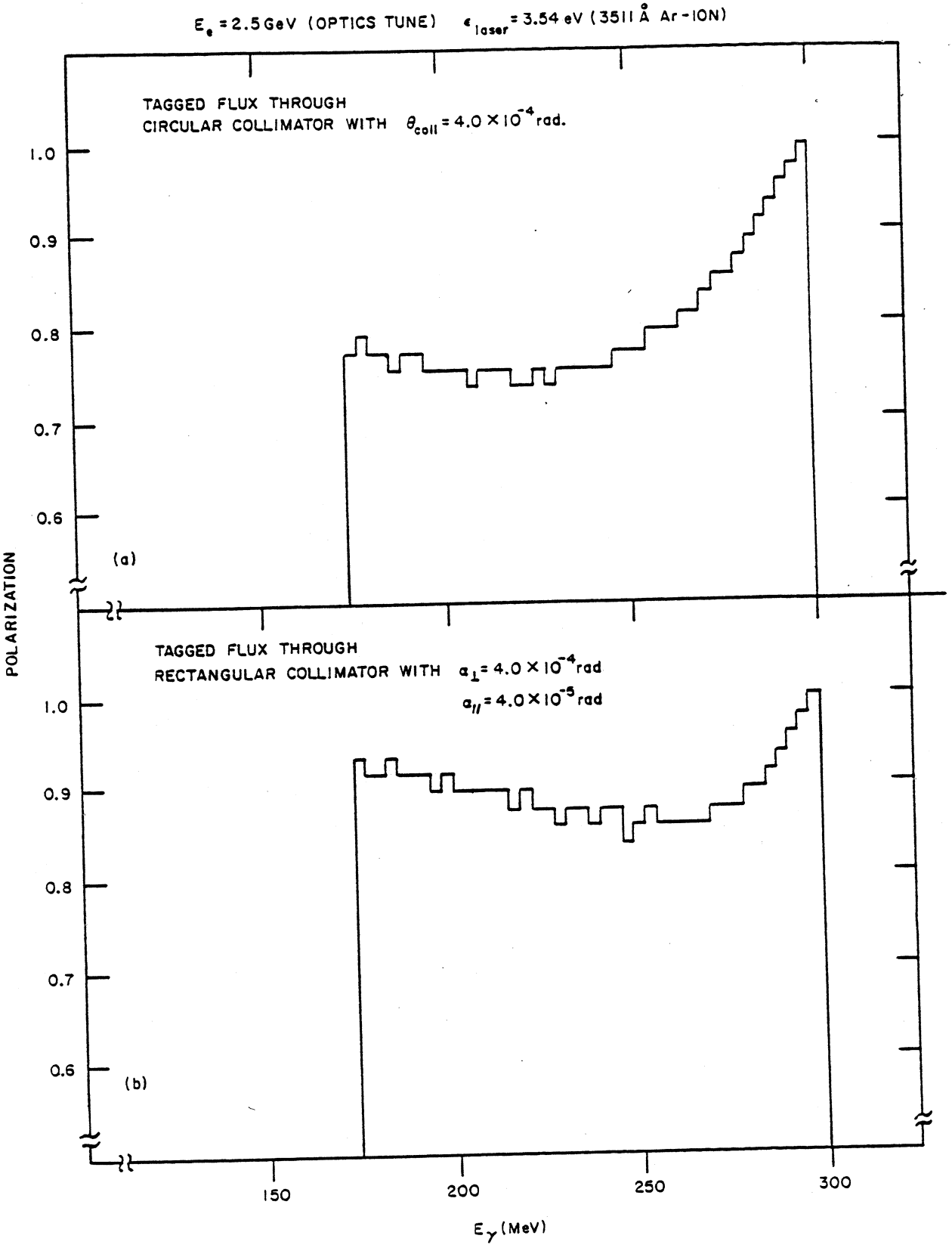

FIG. 17 : The results of Monte-Carlo calculations for the linear polarization of the tagged γ rays emerging from 2 different collimators. (See caption to Fig.15.)

current (0.5 amps) and maximum pulse rate (52.88 MHz),and the electron beam energy is fixed at 2.5 GeV (or 3.0 GeV in a later stage of the NSLS). The laser-backscattering facility operates as just another passive user of the storage ring.

PRIMARY MODE: The CW light from an Ar-Ion laser external to the storage ring is made to traverse the full length of the injection-straight section in the X-Ray ring. With 3 watts of CW power in the UV at 3511 Å (PHASE I), the total flux of tagged γ rays between 175 and 300 MeV will be 1.8×10^{7} sec.$^{-1}$. The average number of tagged γ rays per electron pulse is then $\bar{N}=0.34$, and the probability that there will be exactly one tagged γ ray per electron pulse is, from Eq. (8), equal to 0.24. The flux of useful tagged γ rays is thus $(0.24)\times(5.288\times10^{7}) = 1.28\times10^{7}$ sec^{-1}. If these γ rays are collimated to 4×10^{-4} rad, then the fraction of these transmitted to the nuclear target is 0.78 (Fig. 16), which leads to a useful tagged flux on target of 1.0×10^{7} sec^{-1}. In this case, the total number of electrons removed from the beam is 4.3×10^{7} sec^{-1}, which implies a lifetime of 13 hours for the 2×10^{12} stored electrons of the X-RAY ring. This is significantly longer than the expected lifetime of the ring due to other effects and will not seriously affect other users of the NSLS. In PHASE II, a 7 watt UV laser will be installed to bring the useful tagged flux up to its maximum value of 2×10^{7} per second. For planned experiments requiring 200 MeV γ rays, the same Ar-Ion laser operating in the visible around 5100 Å,

can provide more than enough power (up to 20 watts CW) to produce the maximum useful tagged flux between 175 and 211 MeV.

In certain cases, an experiment may require a very high flux of γ rays (per MeV of bombarding energy) over a relatively narrow dynamic range. This could be accomplished by restricting the active range of the tagging spectrometer, and increasing the laser power to bring the tagged flux back up to its maximum value.

SECONDARY MODE: The Ar-Ion laser is again operated CW, but the optical cavity is stretched to include the entire straight section. The electrons then collide with the internal laser power which is at least a factor of 10 higher than that external to the cavity. Although the laser cavity is quite long, this is not expected to pose any serious problems, particularly since reliable operation of just such a laser with a 17.5 meter optical cavity has already been demonstrated at Frascati. The increased laser power in this mode of operation would lead to a reduction in the lifetime of the stored beam to about 1 to 2 hours, and thus may conflict with other users of the NSLS.

For the experimental medium-energy physics program outlined in section IV, only the primary mode of operation is planned.

III.4 Gamma Ray Facility

A. Beam Line

A general layout of the National Synchrotron Light Source is shown in Fig. 18. The 2.5 GeV "X-RAY" storage ring has a total of 8 straight sections. Although the laser backscattering facility requires one of these, the only thing which would actually occupy the straight section is a laser beam. Thus, the injection straight, which is unusable for either wigglers or undulators, can be utilized for high-energy γ-ray production. The γ rays would emerge from a 0° port on experimental line X5, pass through a vacuum window, be transported through the building within a pipe holding a rough vacuum, pass through a hole in the exterior wall, and be stopped in a shielded dump outside. The floor space within the existing building which is allocated to this beam line is shown by the hatched area in Fig. 18. Because the γ-ray beam is extremely well focussed by the Lorentz transformations and because the total flux, although large compared to other medium-energy sources, is still only a milliCurie, the radiation level outside of this hatched area will be extremely small and will not hamper other users of the NSLS. In particular, the adjacent 10°-X6 synchrotron radiation line may still be utilized, if desired. (Gamma and neutron radiation monitors will be connected in series with the laser power supply and would interrupt the beam if high radiation levels were produced.)

A closeup of the straight section is shown in Fig. 12. Zero degree vacuum ports would be installed on the magnets at either end of the straight. The 0° port on the dipole farthest from the laser,

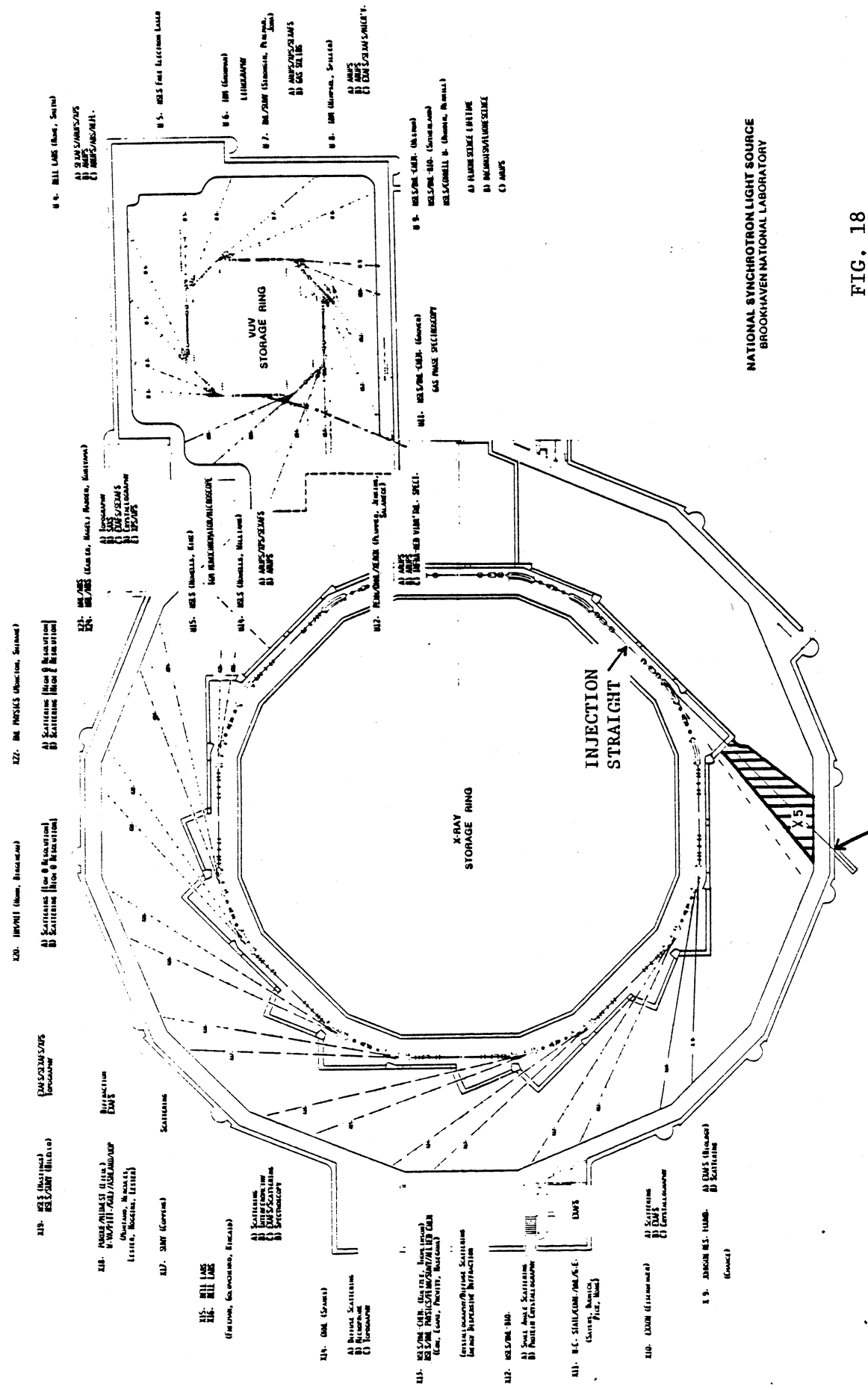
NATIONAL SYNCHROTRON LIGHT SOURCE
BROOKHAVEN NATIONAL LABORATORY
VUV
STORAGE RING
X-RAY
STORAGE RING
INJECTION
STRAIGHT
X5
Y-RAY LINE

FIG. 18

essential in the SECONDARY MODE of operation (section III.3), is still necessary in the PRIMARY MODE for alignment and for monitoring the laser power and spot size. Brewster windows, oriented to allow plane-polarized light to pass through with less than 0.7% absorption, would be used on these ports to separate the ultra high vacuum of the machine from the rough vacuum of the γ-ray line. The light from the laser, mounted on an optical bench outside the shielding wall, would be deflected by front-surfaced mirrors down the length of the straight section. The resulting backscattered γ rays would pass through the optical elements and continue to the nuclear target area.

B. Optical Transport

A detailed layout of the optical elements is shown at the bottom of Fig. 19. Two lenses, labeled with their focal lengths f_1 and f_2, are positioned to minimize the laser spot size within the straight-interaction section. In Phase I, a Spectra Physics 171 Ar-Ion laser would be used. The laser beam would be cylindrically symmetric, and its power would fall off radially as a Gaussian. The calculated half-width of this distribution (σ_L) is shown at the top of Fig. 19 as a function of path length, Z=0 marking the center of the straight section. (If necessary, this optical transport system can also be used in the SECONDARY MODE of operation by replacing the front mirror of the laser with another mirror located at Z=+9.5 meters, thus forming a 29.1 meter optical cavity.)

The alignment of this optical system is relatively straightforward. The alignment points on the optical bench (Fig. 19-bottom) must be located along the axis of the straight section and

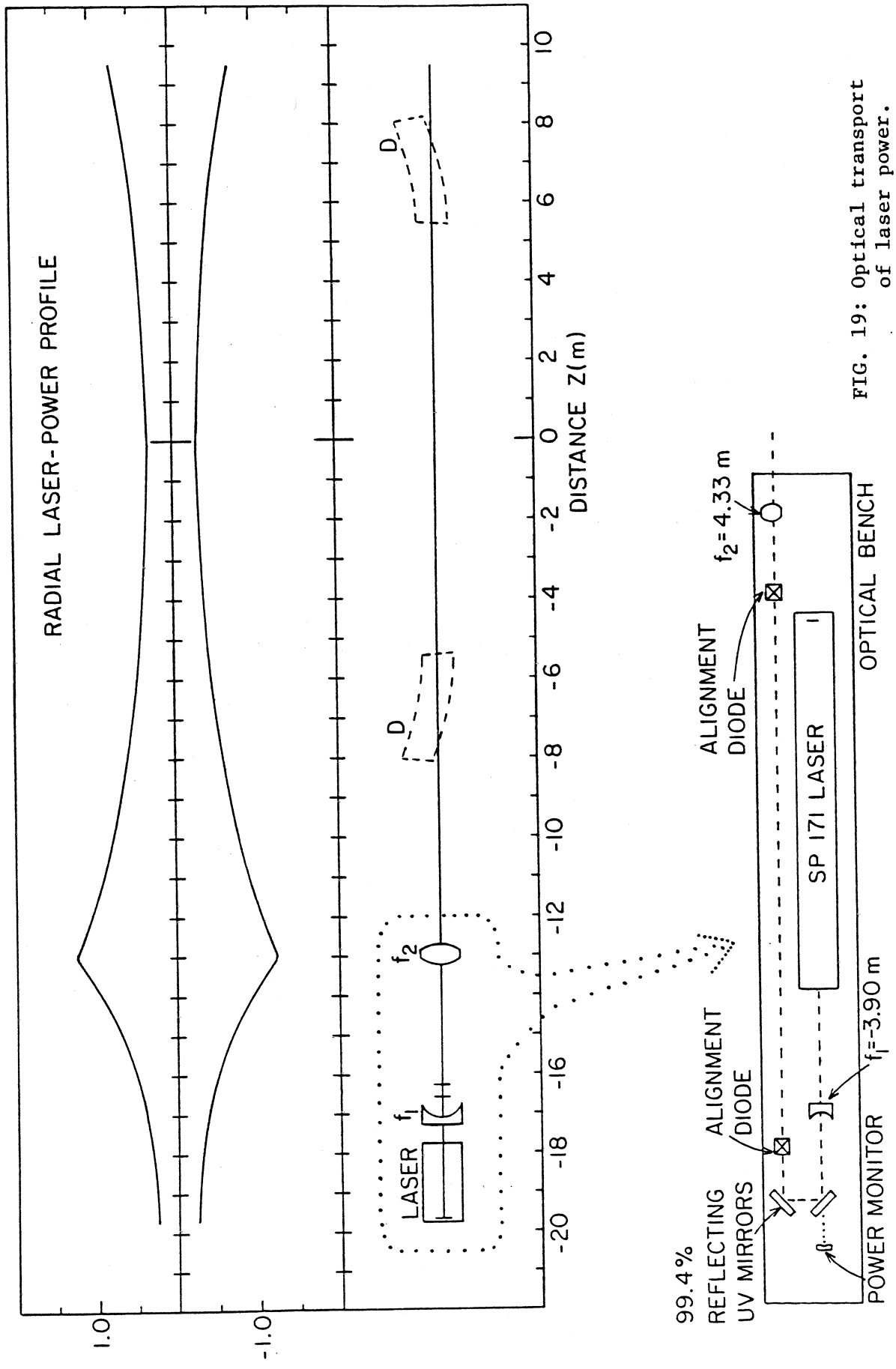

FIG. 19: Optical transport of laser power.

the 0° ports of the dipole magnets. Once this has been done, x-y position sensitive diodes may be mounted on top of these points, and the laser beam can be centered on this axis by adjusting the two mirrors at the end of the optical bench. With the alignment diodes removed, a power density monitor can be centered on axis at the opposite end of the straight section (Z=+9.5m). The two lenses can then be inserted on the optical bench. The tilt of these lenses must be adjusted to keep the beam centered at the positions of the alignment diodes as well as at the power monitor (Z=9.5m). To facilitate this procedure, the mirrors and lenses will be mounted on computer-servo-controlled precision goniometers, capable of rotating in two planes. With the readouts from the alignment diodes and power monitors fed back to a microprocessor, the optical system can be tuned automatically. The line defined by this laser beam determines the direction of the γ rays and the position of the nuclear target. Thus, the normal mode of operation will be to fix the orientations of the optical elements at their pre-optimized values, and move the electron beam with correcting coils to peak the γ ray flux on target. Such adjustments are expected to be very small and will not alter the synchrotron source positions at other points in the ring.

C. Tagging Spectrometer

The "front-end" region of the proposed laser-backscattering line, together with the tagging-spectrometer magnets, are shown in Fig. 20. (The 10°-X6 synchrotron radiation line is not shown here. It could emerge from magnet D1, the dipole immediately following the injection straight section.) There are two collimators that restrict

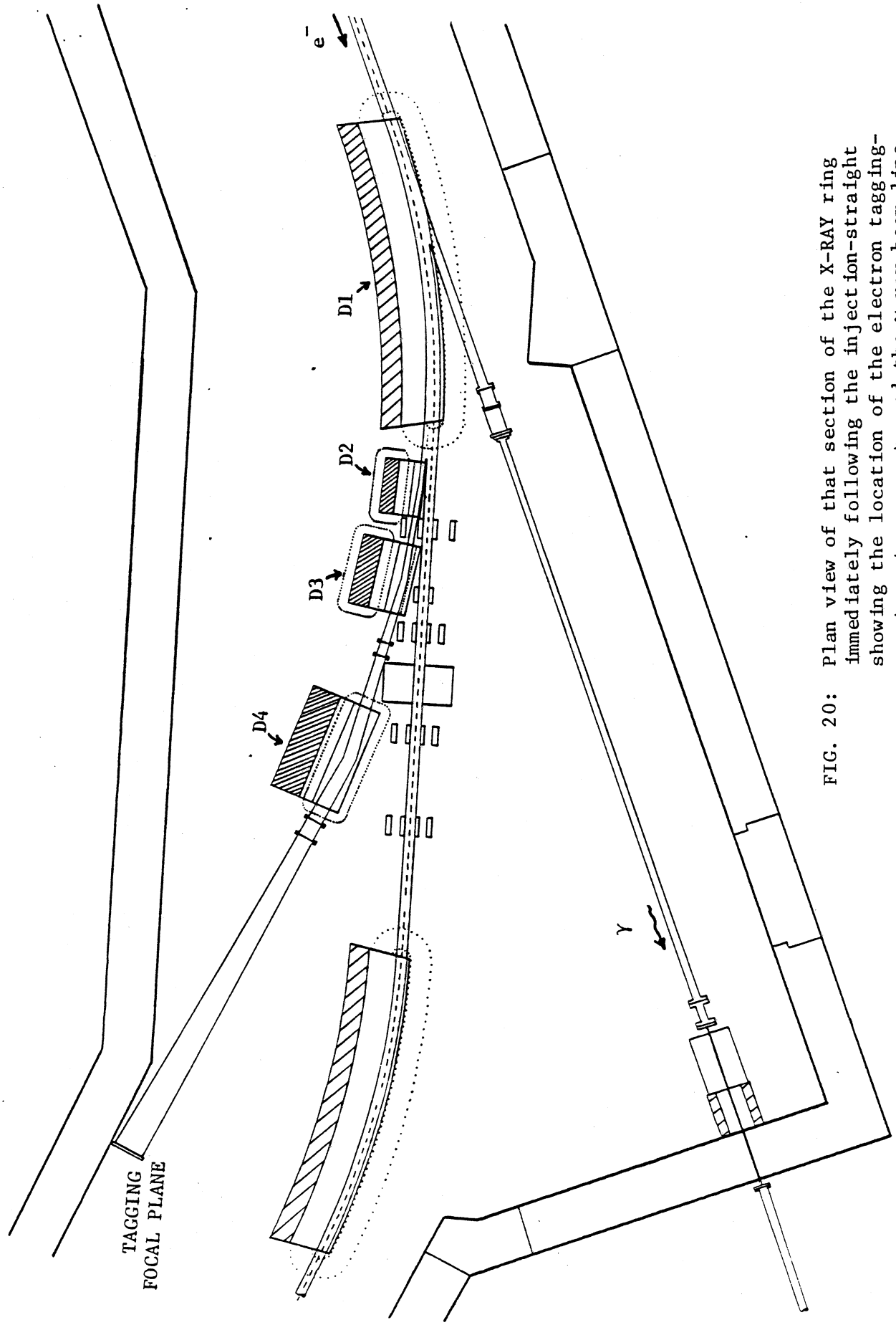

FIG. 20: Plan view of that section of the X-RAY ring immediately following the injection-straight showing the location of the electron tagging-spectrometer magnets and the γ-ray beam line. The laser-electron collision region is off to the upper right of the figure.

the angle of the emerging γ rays to those that have a high enough energy to be tagged. The first of these is shown in Fig. 20, just inside the existing shielding wall, and is followed by a magnet which serves to clear away charged particles created by showers in the collimator. The Brewster window separating the ultra-high and the rough vacuum regions is located immediately before the collimator. Pumping stations are positioned just before this window and at the exit of dipole 1. A high-vacuum and a fast-acting valve would also be located at this 0° port.

Electrons that lose energy by producing high-energy γ rays would be displaced from the primary stored beam at the exit of the existing dipole magnet (D1 in Fig. 20). This dipole maintains a field of 12.13 KG over its 2.7 m length, and produces a dispersion of 0.65 cm/% at 0.35 m from its exit face. This dispersion is large enough to allow a second dipole (D2 in Fig. 20), with a thin (4 mm) current-sheet septum, to be located just outside the existing ring vacuum chamber. This second magnet would then accept all Compton-scattered electrons with momenta of 2.32 GeV/c or less. These electrons would then be further deflected in the fields of the magnets labeled D2, D3, and D4 and transported to the focal plane of the "spectrometer", defined by magnets 1 through 4 of Fig. 20. The drift section between D4 and the focal plane would simply be a piece of pipe with a thin Al or Ti window ending just in front of the focal plane detector. This entire line would be maintained at the ultra-high vacuum of the ring. A high vacuum valve and pumping station after magnet 4 would allow, whenever necessary, easy decoupling of this pipe that crosses the access corridor between the shielding walls. A

second high vacuum valve and pumping station, together with a fast acting valve, would be located just after D3, and would permit the removal of magnet D4, together with the drift section, if access for large pieces of equipment were needed. (Magnet 4 would be positioned with locating pins mounted in the floor.)

The region of the second dipole D2 is shown, enlarged, in Fig. 21. The vacuum chamber splits around the septum, forming a "crotch" which separates the ring chamber from the tagging line. The field in the 0.7 cm gap of D2 is 10.0kG, and the high permeability of the pole steel at this operating point, combined with the small gap, results in very small fringe fields from this magnet. However, because of its proximity to the primary beam, several precautions will be taken to reduce the residual field at the circulating beam to very low levels ($\int B \cdot dl < 10$ gauss·meters). First, a special pole tip design will be used to generate a more rapid fall of the fringe field than is obtained with conventional flat poles. This floating pole design (Th81) will reduce the fringe field at the circulating beam by at least a factor of 2 (to about 300 gauss). Then, the current-sheet septum will further cancel the field (to <100 gauss). Finally, multiple trimming coils will be located above and below the ring vacuum chamber. These coils will be arranged so as to allow the remaining field and its gradient to be cancelled at the circulating beam by adjusting the currents in the individual coils. Calculations of the magnetic fields for D2 have been performed with the code TRIM (Co74). In Fig. 22 the calculated field in the magnetic mid-plane is plotted as a function of transverse distance, to show the contribution of the various elements. Measurements made for a magnet with a

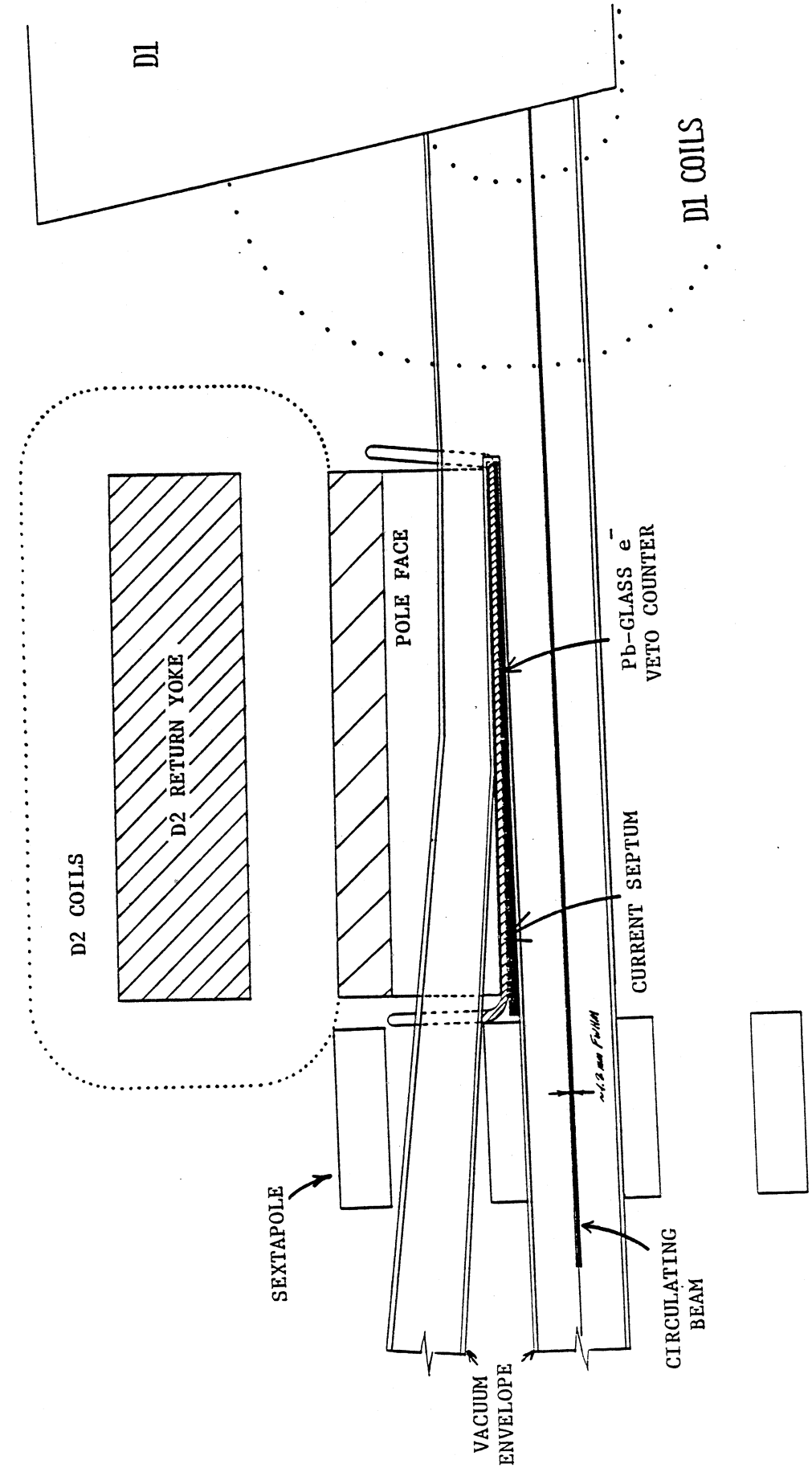

FIG. 21: Plan view of tagging spectrometer septum magnet D2 and the junction of the spectrometer and ring vacuum envelopes.

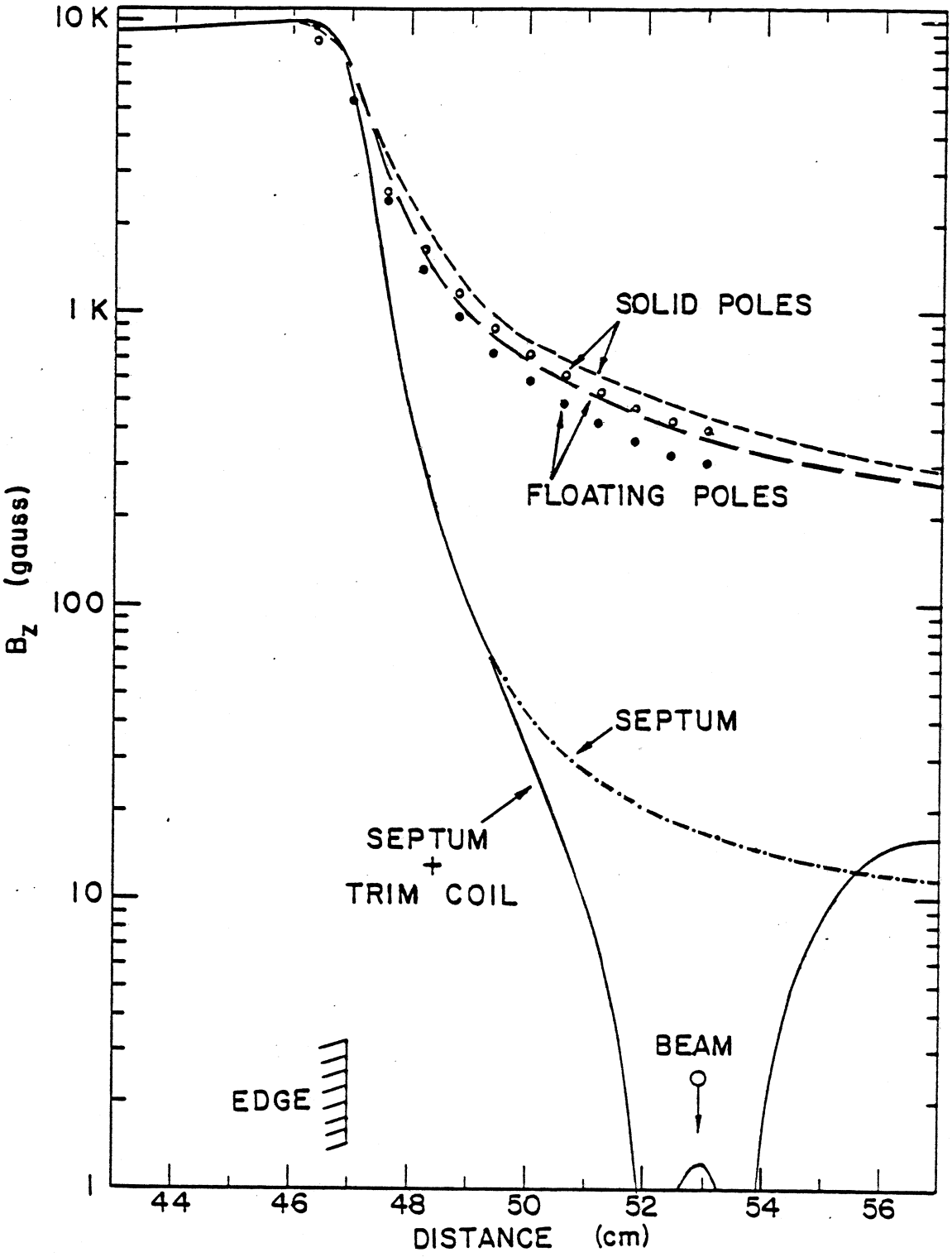

FIG. 22: Magnetic field in the midplane of D2 as a function of transverse distance. Calculations are shown for solid and floating pole geometries (short- and long-dashed lines); scaled measurements for these two poles are shown by open and solid circles, respectively. Calculations for the magnet with floating poles plus a current sheet septum, are shown as the dot-dashed curve. The behavior of the complete D2 assembly with floating poles, septum and trim coil is shown by the solid curve. The edge of the magnet and the position of the stored electrons are indicated at the bottom of the figure.

similar gap (1.1 cm) to that of D2 are also indicated in the figure. The field produced by the complete D2 assembly is shown by the solid line. The location of the stored electron beam is indicated by the arrow along the horizontal axis. A cross sectional view of D2 is shown in Fig. 23. This magnet and the auxiliary trimming coils will be built as an integral unit so that the entire system can be adjusted, before installation, to produce the desired field cancellation along the path of the circulating beam.

The only element of the existing ring-transport system that must be modified for the tagging spectrometer is the first sextupole following D2. The scattered beam passes through a gap in this element that already exists in the ring-plane. However, to extend the dynamic range up to the maximum energy γ rays (300 MeV), or equivalently down to the minimum scattered electron energy (2.2 GeV), it will be necessary to push the return yoke of the sextapole out further from its center, while leaving the pole-tips in the same positions. This will be done in a symmetric way so as to retain a pure sextupole field in the vicinity of the stored beam. In any case, this element provides only a second-order correction to the ring transport and this modification will have no effect on other NSLS users.

After passing through the sextapole, the Compton-scattered electrons are then further deflected and dispersed by the 17kG dipole D3. This magnet would be constructed with a septum wound inside its 1.0 cm gap at the outer edge. With this septum design, and with the greater distance of D3 to the circulating beam, adequate field cancellation can be achieved with magnetic shielding between this dipole and the ring. The scattered electrons are then further

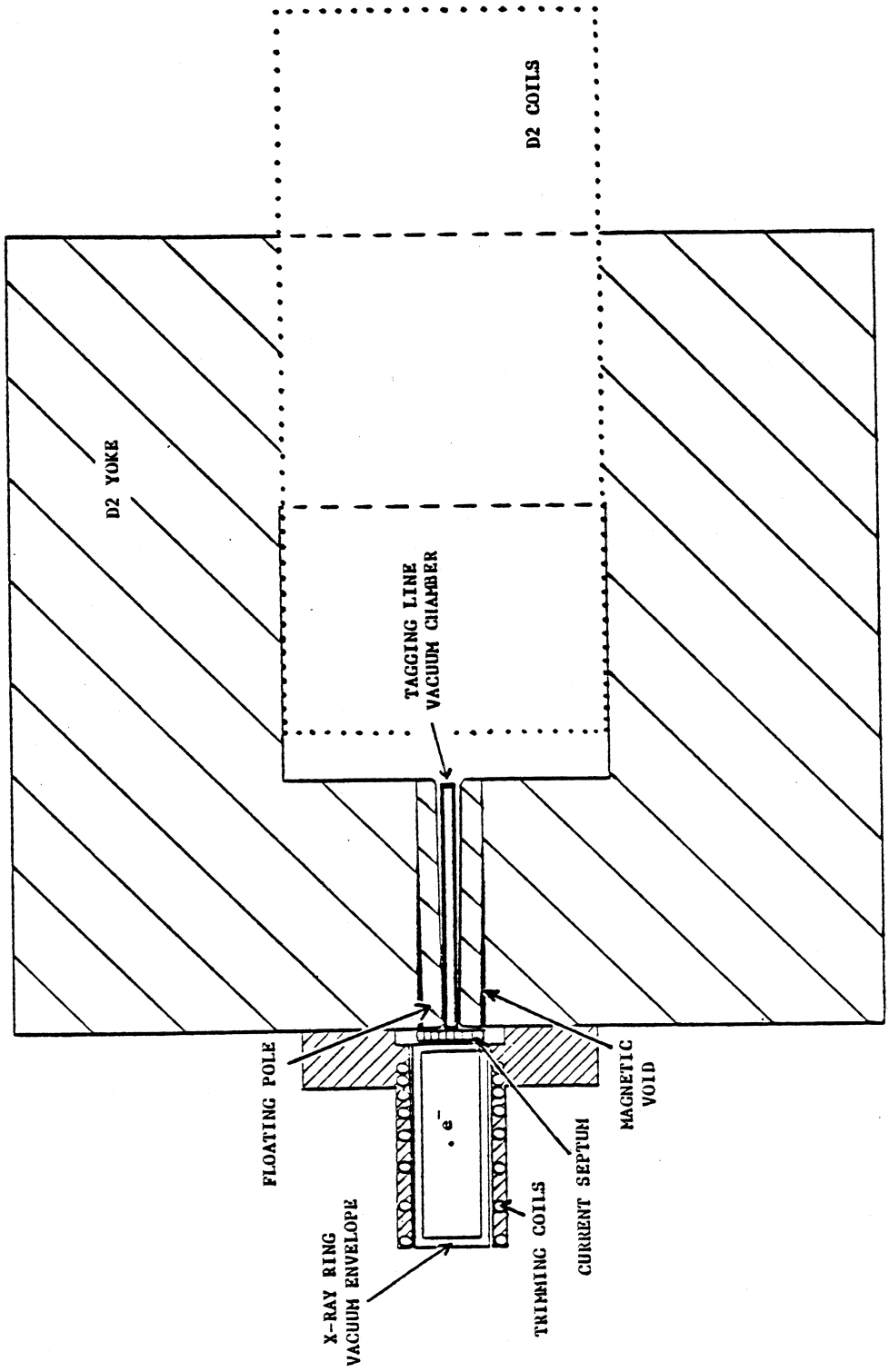

FIG. 23: Cross sectional view of tagging spectrometer septum magnet D2, indicating relative location of vacuum envelopes, septum and field trimming coils.

dispersed by the final dipole D4, which is a conventional "C"-type magnet operating at 17kG with a gap of 1.0 cm.

The mechanical and electrical properties of D2, D3 and D4 are summarized in Table I, and Fig. 24 presents the excitation curves for these three magnets. As indicated in Fig. 24, at 10kG, D2 is well below the "knee" in the magnetization curve of the steel, and the resulting large permeability of the yoke and poles (about 1800) helps to keep the fringe fields low. For the same reason the power consumption of this magnet is less than 1 kW. Dipoles D3 and D4 operate at a lower efficiency (above the knee in the magnetization curve) resulting in increased fringing and power consumption. However, as mentioned above, fringing is not a serious problem for these dipoles because of their greater distance from the circulating beam.

None of the magnetic elements D2, D3, or D4 would be any closer to the stored beam than the outside wall of the existing vacuum chamber. This design preserves the ±4 cm "stay-clear" aperture necessary for high current injection (NS82), and insures no interference with other NSLS users. All of these magnets would be powered by stabilized DC supplies. They would be at zero field during injection and would only be energized after the stored beam had reached 2.5 GeV.

The additional fields provided by magnets D2, D3, and D4 significantly improve the resolution of the spectrometer, and allows the Compton-scattered beam to clear the existing ring-line quadrupole. The drift that follows D4 then significantly increases the dispersion. Calculations of the optical properties of this tagging line have been

TABLE I

Specifications of NSLS Photon Tagging Line Dipoles

Parameter	D2	D3	D4
B(kG)	10	17	17
Length (cm)	48	60	95
Depth (cm)	35	50	62
Height (cm)	38	52	64
Gap (cm)	0.7	1.0	1.0
Turns*	96	144	144
Resistance* (Ω)	0.138	0.277	0.404
Ampere-Turns	5830	22,600	18,300
Current (A)	61	157	127
Voltage (V)	8.4	43.5	51
Power (kW)	0.51	6.8	6.5

*Assuming 1/4" square conductor, 50% area for cooling and insulation, and 2×10^{-6} Ω·cm resistivity.

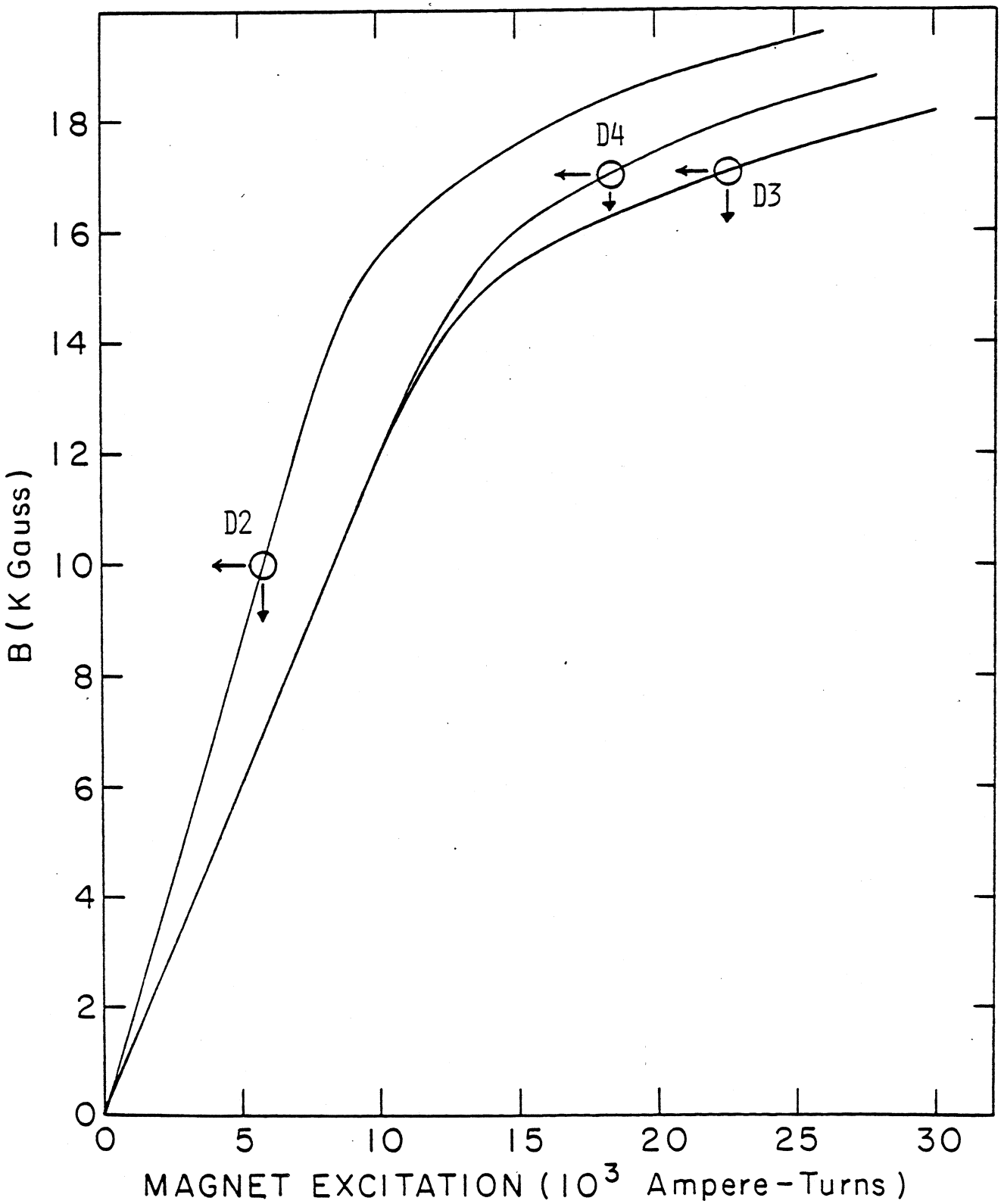

FIG. 24: Calculated excitation curves for the tagging spectrometer dipole magnets D2, D3 and D4.

made with the code TRANSPORT (Br70). Input phase space ellipses were taken from SYNCH calculations (NS82) for the circulating beam stored in the NSLS X-RAY ring. The computed spot size, dispersion, and momentum resolution of the Compton-scattered electrons are listed in Table II for the OPTICS and HIGH-β tunes of Figs. 13 and 14. The focal plane is 28 cm long, with an image size of about 4.8 mm (horizontal) x 0.5 mm (vertical). Estimates of second order aberrations indicate that they are negligibly small, principally because of the small divergence of the source. The optimum resolution of this spectrometer is about 1.9 MeV. Including the expected 0.08% resolution of the primary beam in the OPTICS tune (va80), the net electron (and hence tagged-γ) resolution will be 2.7 MeV, and this is almost constant throughout the acceptance range of the spectrometer.

The detector of the Compton-scattered electrons that reach the focal plane will be a lead-glass hodoscope consisting of two 48-element arrays, each element of which is 6 mm thick. The second array will be positioned behind the first and offset 3 mm. The signals from the photomultiplier tubes viewing the Pb-glass elements will be passed to fast-discriminators and then input to four 24-bit coincidence latches. These latches will be strobed by a signal indicating the detection of a nuclear-reaction event in fast coincidence with a common "OR" from the hodoscope. This strobe will subsequently cause the bit-patterns from the latches to be read by the computer. Logical coincidences between two detectors, one from each of the two 48-element arrays, will be used to reconstruct a net 3 mm position sensitivity. The bit-patterns will also be examined to determine the number of such 3 mm bins that contained an electron.

TABLE II

Tagging-Spectrometer Performance

Tune	ΔX_{FWHM} (mm)	ΔY_{FWHM} (mm)	D (cm/%)	$\Delta E/E$ (%)
OPTICS	4.77	0.51	4.902	0.097
HIGH-β	4.21	0.83	4.902	0.086

Such Compton electron + nuclear reaction events in coincidence will be relatively rare so that the dead-time associated with reading the latched words will be negligible. Furthermore, since the latch bits can only be set after receiving a nuclear strobe, until such an event occurs the latches are always alive. The use of Pb-glass, which not only produces extremely fast signals but is also very insensitive to electron energies less than about 80 MeV, insures very low background levels in the hodoscope. In addition, the requirement that an electron pass through one detector in the first 48-element array, and then through a specific detector in the second array, ensures that the electrons which are detected have actually come through the tagging spectrometer, and not from some other point in the ring.

It should be possible to logically remove the untagged portion of the γ-ray spectrum reaching the nuclear target (low energy regions of Fig. 15) by detecting the presence of the associated electrons that are below the acceptance window of the spectrometer (E_e>2.32 GeV). These electrons will pass through the inner edge of the storage-ring vacuum envelope and can fire a thin Pb-glass strip placed outside the aluminum pipe. Such a detector is shown in the region of the crotch of D2 in Fig. 21. When this is used in anticoincidence with the nuclear strobe, essentially every γ ray reaching the nuclear target will either be tagged or rejected.

D. Nuclear Target Area

The PHASE I experimental area is shown in Fig. 25, together with that portion of the X-RAY ring used in the laser backscattering. A second collimator, slightly smaller than the first, would be housed

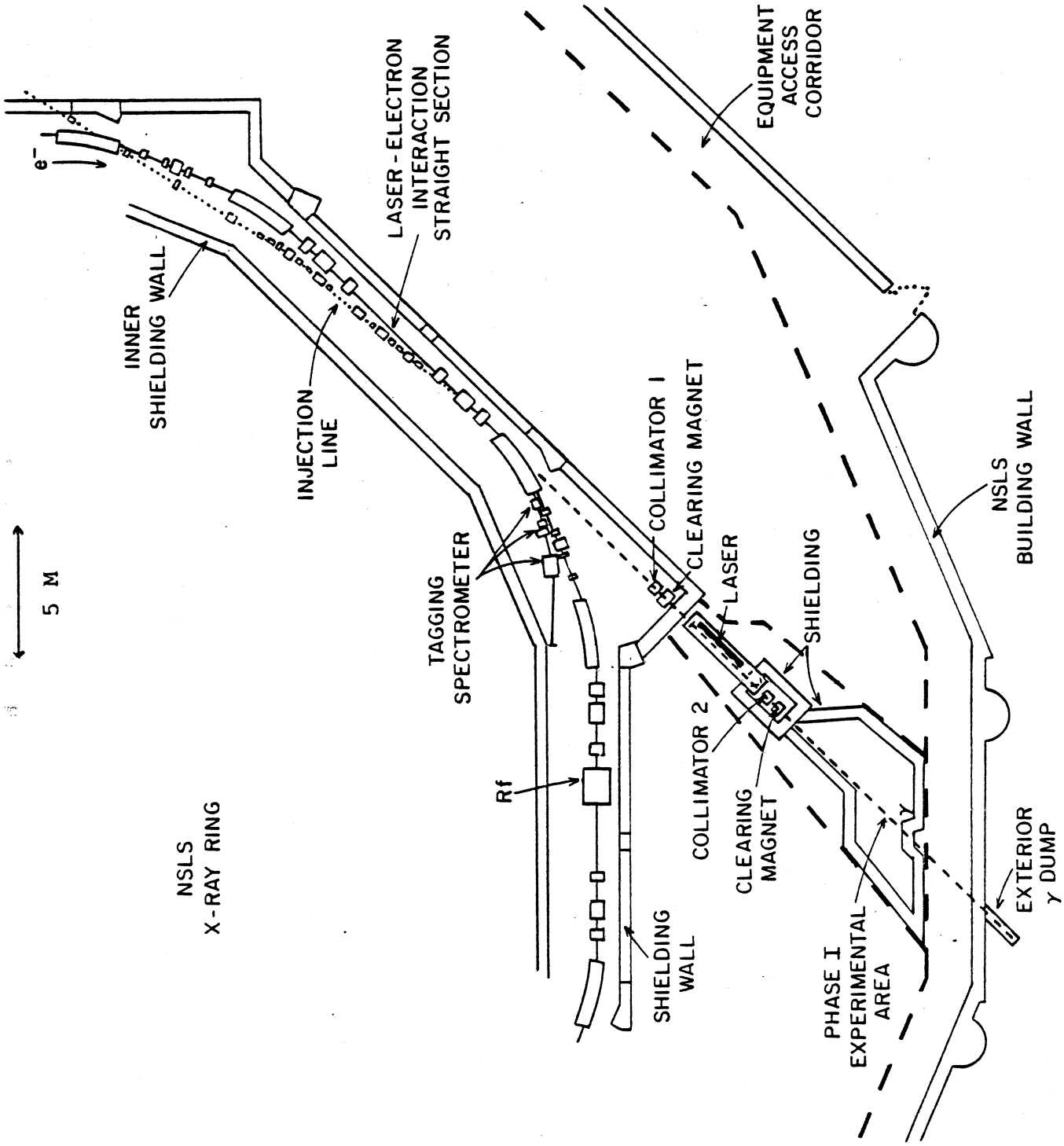

FIG. 25: PHASE I γ-production and experimental areas.

in a shielded area located immediately after the optical bench. Laser optics controls, a small computer, and minimum nuclear electronics, can be accommodated next to this area. The nuclear target would also be shielded and the remaining floor space, still within the heavy-dashed lines in Fig. 25, is just sufficient for either the absorption or one of the γ-ray detectors necessary for the PHASE I tests and experiments. These detectors can be maneuvered to this X5 floor area along the outer "equipment access corridor". A γ-beam line valve located immediately before this corridor would allow the rapid removal of the pipe that extended to the dump whenever access across this region was necessary.

The equipment necessary to detect the reaction products of medium-energy γ rays, pions for example, cannot be accommodated in the PHASE I experimental area. Furthermore, the NSLS does not have an overhead crane and the outer access corridor is simply too narrow to be used for moving large magnets. The lack of space is so severe that an extension to the building is absolutely essential.

The preliminary design of an extension to the existing NSLS building is shown in Fig. 26. The second beam-defining collimator and clearing magnet would now be located at the entrance corner of this γ-ray lab. This extension would provide room for a small target area for γ-ray scattering and absorption detectors, followed by a second larger target area that could accommodate two magnetic spectrometers. Once again, the beam would ultimately penetrate the exterior wall and be stopped in a shielded dump outside. A loading door and platform on the outside wall of this extension would allow access for large pieces of equipment. A separately shielded area would house the electronics

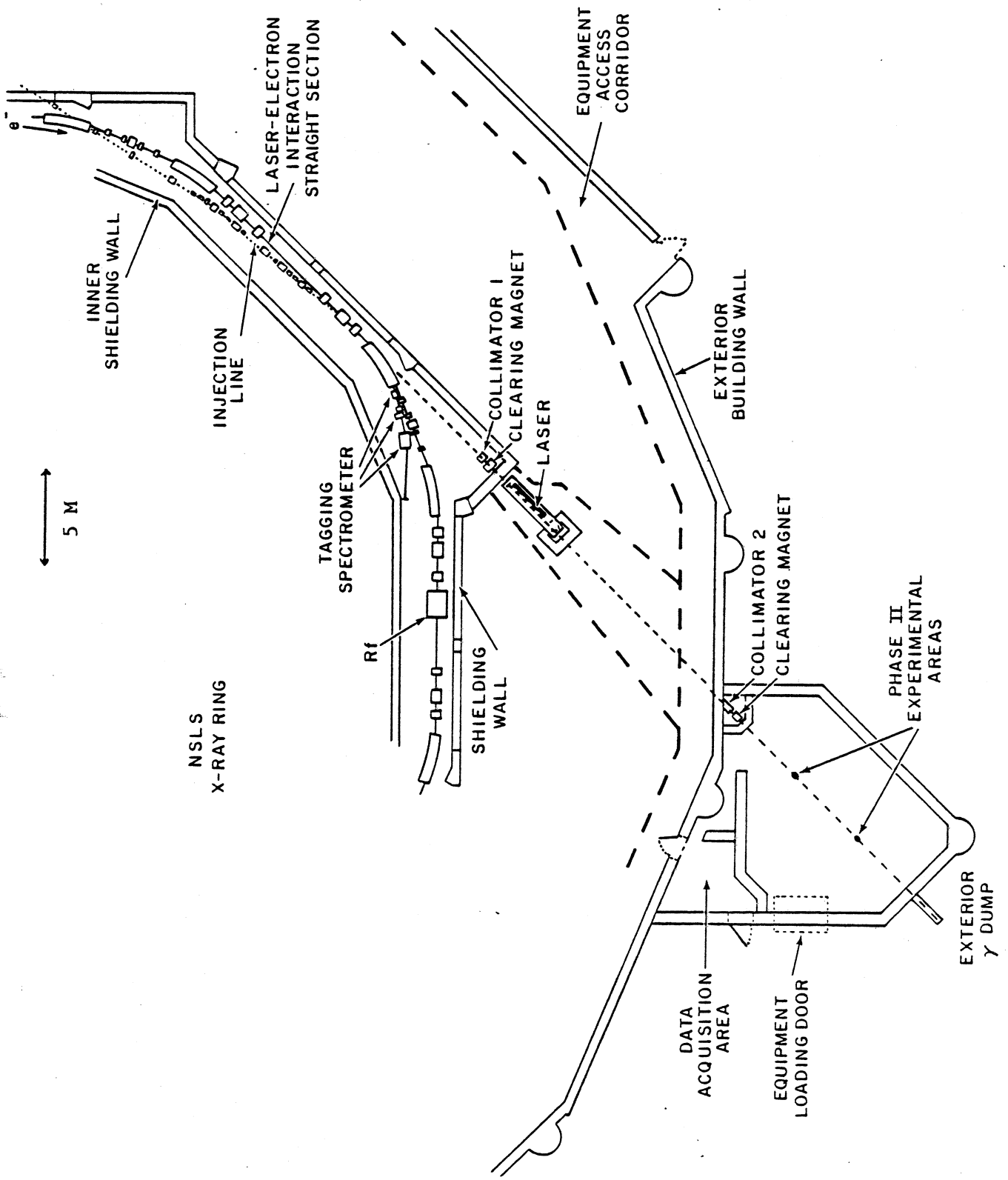

FIG. 26: PHASE II γ-production and experimental areas.

and data acquisition computer, and access to the main NSLS building would be through this area. The construction of this external γ-ray lab is planned for PHASE II of this project.

III.5 Extension to 500 MeV with the Free Electron Laser Coupling both VUV and X-Ray Storage Rings

The 300 MeV limit on the γ-ray energy during the phases of operation discussed in the previous sections arises from a lower limit of 3500 Å on the wavelength of the laser light used for backscattering at 2.5 GeV. (The corresponding limit for 3.0 GeV operation of the X-RAY ring is 420 MeV.) Lower wavelengths are commercially available by frequency-doubling Ion lasers or Ion-pumped Dye lasers. However, such devices can operate with high duty-cycles only at power levels that are about 10^3 times smaller than the Ar-Ion laser. The corresponding reductions in γ-ray flux would result in a beam of limited usefulness.

The only way to decrease the laser wavelength, and thus increase the γ-ray energy, while maintaining a power level sufficient to produce a high γ-ray flux, is to use a Free Electron Laser. A Free Electron Laser (FEL) is a rather new device (E176) in which photons and electrons together traverse a periodically varying magnetic field. The presence of the electrons inside this undulating field stimulates the emission of more photons of the same wavelength. This arrangement is shown schematically in Fig. 27. The electron beam enters the straight region from the left and produces synchrotron radiation in the undulator. The electrons are then swept away by a dipole magnet while the synchrotron photons pass through a 0° port on this magnet and are reflected back by a mirror. These photons travel back through the undulator region and are ultimately reflected by a second mirror. If the next electron bunch is timed to coincide with these photons when both are traversing the undulator in the same direction, then

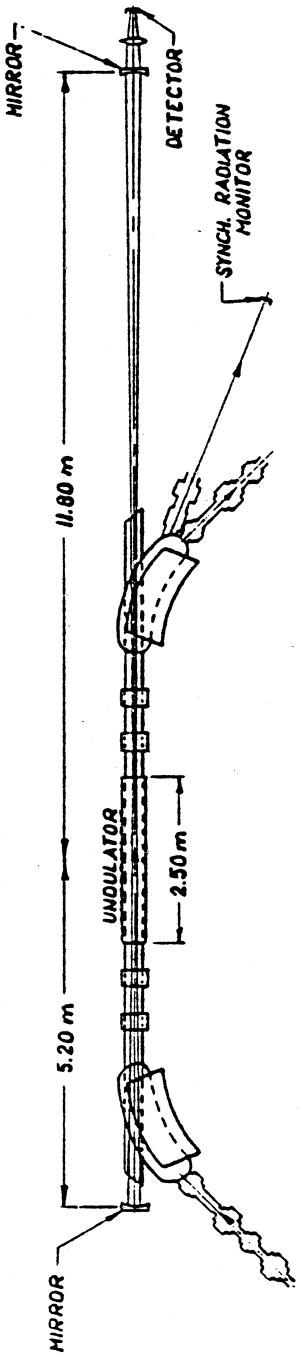

FIG. 27: Plan view of the Free-Electron-Laser under construction at one of the straight sections of the VUV ring.

there will be a net gain in the photon intensity and, after enough passes, the linewidth of the radiation will collapse. This will be accompanied by a decrease in the average energy of the electrons leaving the region of the undulator. For a simple description of how energy is transferred from the electrons to the radiation field it is convenient to consider their interaction in the rest frame of the electron. Here the undulating magnetic field becomes a crossed electric and magnetic field approaching the electron. This electromagnetic wave can then backscatter from the electron, and the resulting scattered wave can be enhanced or stimulated by the incoming photons that, in the lab, are traveling in the same direction as the electrons. More detailed descriptions of the theory of an FEL are available in the literature (JMa73; JMa74; Re78; Re79; Pe80).

The wavelength of the photons emerging from an FEL is related to the periodicity λ_o of the magnetic field in the undulator and to the energy of the electron beam γmc^2 by

$$\lambda = \frac{\lambda o}{2\gamma^2}(1+K^2), \tag{12a}$$

where the parameter K is related to the r.m.s. magnetic field by

$$K = \frac{e\lambda o}{2\pi mc}\langle B\rangle_{r.m.s.} \tag{12b}$$

The power output of such a laser is an exponential function of the single-pass gain G, and this is related to the peak electron current I_p and electron-beam cross-sectional area Σ by (Re78;Lu81)

$$G = (\text{constants}) \cdot (\lambda_o \lambda^3)^{1/2} \frac{K^2 N^3}{(1+K^2)^{3/2}} \frac{I_p}{\Sigma}, \tag{13}$$

where N is the number of periods in the undulator. The gain in an FEL can be much higher than in a conventional laser. The first Free Electron Laser, developed on a linac, reported a gain of 7% for a peak current of 70 mA (El76). If the FEL is part of a storage ring where the peak currents can be as large as 100 Amps, the single pass gain could in principle be huge. However, the bunches that stimulate the laser emission during successive pulses would then be made up of the same electrons. Thus, the FEL can have a significant effect upon the stored beam. Detailed discussions of the interaction between an FEL and a storage ring are reported in refs. Re78, Kr79, Pe80, and LK 81.

The construction of an FEL on the U5 straight section of the VUV ring at the NSLS is presently nearing completion. The undulator is made up of permanent Rare-Earth-Cobalt magnets and contains N=39 periods, with a periodicity λ_o=6.5 cm (Bl81;Lu81). (This is the arrangement shown schematically in Fig. 27.) The undulator gap is adjustable, allowing K (Eq. 12) to vary from about 1.4 to 3.1. With these parameters, it should be possible to obtain wavelengths as low as 2000 Å with electron energies of 300 to 600 MeV in this storage ring. The expected average FEL-output-power levels are shown for different wavelengths in Fig. 28 with the scale on the left. The VUV-FEL will be operated with two photon bunches in the optical cavity and with three 0.5 ns electron bunches in the ring, each separated by 56.7 ns (17 meters). (To obtain this with a 52·88 MHz-Rf oscillator, only every third potential bunch is filled with electrons.) This time structure implies that the peak power during the laser pulse will be 113 times larger than the average level, and this is indicated by the scale on the right side of Fig. 28.

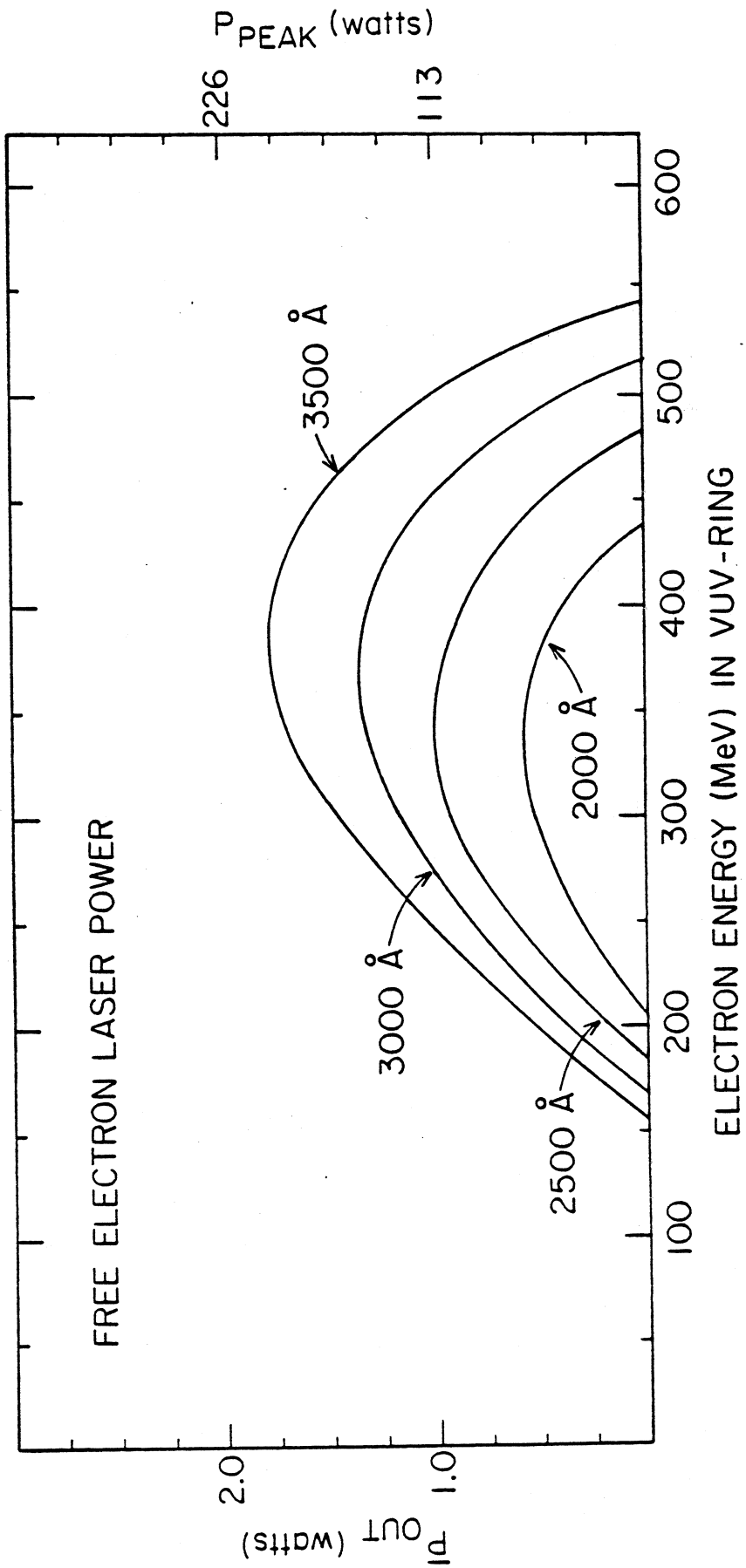

FIG. 28 : Expected average output-power levels for different wavelengths of operation of the FEL on the VUV ring. Peak power levels are indicated by the scale on the right.

One might imagine such an FEL mounted on the X-RAY ring with the resulting laser light arranged to backscatter from the 2.5GeV electrons to produce ultra-high energy γ rays. However, the factor γ in Eq. (12a) would then be 4900 and, since it is difficult to realize fields that would produce values of K much greater than about 3, low FEL wavelengths (2000 Å - 3000 Å) could only be produced with a λ_o=1 meter periodicity undulator. Such an undulator would require N=30 to 40 periods to obtain a gain (Eq. 13) comparable to the VUV-FEL. This length of straight section, free from optical elements, is certainly not available anywhere in the world. Furthermore, it would be virtually impossible to construct such an ~30 meter straight region, throughout which the electron beam area (Σ in Eq. 13) was small. The solution to this problem is unique to the NSLS at Brookhaven. Because of the proximity of the low-energy and high-energy storage rings, and because both rings can be run from the same Rf oscillator and thus synchronized in time, the light from the FEL on the VUV ring can be transported to the injection straight of the X-RAY ring and there, backscattered. The 87.5 meter optical path coupling the two storage rings is indicated in Fig. 29. The relative phase between the FEL-photon and X-RAY-electron bunches can be adjusted by simply translating a mirror, which then varies the optical path length.

Because of the time structure of the FEL, only every third X-RAY electron bunch will collide with a photon bunch in the middle of the straight section where the electron beam is smallest (Fig. 14). Nonetheless, taking this into account the 2000 Å power levels of Fig. 28 imply a total tagged γ-ray flux of 2×10^7 sec^{-1}, extending from 280 MeV up to about 500 MeV. (When the X-RAY ring achieves 3.0 GeV

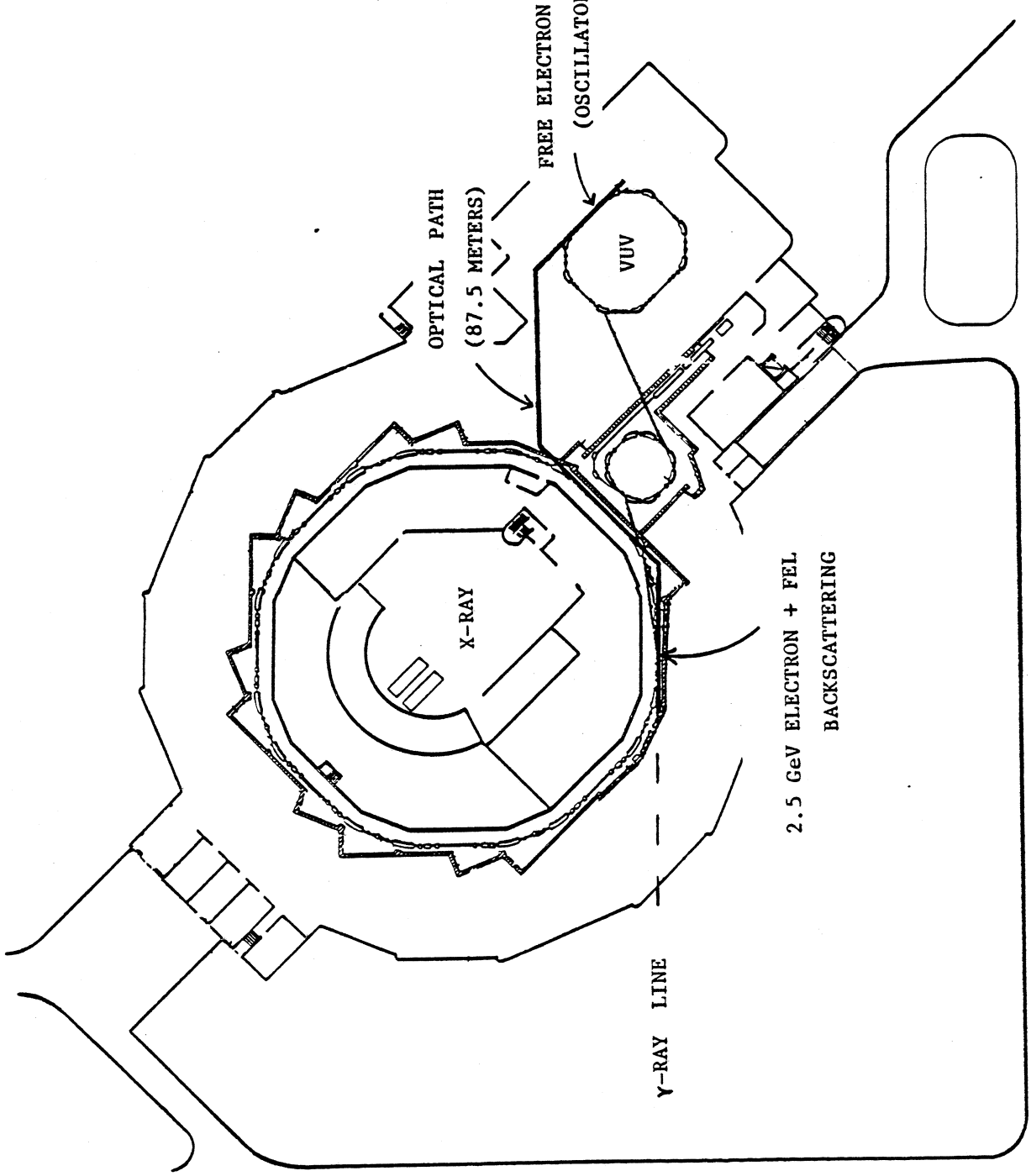

FIG. 29

FIG. 29: The optical path that would be used to backscatter the FEL light of the VUV ring from the electrons in the X-RAY ring.

operation, this tagged spectrum would be shifted up to almost 700 MeV!) This coupling of the two storage rings is planned for the third stage of our program.

III.6 Expected Low-Background Levels

There are only two potential sources of high-energy γ-ray backgrounds: small angle scattering in the beam-defining collimators and bremsstrahlung of the electron beam in the residual gas of the straight section.

As shown in Figs. 25 and 26, a magnet located immediately after each collimator serves to sweep away any charged shower particles produced by the γ beam striking the edge of one of these apertures. The first collimator cuts out most of the unwanted large-angle flux. The small size and divergence of the γ-ray beam makes it possible to locate the second collimator sufficiently far from the first to ensure that γ rays which scatter from the edge of the first collimator through more than about 10^{-3} radians cannot reach the nuclear target area. Whenever it is important to ensure that all γ rays reaching the nuclear target are either tagged or logically removed, a second collimator made out of Pb-glass can be used in anticoincidence, together with the Pb-glass veto counter shown in Fig. 21.

Bremmstrahlung of the electron beam in the residual gas of the vacuum pipe in the X-RAY ring injection straight can produce γ rays up to 2.5 GeV in energy, some of which will pass through the collimators to the nuclear target area. The energy integrated bremsstrahlung cross section is given by (Ja62)

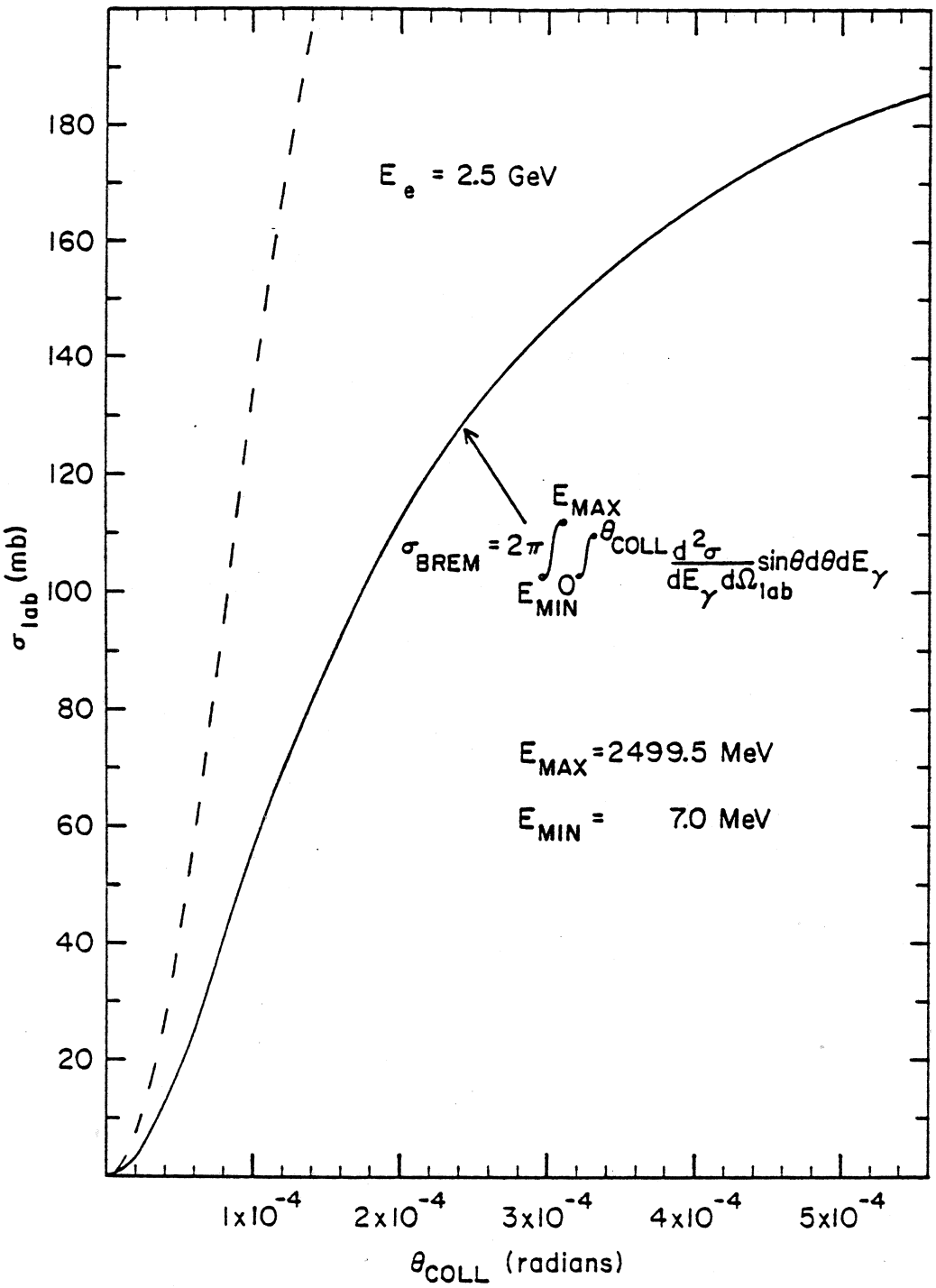

FIG. 30: The total cross section for electron bremsstrahlung in the residual gas of the interaction straight, integrated over a circular collimator of half-angle θ_{COLL}, is shown by the solid line. In contrast, the angular dependence of the laser-backscattered radiation is also shown here as the dashed curve (solid line of Fig. 8).

$$\frac{d\sigma}{d\Omega}(\theta) = \frac{4\alpha}{\pi}\left(\frac{e^2}{mc^2}\right)^2 \beta^2\gamma^2 \quad \frac{(1+\gamma^4\theta^4)}{(1+\gamma^2\theta^2)^4} \qquad (14)$$

$$x \left\{ \ell n^2\left[\frac{4\beta^2\gamma^2 mc^2}{(1+\gamma^2\theta^2)} \quad \frac{1}{E_{\gamma}^{MIN}}\right] - \ell n^2\left[\frac{4\beta^2\gamma^2 mc^2}{(1+\gamma^2\theta^2)} \quad \frac{1}{E_{\gamma}^{MAX}}\right]\right\} .$$

The integration of Eq. (14) over the angular acceptance of the γ-ray beam-defining collimator is shown by the solid line in Fig. 30 for E_{MIN} = 7 MeV, the minimum energy needed to produce a nuclear reaction. (For comparison, the corresponding cross section for laser backscattering--solid line in Fig. 8--is replotted as the dashed line in Fig. 30.) For a collimator half-angle of 4×10^{-4} radians, a total electron current of 0.5 amps, and a vacuum of 1×10^{-10} torr in the 11.3-meter straight section, the expected rate of bremsstrahlung γ rays between 7 MeV and 2499.5 MeV is 1800 s^{-1}. This is completely negligible compared with the 10^7 tagged backscattered rate.

III.7 Comparisons with Other Medium-Energy Photon Sources

The recent review by Beil and Bergere (Be80) discusses most of the available techniques for producing high-energy γ-ray beams. The characteristics of medium-energy beams ($E_\gamma > 200$ MeV) produced by the various possible methods is summarized in TABLE III.

The difference between bremsstrahlung spectra obtained at two electron energies E_1 and E_2 produces a peak in the effective photon spectrum between E_1 -0.5 MeV and E_2 -0.5 MeV. To obtain reliable estimates of the magnitude and shape of this difference spectrum, E_1 and E_2 must be separated by several MeV. Thus, although this technique produces a large effective photon flux, the resolution is poor and the associated nuclear measurements must be sensitive to small differences between two large numbers.

The flux of 3×10^5 sec^{-1} quoted for tagged-e^--bremsstrahlung is available at the Bonn synchrotron, which is currently the only facility in the world where such high-energy moderate-resolution beams are available. This number could in principle be increased to about 10^7 sec^{-1} by utilizing a high duty-factor electron accelerator, if such a machine existed.

Positron annihilation-in-flight has been used extensively to produce photons, chiefly below 100 MeV. When utilizing such a beam, a second measurement must always be made to subtract out the effects of the accompanying bremsstrahlung. At energies above 100 MeV the bremsstrahlung contribution becomes very large, and this subtraction becomes much more difficult (Be80).

The bremsstrahlung background to e^+ annihilation-in-flight can be removed by detecting the second annihilation photon. However,

TABLE III: Sources of Medium-Energy Quasi-Monochromatic Gamma Rays

	Resolution	Polarization	Monochromatic Flux (sec^{-1})	Yield of accompanying γ rays of unknown energy
e^- bremsstrahlung end-point difference	-----	-----	10^{11}	Very large below end-point region
e^- Tagged bremsstrahlung	10 MeV *	-----	3×10^5 *	Large component untagged
e^+ annihilation in flight	3 MeV	-----	$<10^6$	Very large from bremsstrahlung
tagged-two-photon e^+ annihilation in flight	~5 MeV +	-----	$<10^4$ +	Very large component untagged
e^- coherent bremsstrahlung in diamond	60 MeV	~33% ‡	10^6	Large ‡
e^- laser scattering at the NSLS (X-RAY ring)	2.7 MeV	>90%	2×10^7	None

* Parameters quoted are from Bonn (Me79). The flux obtainable with a high-duty factor electron accelerator could be ~10^7, if such a machine existed in this energy range.

\+ Parameters quoted are extrapolated from initial tests at Saclay (Be80).

‡ Higher polarizations and lower backgrounds are available with this technique, but only for very high photon energies-many GeV (Pa68,Ta80).

kinematics and practical considerations necessitate using only those photons emitted at angles away from 0°. This greatly reduces the effective flux, and the resolution degrades because of the dependence of the angular definition upon the electron beam divergence (Be80).

A review of photon production by coherent e^{-}-bremsstrahlung in crystals such as diamond is given in ref. (Pa68). This technique can produce a single 10% resolution polarized γ-ray line, with relatively little background, for energies greater than about 5 GeV. However, below 1 GeV several strong lines are produced, and the resulting spectrum is no longer even quasimonochromatic.

In addition to the parameters listed in TABLE III, the physical size of the photon beam is also an important consideration. Of course, this can always be reduced by collimation, but not without a dramatic cost in intensity. For the conditions necessary to obtain the flux levels quoted in TABLE III, the proposed laser-backscattered beam is by far the smallest. The beams from the proposed facility would certainly be the most versatile.

IV. Medium-Energy Research Program

A representative set of experiments, which illustrates the versatility of the proposed facility in addressing diverse questions in medium-energy research, is outlined within the following subsections. This program is presented in an order that is roughly consistent with the phases of development of the γ ray facility. The motivation for this set of experiments is discussed in the next section. An outline of specific measurements and count rate estimates is given in Section IV.2. The major pieces of equipment necessary for these experiments, most of which already exist at BNL, are listed in Section IV.3.

IV.1 Scientific Motivation

A. Search for Giant-Delta Resonances in $(\vec{\gamma},\gamma)$

One of the most extensively studied collective excitations in nuclear physics is the giant dipole resonance (GDR). In a microscopic picture a large number of particle-hole states, which in the absence of collectivity would produce a distribution spread out over 5 to 10 MeV, coherently add to concentrate their strength in a narrow region a few MeV wide. The GDR has been observed in the low energy ($80A^{-1/3}$ MeV) photoabsorption cross sections of most nuclei. At much higher photon energies, the internal degrees of freedom of the individual nucleons can be excited. High energy absorption cross sections are dominated by the production of the delta, the first nucleon-excited state at $E_x \simeq 300$ MeV. This situation is illustrated in the top of Fig. 31. The integrated absorption strength over the region of the Δ is in fact much larger than in the low energy dipole resonance peak.

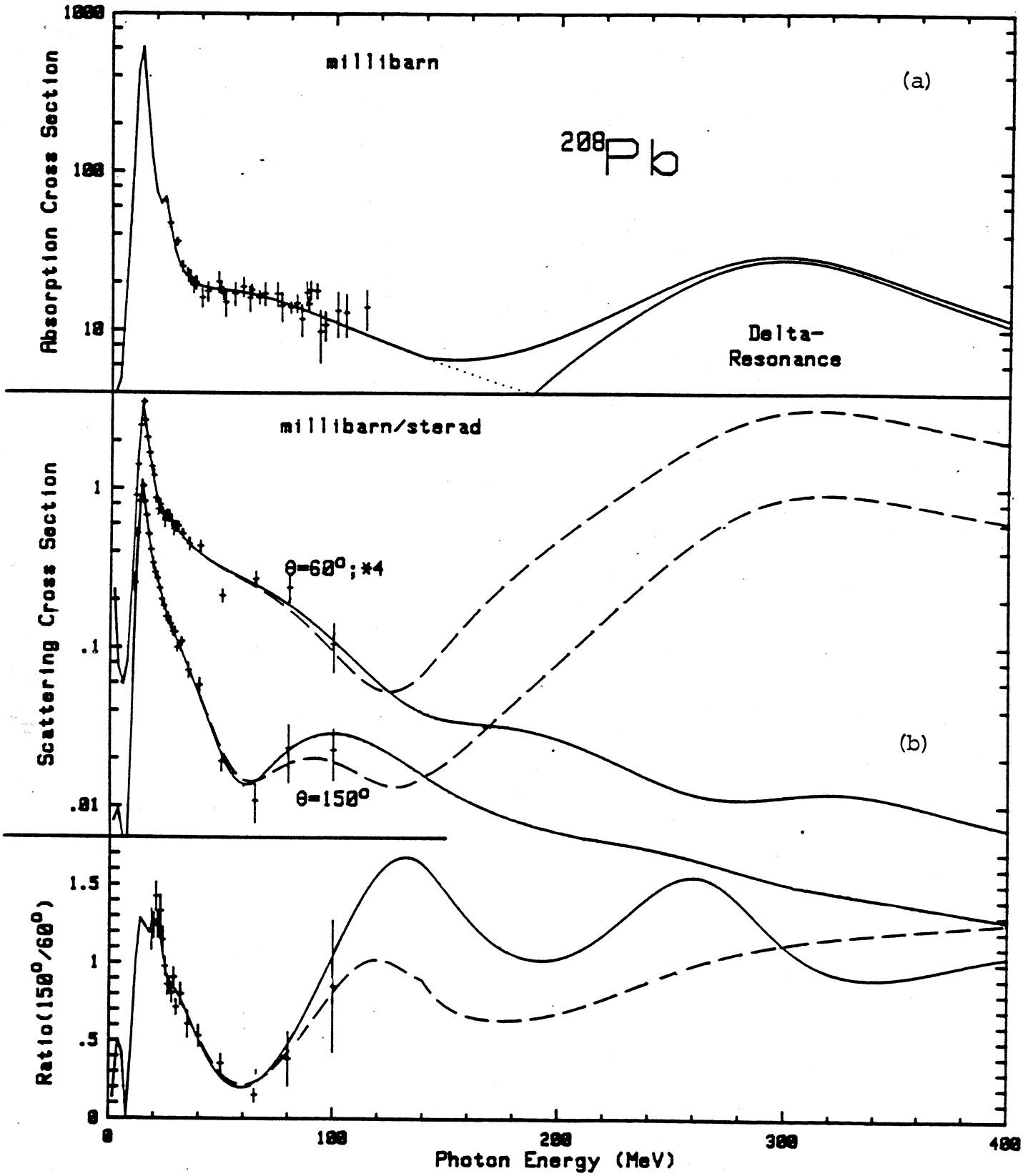

FIG. 31: (a) Photoabsorption for ^{208}Pb, extrapolated up to the region of the delta.

(b) Elastic photon scattering from ^{208}Pb with (dashed) and without (solid) a collective enhancement (Le81).

When a neutron or proton is transformed into a Δ, it leaves behind a nucleon hole and, in direct analogy with the low energy GDR, this suggests the possible existence of highly-collective "giant-delta" resonances made up of a coherent superposition of a large number of Δ-hole states. Recent indirect evidence of such unusual objects has come from (p,n) experiments which have observed spin-flip giant Gamow-Teller (GT) resonances near the GDR in a number of nuclei (see, for example, Ba80). About half of the GT sum rule strength appears to be missing from these measurements. The M1 operator for GT transitions can not only act on a nucleon to change its spin, but can also flip the spin of a quark within a nucleon to make a Δ. The missing GT strength may be contained in a coherent excitation in which the nucleons are excited from the N to the Δ without changing their radial or orbital angular momentum quantum numbers. A calculation for the resulting GT strength distribution in ^{208}Pb is shown in Fig. 32 (from Bo81) where a giant Δ-resonance robs about 60% of the strength from the low-lying GT states. A more detailed calculation including exchange terms suggests that the depletion of the low-lying strength may not be quite this large, only 20 to 30% (Sp82). Nonetheless, a collective enhancement in the region of the Δ is still expected.

The signature of a collective GT-delta resonance is more elusive than that of the GDR. Since the Δ in free decay is 115 MeV wide, a broad peak in the photoabsorption cross section ($\sigma_{\gamma A}$) near the region of the Δ is always expected, and the modifications of this peak due to collectivity will be extremely difficult to disentangle.

The optical theorem and a dispersion relation uniquely determine forward elastic ($\theta_\gamma=0^o$) photon scattering from the total

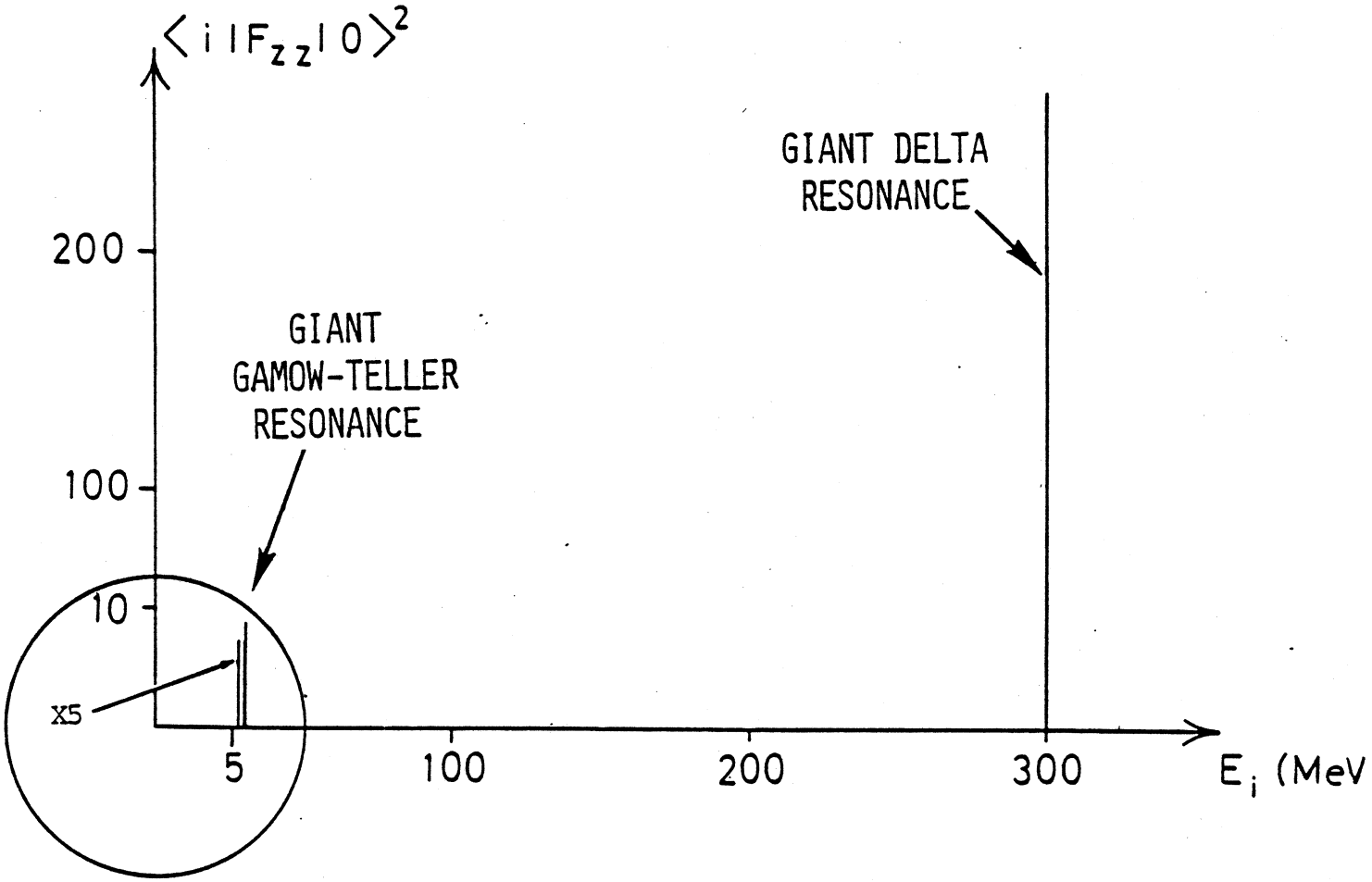

FIG. 32: Calculated spin-flip strength function for ^{208}Pb, from (Bo81).

photoabsorption cross section, providing σ_γ is known at all energies. Such simple constraints do not exist at other angles. The lowest order diagrams contributing to elastic photon scattering from a nucleon are shown in Fig. 33(a). (These diagrams also appear in electron scattering, but only as second-order dispersion corrections.) The contributions to nuclear elastic scattering are shown schematically in Fig. 33(b). The first term contains all of the diagrams from Fig. 33(a), summed over the nuclear constituents. The second term, resulting from internucleon couplings, is formally similar except that the final nucleon that emits the γ ray is different from the one that absorbed it. In the region near E_γ = 300 MeV where the delta resonance dominates, the matrix elements from the first term in Fig. 33(b) have the form

$$M_I \simeq <0 \left| \sum_j \frac{e^{-i(\vec{k}_i-\vec{k}_f)\cdot\vec{r}_j}}{(E_j-E_\Delta)+i\Gamma/2} \right| 0 > . \qquad (15)$$

Since variations in the nucleon energies E_j due to Fermi motion are small compared to the energy and width of the delta, the denominator in Eq. (15) may be taken outside the sum. What remains is essentially the form factor for elastic electron scattering, which will be very small at backward angles.

The contributions of the second term in Fig. 33(b) depend critically on the range of the internucleon correlations. If the correlations are very short range, then this term essentially reduces to the first. On the other hand, if the correlations are long range, as would be expected in a highly collective excitation, then this term will dominate the large angle scattering with a form factor of order unity.

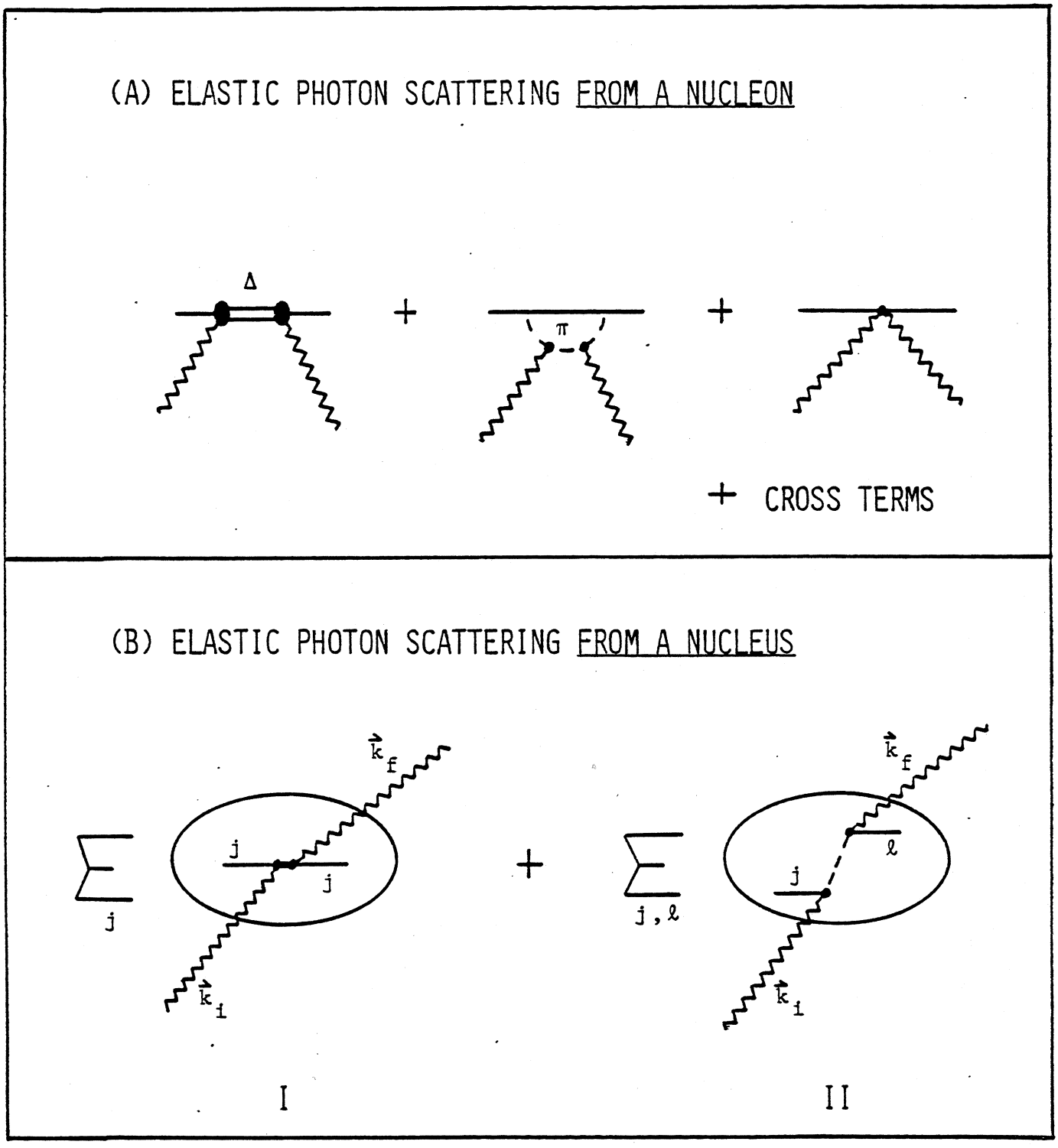
(A) ELASTIC PHOTON SCATTERING FROM A NUCLEON
Δ
π
+ CROSS TERMS
(B) ELASTIC PHOTON SCATTERING FROM A NUCLEUS
$\vec{k}_f$
$\vec{k}_i$
j
j
j
j, ℓ
ℓ
I
II

FIG. 33

The absorption cross section for ^{208}Pb (Le81), shown in Fig. 31(a), has been extrapolated up to the region of the delta using the elementary nucleon cross sections ($82\,\sigma_{\gamma p} + 126\,\sigma_{\gamma n}$). In Fig. 31(b) elastic photon scattering at $\theta_\gamma = 60^\circ$ and 150° is plotted under two extreme conditions. In each of these calculations, σ_γ was used, with the optical theorem and a dispersion relation, to calculate the forward scattering $\frac{d\sigma}{d\Omega}(E_\gamma, \theta_\gamma = 0^\circ)$. This cross section was then multiplied by the dipole angular distribution factor $(1+\cos^2\theta_\gamma)/2$ and by a squared form factor $|F(q)|^2$ to obtain the scattering at θ_γ. In the elastic scattering of photons with energy E_γ, the momentum transfer q is entirely determined by the angle θ_γ:

$$q = \frac{2E_\gamma}{c} \sin(\theta_\gamma/2) \quad . \qquad (16)$$

The solid lines of Fig. 31(b) result from using the charge form factor from electron scattering. These are the results expected for purely one-body interactions. Even at $\theta_\gamma = 60^\circ$, the cross section is so much reduced by the form factor that there is no hint of Δ excitations. The dashed curves are obtained by setting $F(q) = 1$, and result in peaks at large angles. Thus, scattering cross sections, characteristic of highly collective excitations, should exhibit some large angle enhancement. Even when most of the absorption cross section σ_γ arises from single nucleon degrees of freedom, collective enhancements should still manifest themselves in the elastic scattering of photons at large angles (large q) where the one-body contributions are negligible.

It is evident in Fig. 31 that elastic photon scattering is an extremely sensitive method of looking for giant collective delta

resonances. For the two extreme cases shown, the cross sections in the region of the delta differ by two orders of magnitude! In addition, there should be a fairly strong A dependence to this phenomenon since the γ ray can only sample those collective internucleon correlations which extend over a distance that is comparable to the photon wavelength. This distance, λ=4.1 fm for a 300-MeV γ ray, is on the order of the nuclear diameter in s-d shell nuclei, but is significantly smaller than the diameter of heavy nuclei.

For these measurements, low-background, high-resolution beams are required to distinguish the scattered photons from the chief target-related background, namely, high energy gammas from π^o decay which have a maximum energy only ~10% less than the elastic photons. Furthermore, if such a "giant delta" structure were observed, its spin could not be determined without a polarized photon beam. With plane polarized γ rays, the multipole content can be studied through the azimuthal dependence of the scattering at a fixed θ_γ (and hence, fixed q). The gamma ray beams attainable in PHASES I and II will meet the needs of these scattering experiments.

B. Modifications to the $\Delta(1232)$ in Nuclear Matter, Studied through Total Photoabsorption

The first excited state of the nucleon, the J=3/2 T=3/2 $\Delta(1232)$, is well known to have an excitation energy of 300 MeV and a width of 115 MeV, in free space. However, its mass and width are strongly affected when it is introduced into the nuclear medium. To understand how the Δ interacts with nuclear matter is a challenging problem facing medium-energy physics.

Since the Δ decays primarily to a pion plus a nucleon, it is readily excited in π -induced reactions. Fig. 34(A) shows the total cross section for pions on ^{16}O. The solid curve is A times the isospin-averaged elementary cross section for Δ production. The data (CL74) is almost a factor of 3 lower than this estimate. Furthermore, the peak is shifted to lower energies and is substantially broadened. A number of effects are believed to contribute to such alterations of the Δ in nuclei (OS79):

(1) Rescattering, in which the Δ decays into a π (and sometimes a ρ) which then subsequently excites a Δ in another nucleon, tends to lower the peak and broaden its width.

(2) Fermi broadening, due to the momentum distributions of the bound nucleons, mainly increases the width.

(3) Pauli blocking, in which the phase space for the $\Delta \rightarrow \pi + N$ decay is reduced since many of the states available for the nucleon are already occupied, tends to increase the Δ-lifetime and can lead to significant reductions of the peak width and slight shifts to higher energies.

(4) Damping into two-body non-mesonic decay channels ($\Delta N \rightarrow NN$) tends to increase the peak width.

There is a good deal of cancellation between these effects, which makes the study of any one of these mechanisms somewhat problematic. However, calculations of pion-induced reactions indicate that the largest modifications made by the nuclear medium are due to rescattering (OS79,WE81). These calculations are able to obtain a fair representation of the data (dashed lines in Fig. 34(A)).

Photon induced reactions in the region of the Δ seem to present quite a different picture. In Fig. 34(B), charged particle

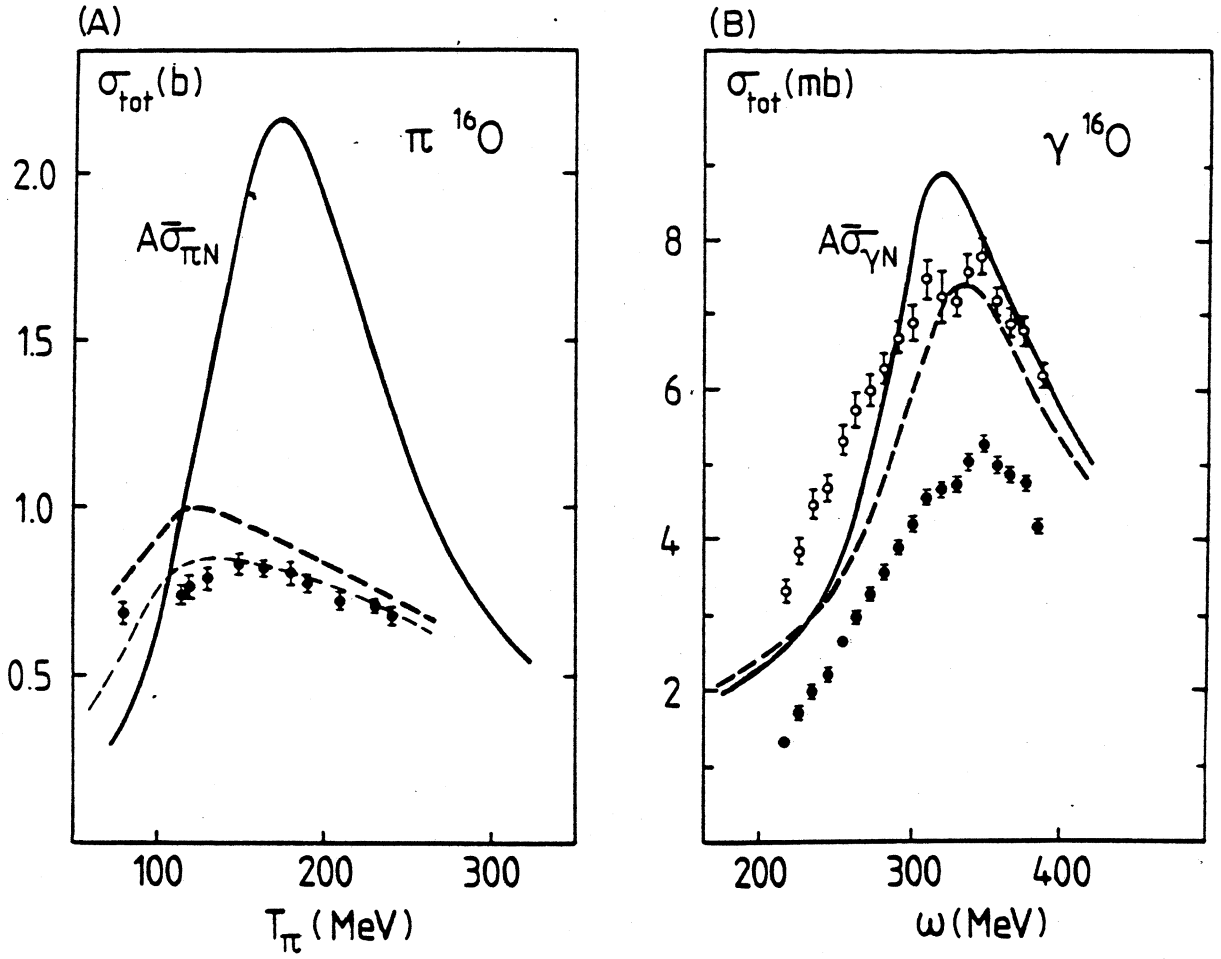

FIG. 34: Comparison of total absorption cross sections for pions (A) and photons (B) on ^{16}O. Solid curves are the scaled nucleon cross sections. Dashed curves are the results of delta-hole model calculations (We81).

photoproduction data from Bonn (ME79), measured over a limited particle energy range (solid points), have been extrapolated to estimate the total γ-absorption cross section (open circles). There appears to be little reduction in the cross section from the $A\sigma(\gamma N)$ estimate. This phenomenon is roughly explained by the fact that the pion interacts primarily with the nuclear surface, causing the $\sigma_{\pi A}$ cross section to increase with $A^{2/3}$ and approach $\pi(R+\lambda\!\!\!^{-})^2$, while the weakly interacting photon samples the entire nuclear volume, causing the $\sigma_{\gamma A}$ cross section to approach $A\sigma(\gamma N)$. This simple picture may be adequate for light nuclei, but must break down when the nuclear radius becomes substantiallly larger than the Δ and π mean free paths. A deeper understanding of this effect is sought in the Δ-hole model (Hi77,K079,OS81,Sa81). Here the pion or photon converts a nucleon below the Fermi level into a Δ, thereby creating a Δ-hole state $|(\Delta h)J^{\pi},T=1\rangle$, which then propagates through the nucleus. All of the Δ-modifying effects discussed above are contained in the transition operators describing the propagation of Δ-hole states. The rescattering mechanism which dominated the calculations of $\sigma_{\pi A}$ appears to be almost negligible in $\sigma_{\gamma A}$, at least in light nuclei. The main contributions to the calculation of Fig. 34(B) (dashed line) come from Pauli blocking and from damping into non-mesonic channels. Both effects are individually large, but the absorptive broadening overcompensates the Pauli narrowing. Whether or not these effects continue to play a dominant role in photoabsorption on heavier nuclei is an open question since there is no data in the region of the Δ for nuclei heavier than ^{16}O. Even for ^{16}O the Δ-hole model does not seems to reproduce all of the data in Fig. 34(B). Non-resonant amplitudes and quasi-deuteron disintegration must be added to raise the level of

the calculation in the region between 200 and 300 MeV (WE81). On the other hand, there are large uncertainties involved in the extrapolation from the limited data (solid points) to the open circles.

Two other methods have been used to obtain total photoabsorption cross sections. One is to directly measure the fraction of γ rays removed from the beam due to the presence of the target. Here, measurements with and without a target must be sensitive to small differences between two very large numbers. A calculated atomic absorption is usually subtracted from this total absorption to obtain the photonuclear cross section. This method has been used extensively at Mainz to study the region of the giant dipole resonance in light nuclei ($A \leq 40$). However, a recent measurement of ^{16}O absorption near the Δ using this technique has yielded cross sections that are 60% lower than those of Fig. 34(B) near the peak at $E_\gamma \simeq 320$ MeV (Sc82). This discrepancy has yet to be resolved. The other experimental technique used to determine $\sigma_{\gamma A}$ is to measure all the neutrons produced by reactions and correct for detector efficiencies and neutron multiplicities (Le81). These corrections are quite complicated, and this technique has never been applied in the region of the delta. This method has been developed recently at Saclay (Ca82) and the resulting photoabsorption cross sections, all below pion threshold, exhibit strong energy dependent discrepancies when compared to the Mainz data (Ah75). Furthermore, these differences persist even when the cross sections are corrected for purely charged-particle producing photoreactions (Be82). The Saclay results have been compared to the Bonn data at only one energy, $E_\gamma = 140$ MeV, and agree quite well there (Ca82). The Saclay results suggest

that the Mainz data is too high, while other data from Mainz suggest that the Bonn measurements are too high. There does not seem to be a way of making these 3 sets of measurements consistent.

In summary, a better theoretical understanding of the Δ in nuclear matter desperately requires reliable experimental cross sections over a range of nuclei. Only data on light nuclei is currently available, and these are in a thoroughly confused state. The γ-ray beams from the NSLS will provide a unique new method of measuring photoabsorption cross sections. All photons reaching the target will either be tagged or rejected. Thus, an absorption measurement consists of simply counting those tagged γ rays that did not survive passage through the target. Furthermore, the small size of the proposed γ ray beam will permit a shower, originating at the target, to be distinguished from a γ ray that passed through the target without interaction. Atomic absorption can thus be rejected electronically, yielding a direct measurement of the nuclear photoabsorption. The detector planned for these experiments is described in APPENDIX A. These photoabsorption measurements can be started in the very early stages of the program.

In addition to the four Δ-modifying effects discussed above, the absorption cross sections near and above the delta are also affected by the asymptotic properties of $\sigma_{\gamma A}$, because of the existence of sum rules. Microscopically, this sensitivity arises from meson-exchange effects and hadronic shadowing (We73). In particular, below meson threshold, the Gell-Mann, Goldberger, Thirring (GGT) sum rule gives the total cross section as (Ge54)

$$\int_0^{th_\pi} \sigma_{\gamma A}\, dE = S\,\frac{NZ}{A}\,(1+K), \qquad (17.1)$$

where

$$K = \left(S\,\frac{NZ}{A}\right)^{-1} \int_{th_\pi}^{\infty} \left[A\sigma_{\gamma N} - \sigma_{\gamma A}\right] dE, \qquad (17.2)$$

and $S \simeq 60$ MeV-mb. The difference between the incoherently summed absorption by A free nucleons compared to the absorption by a nucleus composed of the same A particles [the enhancement parameter K of Eq. (17)] arises mainly from the exchange of charged mesons. (A generalized version of this is presented in ref. We73.) Slight modifications of the asymptotic behavior of $\sigma_{\gamma A}$ can result in sizeable changes in K.

From the very limited amount of high-energy absorption data that is currently available (Zi79), there appears to be an "experimental high-energy sum-rule" that connects the region of the delta to the classical sum rule S:

$$\int_{th_\pi}^{E_{MAX}} \left[A\sigma_{\gamma N} - \sigma_{\gamma A}\right] dE \simeq S \quad . \qquad (18)$$

In the approximation that $E_{MAX} \simeq \infty$, Eqs. (17.2) and (18) imply that $K = A/NZ$. Thus, for ^{7}Li and ^{9}Be where Eq. (18) has been verified for $E_{MAX} = 335$ MeV, the enhancement factors K would be 0.58 and 0.45,

respectively. These values are in excellent agreeement with those obtained from absorption data below pion threshold (Ah75) using Eq. (17.1). This agreement relies on the rapid approach to zero of the difference cross section in Eq. (18) above 335 MeV, although the data (Zi79) do not indicate such a rapid approach to the asymptotic free-nucleon limit. Therefore, absorption data above 350 MeV is badly needed to investigate this problem. Data on heavier targets above pion threshold would also be illuminating since K, determined from measurements below threshold, increases with A (to about 1.2 at ^{40}Ca) while the value implied by Eq. (18) [A/NZ] decreases rapidly (to 0.1 at ^{40}Ca). The extension of the absorption measurements to energies above 350 MeV and to heavier nuclei is planned for PHASE III of the project.

C. Tests of the Delta-Hole Model in $(\vec{\gamma},\pi^o)$

Compared with the inclusive photoabsorption measurements, studies of specific decay channels can provide even more stringent tests of theory. Of all photoproduction reactions, <u>coherent</u> π^o production is by far the most strongly affected by the Δ. Here the whole nucleus takes up the recoil momentum of the Δ and the resulting π^o decay leaves the nucleus in its ground state. The diagrams contributing to the elementary π-production amplitudes are shown in Fig. 35 (We81). Charged pion photoproduction - Fig. 35(A) - has background components which are comparable in size to, and interfere with, the Δ-resonant M1 amplitude. In contrast, the coherent (γ,π^o) process of Fig. 35(B) is almost completely dominated by the M1 excitation of the Δ. This simplicity makes this reaction a particularly suitable tool for studying the Δ in nuclei.

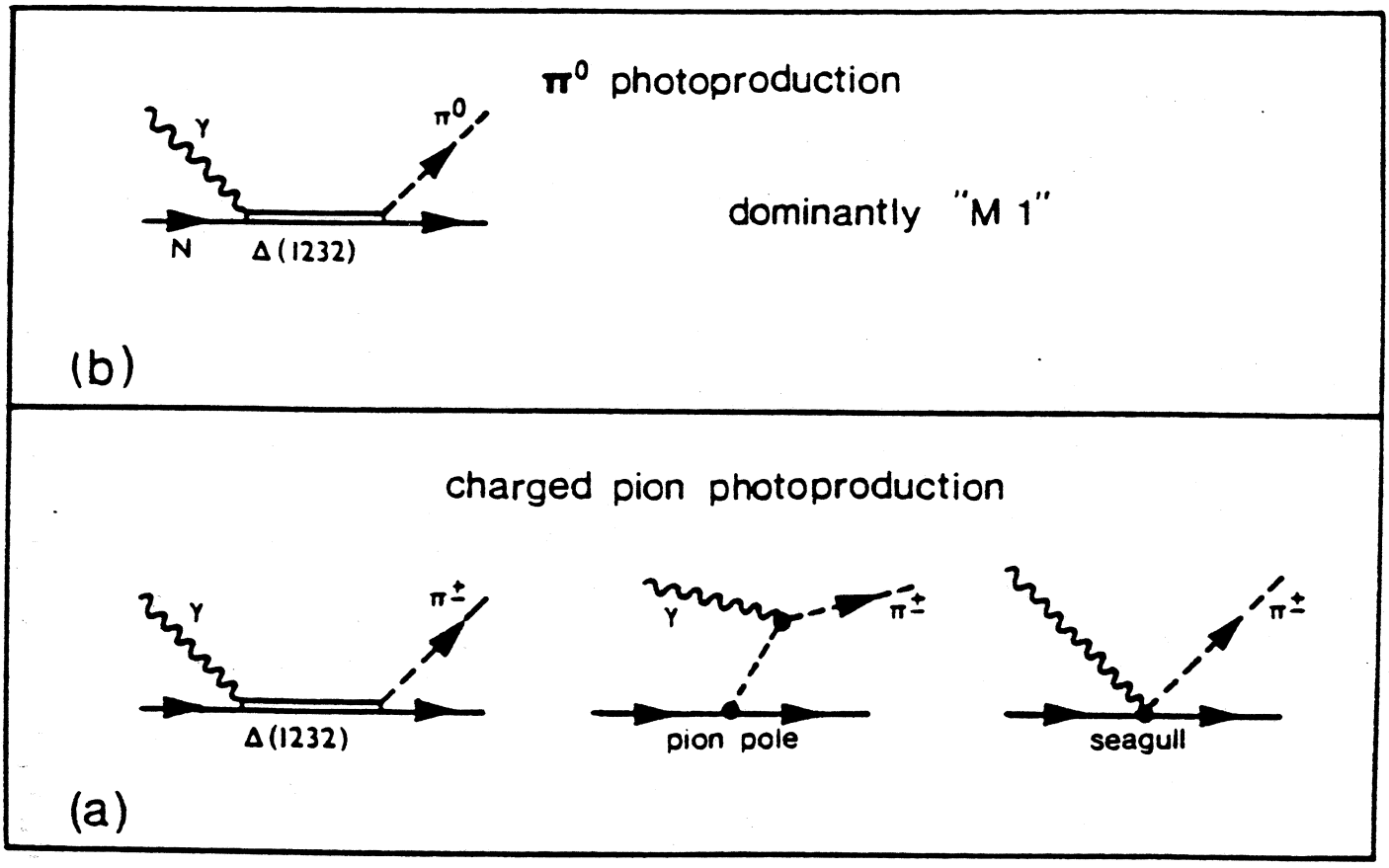

FIG. 35: Elementary pion-photoproduction amplitudes (We81).

Several estimates for the coherent (γ,π^o) reaction on light nuclei have recently appeared in the literature. The sensitivity of this reaction to the details of the Δ-hole model is evidenced by a large spread in cross sections predicted by different authors, despite the fact that each calculation is capable of producing satisfactory agreement with pion scattering data. The calculation of Saharia and Woloshyn (Sa81) for $^{16}O(\gamma,\pi^o)$ is shown in Fig. 36 (solid lines) together with a DWIA estimate (dashed lines). The calculations of Koch and Moniz (Ko79) and of Oset and Weise (Os81) both predict cross sections a factor of 2 lower than those shown here. The datum at E_γ=294 MeV is from the Bonn group (Me79). (There is only one other datum available for this reaction: $d\sigma/d\Omega$ = 74±5 μb/sr at E_γ=330 MeV for $0^o \leq \theta_{\pi^o} \leq 10^o$, again from the Bonn group (Me79),) Although there is an apparent agreement in Fig. 36, it should be noted that these Bonn measurements were done with bremsstrahlung under the assumption that all observed π^o's left the nucleus in its ground state. It is difficult to estimate the errors associated with this procedure. In any case, measurements at larger angles would certainly be a much more sensitive test of theory.

There is a larger body of data on the $^{12}C(\gamma,\pi^o)$ reaction. Unfortunately, this proves to be more confusing than illuminating. Until recently, the only data available was from a bremsstrahlung measurement by Davidson (Da59) at $\overline{E}_\gamma$=242 MeV. These data are shown in Fig. 37 along with a number of calculations. (The data points have been renormalized to the latest value of the $\gamma p \rightarrow \pi^o p$ cross section. This reaction had been used to measure the efficiency of the π^o detectors - Da59.) It is clear that the Δ-hole model calculations have become refined with time and have risen to meet the data, although the

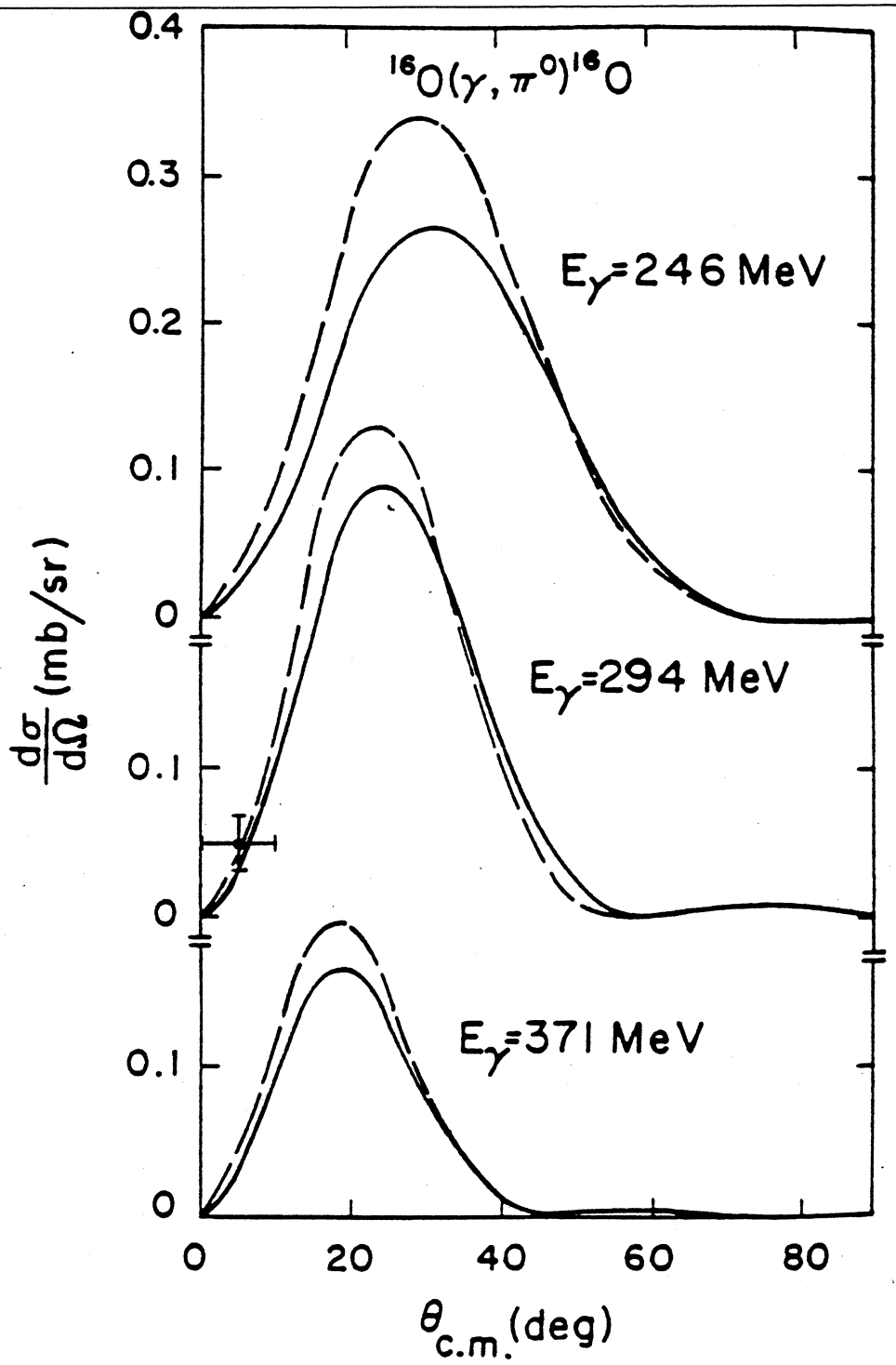

FIG. 36: Delta-hole model calculations for coherent π^0-photoproduction from ^{16}O (Sa81). The data point at E_γ=294 MeV, $0^o \leq \theta \leq 10^o$ is from (Me79).

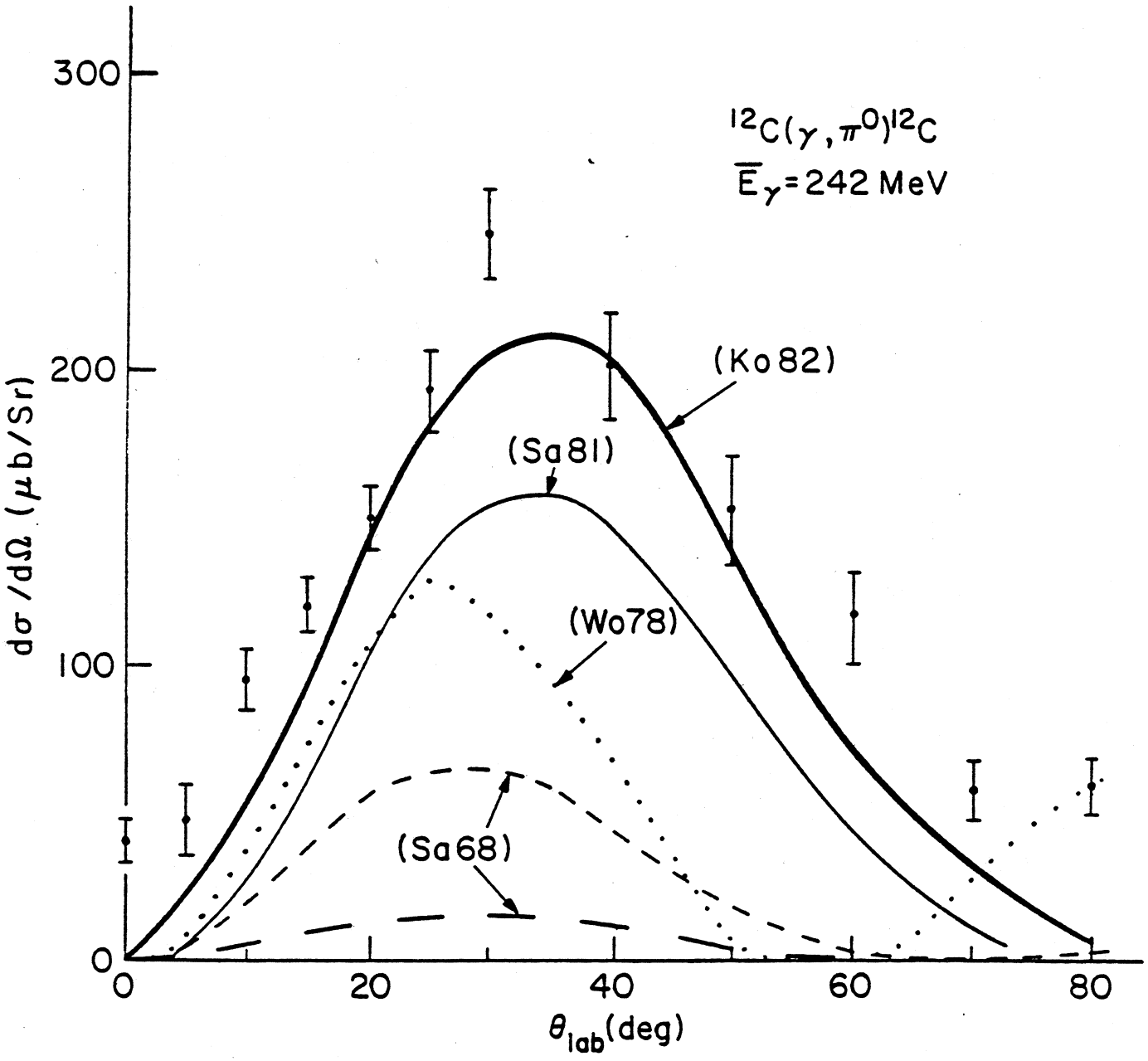

FIG. 37: The bremsstrahlung data of Davidson (Da59) for π^0-photoproduction from ^{12}C, and various delta-hole model calculations.

two most recent works, Sa81 and KO82, still show a sizeable discrepancy. Unfortunately, recent data has fallen far below these two calculations. Preliminary experiments with tagged bremsstrahlung at Bonn (RO80) report a substantial cross section for π^o decays leaving the ^{12}C nucleus in excited states. Direct bremsstrahlung measurements have great difficulty distinguishing this component. Figure 38 shows the recent Bonn measurements for coherent $^{12}C(\gamma,\pi^o)^{12}C$. Although the statistics are poor, these data points are about a factor of 2 below the latest calculation (solid line). The situation is further confused by a new measurement from a Boston University-MIT collaboration using bremsstrahlung from the Bates linac (Mi82). A preliminary analysis of this new data is basically in agreement with the data of Fig. 37. Although no attempt could be made to separate ^{12}C-ground and -excited final states, their total (γ,π^o) cross section is still 30% higher than the sum of the coherent and incoherent components measured at Bonn. A recent reanalysis of the Bonn data has led to a significant increase in the error bars of Fig. 38, owing to uncertainties in the separation of the coherent component with poor photon resolution (Ar82). Nonetheless, the total $^{12}C(\gamma,\pi^o)$ cross section still remains 30% below the more recent Bates measurement.

From the above discussion, it is clear that high quality (low-background, high-resolution, moderate statistics) measurements of the $^{16}O(\gamma,\pi^o)$ and $^{12}C(\gamma,\pi^o)$ reactions, with monochromatic photon beams (so that the coherent part of the cross section can be unambiguously extracted) would significantly advance the understanding of Δ-hole interactions in nuclear matter. Measurements of this type with direct bremsstrahlung are extremely problematic. A π^o of a particular energy

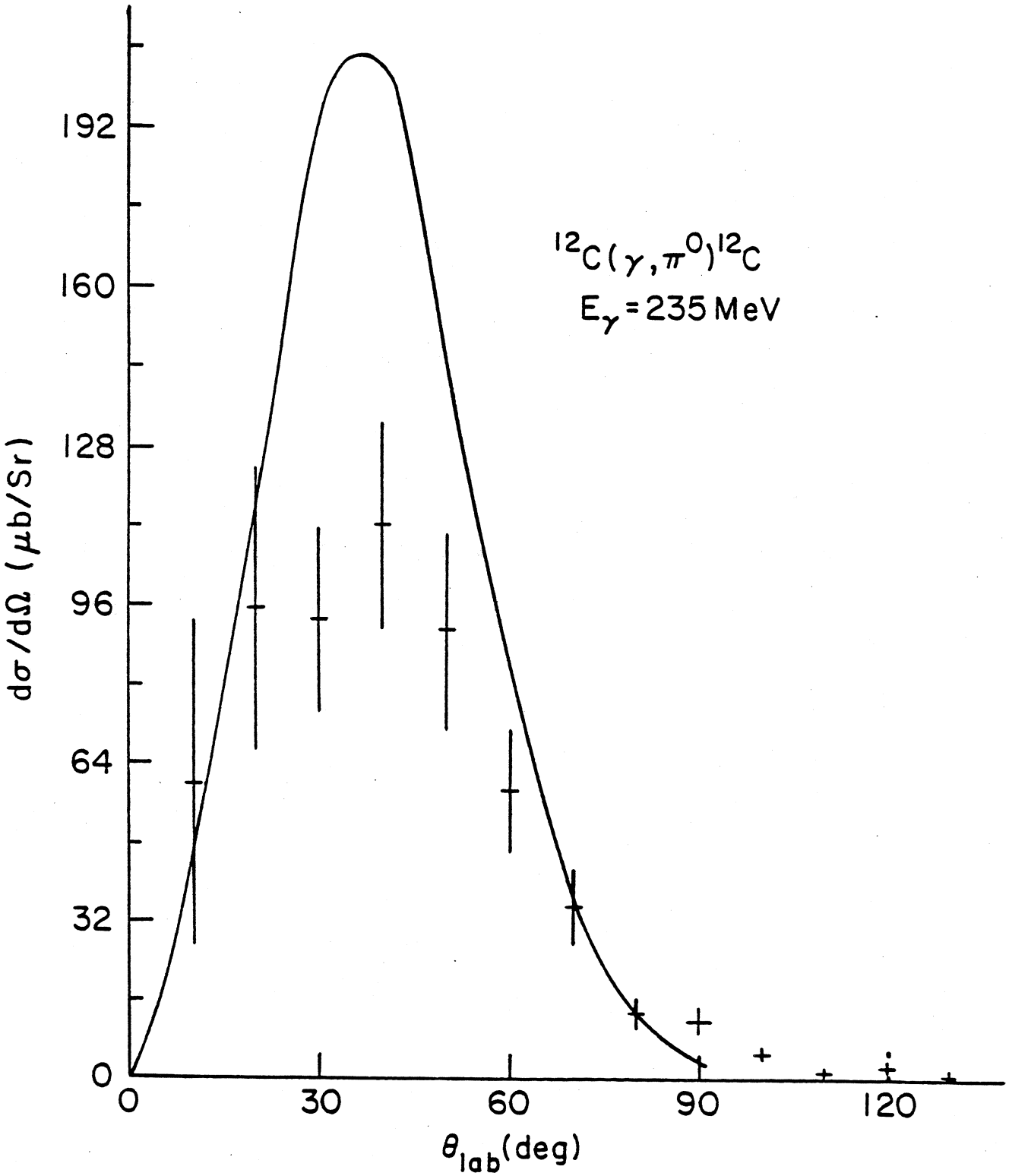

FIG. 38: Tagged-bremsstrahlung data for coherent π^0-photoproduction from ^{12}C (Ro80). The solid curve is a delta-hole model calculation (Mo82).

is detected by its decay into two γ-rays of variable energy and opening angle - see Appendix C. This in itself would not be a problem if coherent productionwere the only open channel. Since this is never the case, the continuous bremsstrahlung spectrum makes separation of the coherent cross section virtually impossible. Good energy resolution in the photon beam is extremely important.

There is another as yet unutilized approach to studying the interaction of the Δ with the nuclear medium. The coupling of the γ-ray to the nucleon that gets excited to make a Δ is entirely M1 relative to the nucleon coordinates. Relative to the nuclear coordinates, several multipoles contribute, all magnetic due to parity conservation. However, added to this "geometric" source of non-M1 strength is a contribution from the Δ-hole residual interaction which is strongly L dependent. This Δ-hole interaction shifts the energies where the contributions from different L's peak. For example, the $L^{\pi} = 1^{+}$ and 4^{-} matrix elements of the Δ-hole force used by Koch and Moniz (Ko79) peak at energies separated by more than 60 MeV. The partial cross sections from a calculation of coherent π^{o} photoproduction on ^{12}C (Hu80) are shown in Fig. 39. An experimental determination of the cross section in the different multipoles would obtain direct information on the strength of the Δ-hole force. At most energies in Fig. 39 significant contributions to the (γ,π^{o}) cross section come from three multipoles (even more at high energies), and π^{o} angular distributions produced by unpolarized photons cannot uniquely disentangle these components. The γ-ray beams from the NSLS will be polarized, and our planned measurements of the coherent $^{16}O(\vec{\gamma},\pi^{o})$ and $^{12}C(\vec{\gamma},\pi^{o})$ reactions during PHASE II operation will provide the first opportunity to compare an experimental multipole decomposition with Δ-hole model calculations.

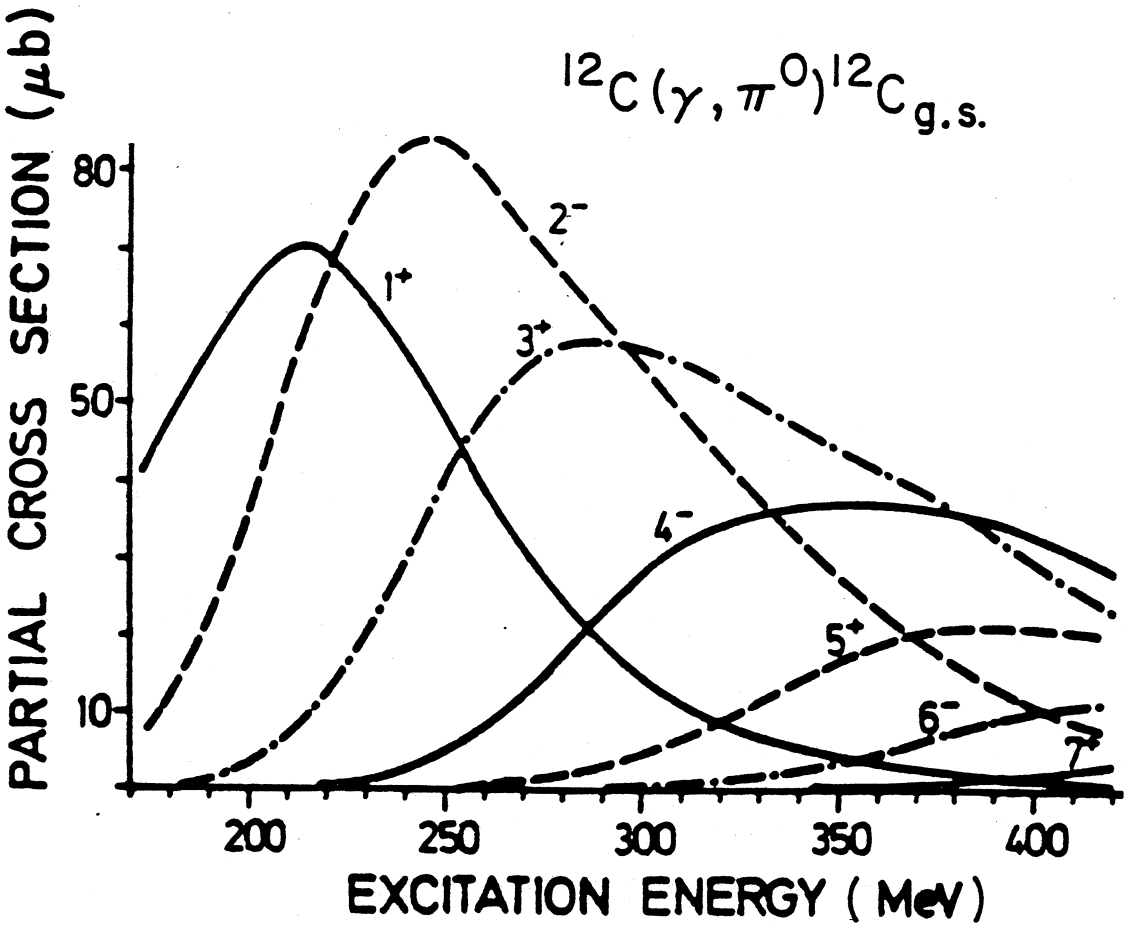

FIG. 39: Angular-momentum decomposition of the coherent π^0-photoproduction cross section from ^{12}C (Hu80).

D. Search for Nuclear Critical Opalescence in $(\vec{\gamma},\pi^+)$

There has recently been considerable speculation about the possible occurence at normal nuclear densities of enhancements in the virtual pion field which are precursors to pion condensation. (A recent review is given in ref. De81; see also Ba81, Ku82, and Gi82.) The enhancements arise from the pion self energy and are expected to occur at momentum transfers of 2 to 3 times the pion rest mass. The experimental searches for this phenomena have been inconclusive at best. It has been suggested (De81) that charged-pion photoproduction could provide a much more sensitive method of searching for this opalescence effect. Recent calculations of the $^{12}C(\gamma,\pi^+)^{12}B$ differential cross sections are shown in Fig. 40 for 210 MeV and 280 MeV incident photons (De81). Near 90^o the opalescence is expected to enhance the cross section by more than an order of magnitude.

The enhancements in Fig. 40 enter the calculation through the pion-pole amplitude of Fig. 35. However, the seagull and Δ-production diagrams are also present and can interfere with the amplitude of interest. An important additional advantage can be gained here by using linearly polarized photon beams. The contribution of the seagull graph is drastically reduced at angles perpendicular to the polarization vector of the incident γ ray. Thus, with this polarization aligned along x, $(\vec{\gamma},\pi^+)$ angular distributions in the <y-z> plane contain contributions only from the Δ and pion-pole terms, and the Δ amplitude can be isolated by measuring the $(\vec{\gamma},\pi^o)$ cross section. The calculations shown in Fig. 40 assume unpolarized photons and neglect Coulomb distortions in the exit channel. Although more recent calculations with distorted waves suggest enhancements that are smaller than those of Fig. 40 (Sc82), the use of polarized photons should substantially improve the signal for an opalescence effect.

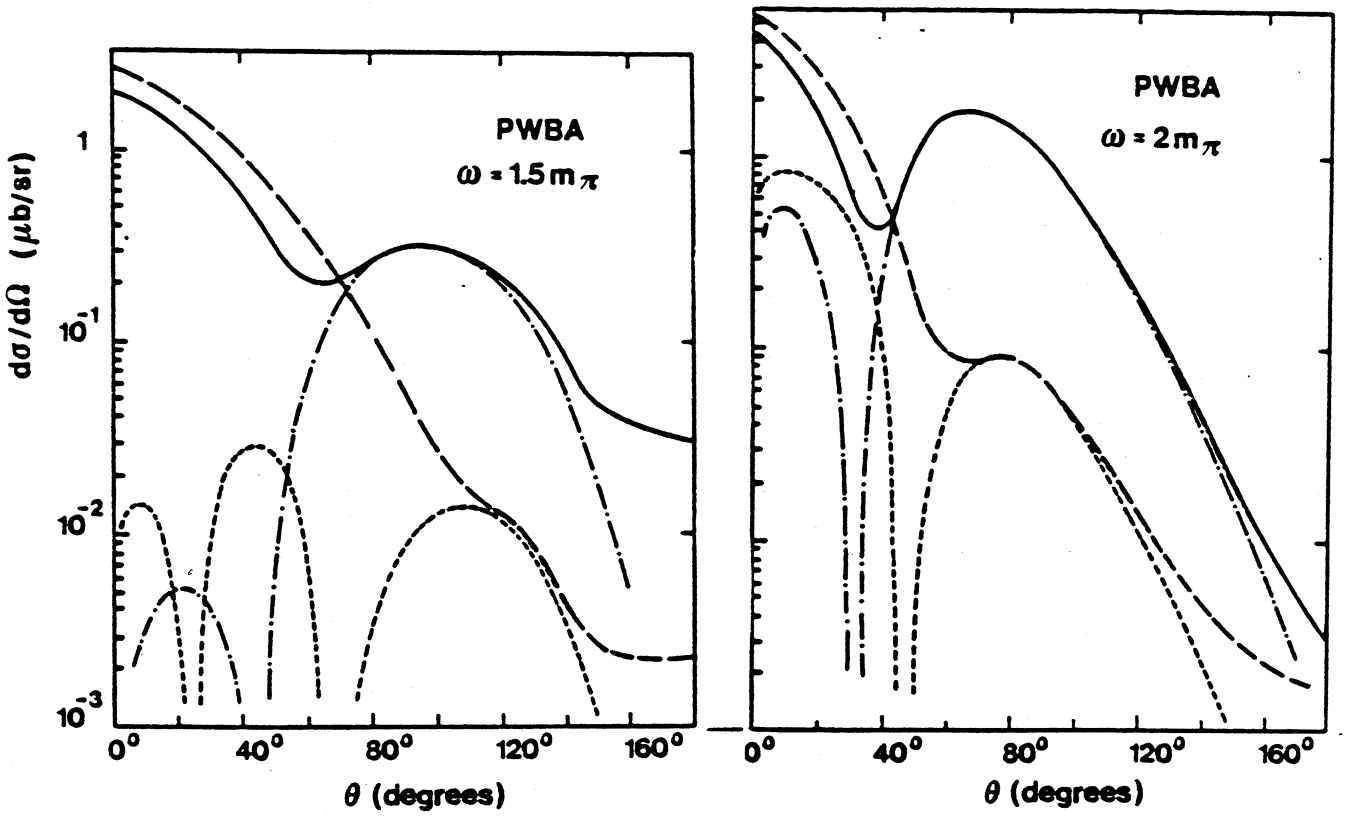

FIG. 40: The angular distribution for the reaction $^{12}C(\gamma,\pi^+)^{12}B$ (g.s.) at pion energies of 70 MeV (left) and 140 MeV (right). The opalescent behaviour is displayed by the full curves whereas the long-dashed curves represent standard 1p shell calculation. The longitudinal spin contributions have been separated as the dot-dashed and short dashed curves. (De81)

These experiments are planned for PHASE II of the project. If an enhancement in the 90° cross section is observed, additional ($\vec{\gamma}$,π^o) measurements can be undertaken to separate out the effects of the delta.

E. Delbrück Scattering from the Vacuum Polarization Cloud

In addition to nuclear scattering, there are three other processes that add coherently to elastic photon scattering: Rayleigh scattering from the atomic electron cloud, Thomson scattering from the charge of the nucleus, and Delbruck scattering from virtual electron-positron pairs created in the nuclear Coulomb field. All three decrease rapidly with scattering angle and only Thomson scattering survives at high energies. For medium energies and large angles, all of these processes are either negligible or can be reliably calculated. However, at high energies and forward angles, Delbruck scattering in fact dominates.

The diagrams contributing to Delbruck scattering are shown in Fig. 41. They essentially represent scattering from the vacuum polarization cloud associated with the charged nucleus. The Delbruck amplitudes are third order in α. Although rather difficult to calculate, they form a unique set of high order Feynman diagrams that can be experimentally isolated and compared with QED. Although QED calculations have successfully reproduced large-angle low-energy data (Ba77), the Delbruck amplitudes are very forward peaked and, at these forward angles, systematic differences between data and calculations still persist (Pa75). There has been only one measurement of small-angle Delbruck scattering at medium energies, $E_\gamma \approx 87$ MeV

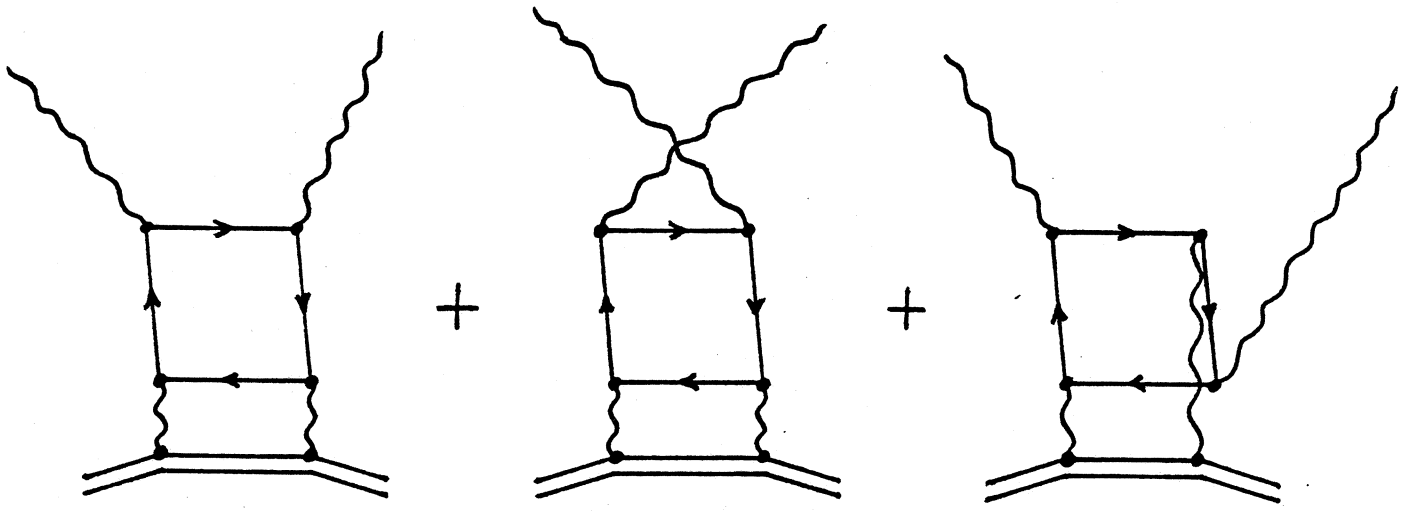

FIG. 41 Diagrams for Delbrück scattering.

(Mo60), and although the data confirmed the expected Z^4 dependence of the scattering from a wide range of nuclei, calculated cross sections have fallen consistently short of the measured values (Pa75).

One of the key experimental problems in detecting Delbrück scattering is the separation of this effect from other amplitudes, particularly Rayleigh scattering which can be significant at small angles. However, the Delbrück amplitudes are very sensitive to the polarization of the incoming photon. The angular dependence of the cross section in planes parallel and perpendicular to the incident polarization vector can be used to study these amplitudes. The beams available in PHASE II will be extremely well defined, as well as polarized, and this will permit sensitive measurements of Delbrück scattering at very small angles over a wide range of energies.

F. The Effects of Neutral Z_o Exchange in $(\vec{\gamma},e^+e^-)$

The structure of the weak-neutral-current interaction has remained an important problem since its discovery in 1973 (Ce73). Since then, only a small number of experiments have reported effects due to neutral currents. The Weinberg-Salam-Glashow (WSG) model, encompassing both weak and electromagnetic forces, has successfully accounted for anti-neutrino-induced reactions (Ba78) as well as parity-violating asymmetries in polarized electron-deuteron scattering (Pr78). However, measurements of parity-non-conservation in the interaction of atomic electrons with nucleons in bismuth vapor (Bai77,Le77) have observed effects much smaller than predicted by the WSG model, although such large discrepancies were not observed in atomic Thallium (Co79). New measurements of the magnitude of these parity-non-conserving effects would greatly help to resolve the nature

of weak-neutral-current interactions. To this end there is currently a large effort to measure forward-backward asymmetries in the production of lepton pairs at PETRA and PEP. The WSG theory predicts asymmetries of $(N^{\mu^+}-N^{\mu^-})/(N^{\mu^+}+N^{\mu^-}) = -(8.7\pm.6)\%$ in the $e^+e^- \rightarrow \mu^+\mu^-$ reaction at 35 GeV. The JADE, TASSO, and MARK-J groups have recently reported asymmetries of $-(12.8\pm3.8)\%$, $-(16.1\pm3.2)\%$, and $-(9.8\pm2.3)\%$, respectively (Ja82, Ta82, Ma82). These asymmetries seem to be consistently higher than the WSG estimate, although much more data is necessary since all of these measurements suffer from poor statistics.

Several authors have suggested electron-bremsstrahlung as a mechanism sensitive to neutral currents (Ja76, El80). The elementary diagrams for this process are shown in Fig. 42(a). The interference of single photon- and Z_o-exchange produces a small component to the emitted radiation that is circularly polarized. In the absence of Z_o-exchange, 0^o bremsstrahlung is completely unpolarized and off-axis it is plane polarized. The circular polarization created by the neutral currents is expected to decrease roughly with the square of the momentum transferred to the nucleus. In a recent experiment at Mainz, Ziegler (Zi82) has measured the component of circular polarization in the $\theta_\gamma<1$ mrad bremsstrahlung of up to 400 MeV electrons, by using a Compton polarimeter as an absorption detector. The observed transmission asymmetry, which is related to difference between right (R) and left (L) circularly polarized components $(d\sigma_R - d\sigma_L)/(d\sigma_R + d\sigma_L)$, is shown in Fig. 43. The polarimeter used in these measurements relied on the spin dependence of Compton scattering, which is a very small part of the total absorption cross section at these high energies. The polarimeter efficiency was thus quite low. The asymmetry of 10^{-6} observed at $E_e \approx 300$ MeV (Fig. 43)

FIG. 42

(A) DIAGRAMS FOR BREMSSTRAHLUNG :

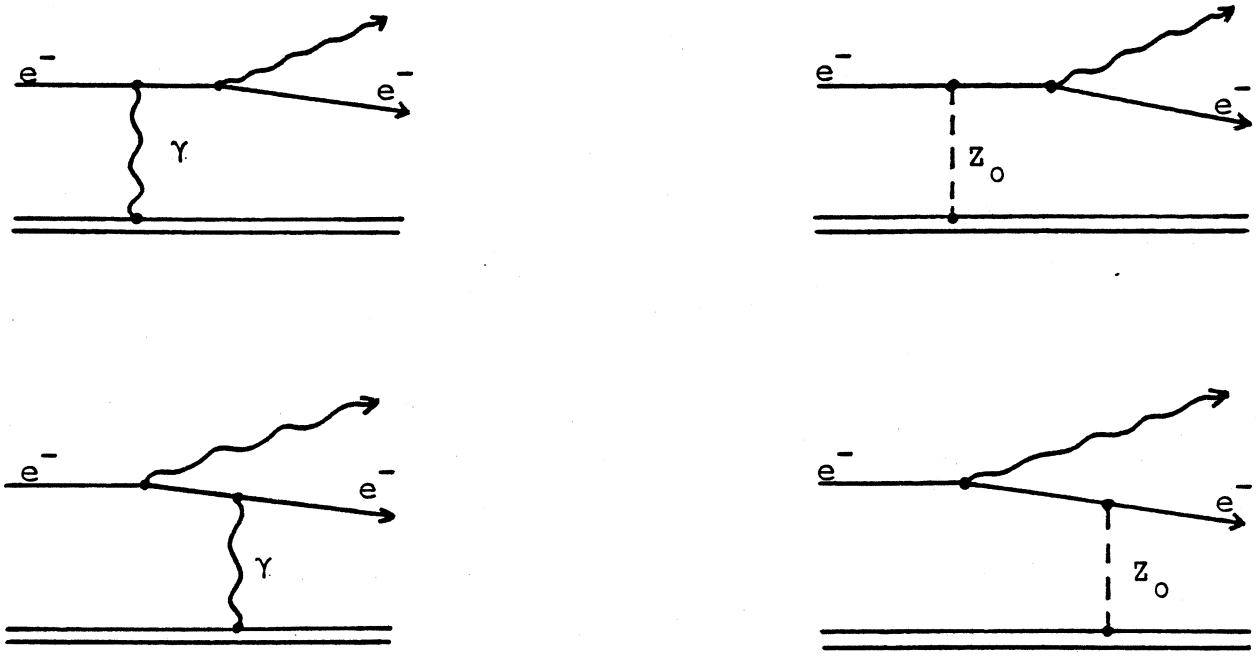

(B) DIAGRAMS FOR PAIR-PRODUCTION :

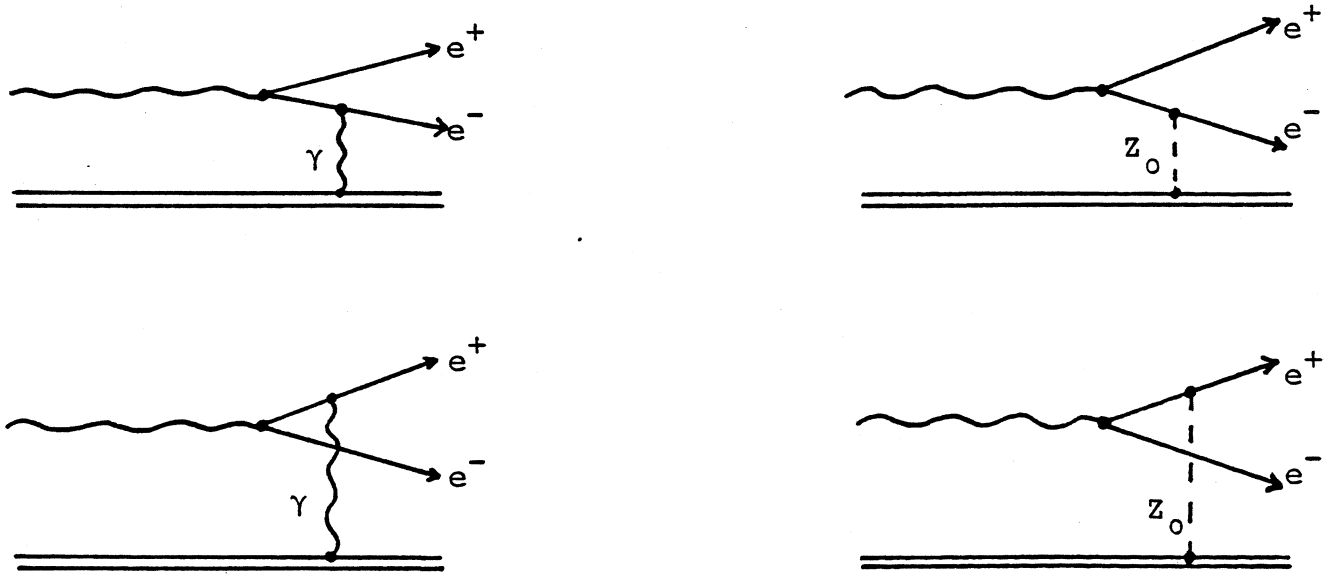

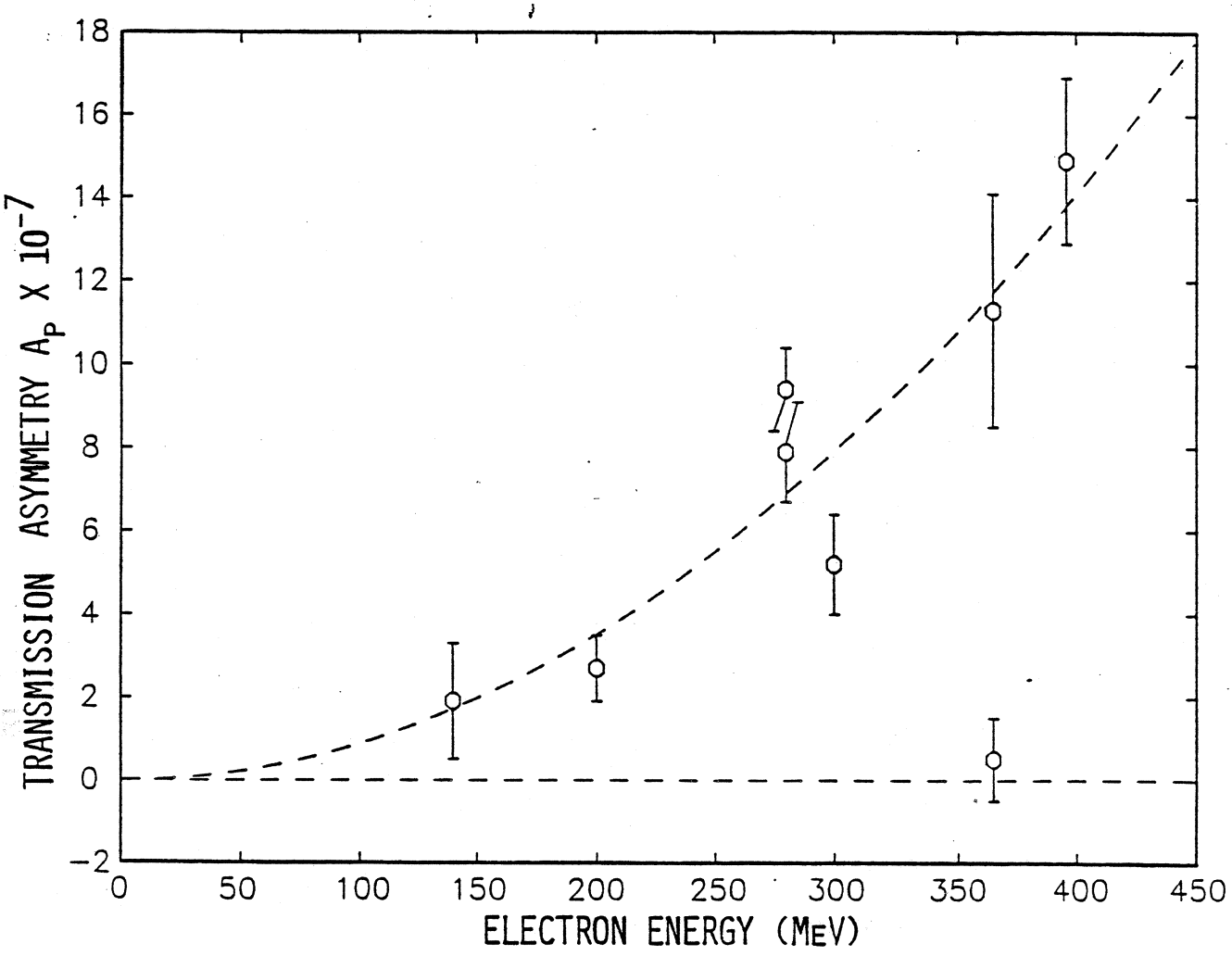

FIG. 43: The asymmetry in the transmission of bremsstrahlung through a magnetized iron absorber used as a Compton polarimeter (Zi82).

corresponds to a circular polarization of 3×10^{-4}. This is two orders of magnitude larger than would be expected from the Weinberg-Salam-Glashow model (Ja76,Zi82). Furthermore, the q^2-dependence evident in the dashed curve of Fig. 43 is the inverse of the WSG prediction: the polarization appears to increase with energy rather than decrease. Ziegler's result, if due to neutral currents, is quite startling. On the other hand, the low datum at 365 MeV suggests the possibility that errors in this experiment may have been underestimated. In any case, this effect must be studied further.

An independent yet related mechanism for studying effects such as evident in Fig. 43, is pair production by circularly polarized γ rays. The relevant diagrams for this process are shown in Fig. 42(b) and differ from those of bremsstrahlung only in the direction of the electron. Although the pair production asymmetry $A=(d\sigma_R - d\sigma_L)/(d\sigma_R + d\sigma_L)$ expected from the WSG model has yet to be calculated for photon energies in the 300 MeV range, an extrapolation of the work of Olsen, et al. (0180) suggests values less than 10^{-5}. Purely electromagnetic effects can also give rise to asymmetries, but these have very different angular and energy dependences (0180).

The effects of neutral currents in pair production can be studied in PHASES I and II with the pair spectrometer that forms part of the absorption detector described in APPENDIX A. The addition of a quarter-wave plate to the laser optical transport will produce 100% circularly polarized 300 MeV γ rays of either helicity. If Ziegler's enhancement over the WSG estimate is indeed due to neutral currents, the effect upon the pair-production asymmetry should be quite dramatic.

G. Search for Dibaryon Resonances in $^2H(\vec{\gamma}, p\,\pi^{\pm})$

There have been several experimental searches for the 6-quark "Dibaryon" states predicted by QCD. (A recent review is given in ref. Yo80.) Many of these states are predicted to be of fairly high spin. Several candidates have been reported, mostly in experiments where a polarization measurement has been used to enhance the signal from high spin resonances. Nonetheless, all of these are controversial since most are several 100 MeV wide and occur near production thresholds.

Recently, a candidate of unprecedented narrowness (40 MeV) was observed at Saclay in the disintegration of deuterium with unpolarized photons (Ar81). A π^- + proton pair were detected in coincidence with magnetic spectrometers, thus uniquely defining the kinematics of the reaction. For small values of the recoil momentum of the unobserved proton, the cross sections were completely consistent with the quasifree contribution (impulse approximation). However, at large recoil momenta, a pronounced structure was observed at about E_γ = 410 MeV. The ratio of the Saclay data to the calculation for quasifree scattering is plotted in Fig. 44. Since neither the beam nor the target was polarized, the spin of this structure is not known.

Measurements with polarized γ rays are needed to study the spin of this resonant structure. Furthermore, if the enhancement shown in Fig. 44 is indeed due to a Dibaryon, then several other such resonances should exist ;in the mass range from 2.15 to 2.35 GeV ($320 \leq E_\gamma \leq 530$ MeV). A search for such structures is planned for PHASE III of the project.

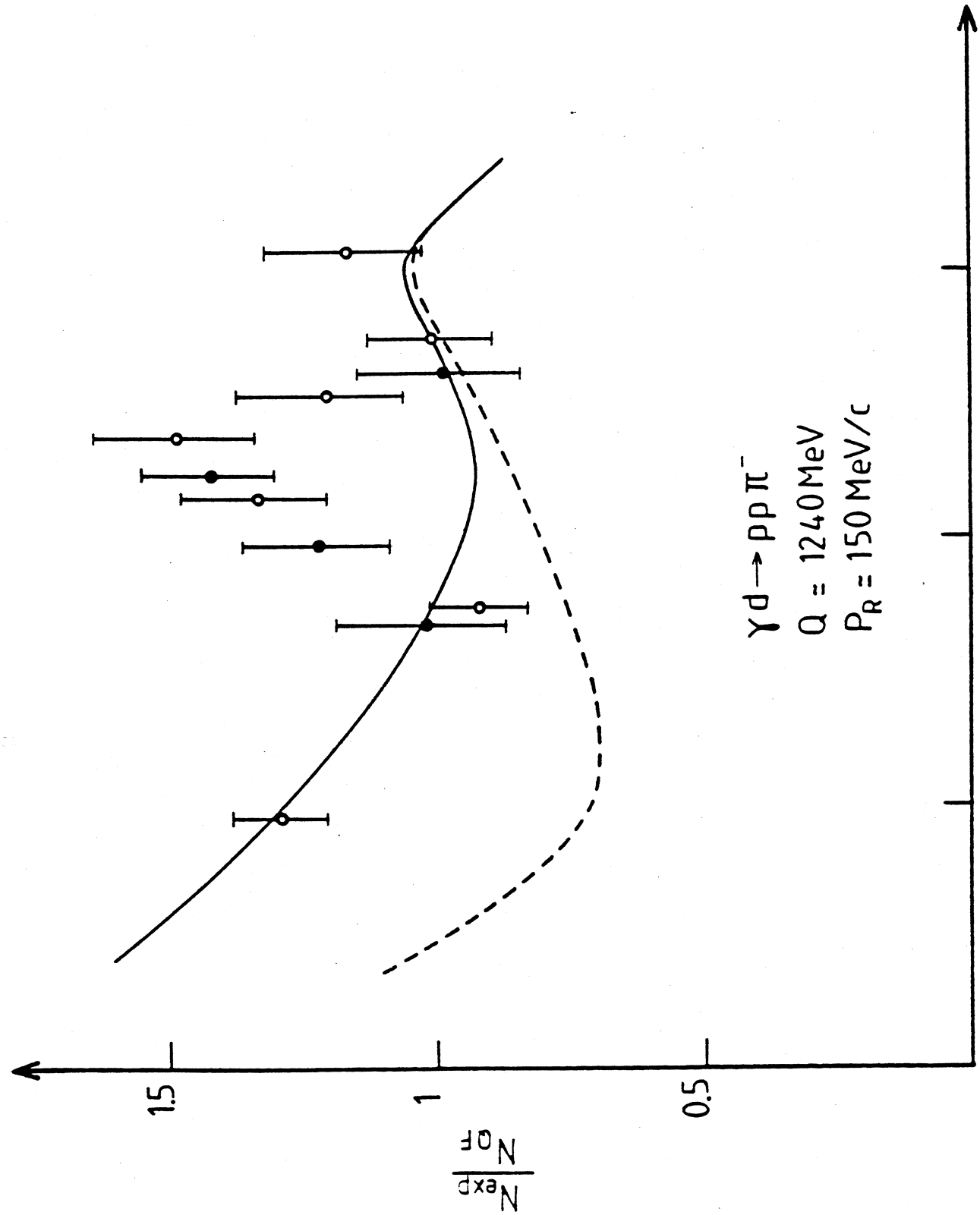

FIG. 44: The $^2H(\gamma,p\bar{\pi})$ cross section plotted relative to quasi-free $\gamma + n \rightarrow p + \pi^-$ production (Ar78).

IV.2 Experimental Considerations and Sample Counting Rates

For a reaction with a cross section $d\sigma/d\Omega$, the event rate from a target of mass number A and thickness T in a detector with an efficiency-solid-angle product $\varepsilon\Omega$ is

$$R(sec^{-1}) = (5.97x10^{-4})\frac{d\sigma}{d\Omega}(mb/sr)\varepsilon\Omega(sr)\frac{T}{A}(g/cm^2)\bar{\Phi}_\gamma(sec^{-1}), \quad (19)$$

when the photon flux is $\bar{\Phi}_\gamma$. Counting rate estimates from Eq. (19) for the experiments discussed in Section IV.1 are given below.

A. Elastic photon scattering from the delta

Collective enhancements in the region of the delta can occur only at large angles in (γ,γ). There, backgrounds from atomic processes are expected to be quite low, so that thick targets can be used. In the limiting case of a giant-delta resonance with maximal collectivity in ^{208}Pb (dashed curves of Fig. 31), the peak cross sections at either 60^o or 150^o would be about 1 mb/sr. Although the data would always be analyzed in the 2.7 MeV steps defined by the tagging spectrometer, binning the final results in 10.8 MeV intervals of γ ray energy is sufficient to study this problem. In the standard operation with $2x10^7$ tagged photons in the full 175 MeV to 300 MeV range, there would be $1.7x10^6$ γ rays per second in this 10.8 MeV interval. For a target of one radiation length (6.3 g/cm^2 for Pb), the scattered rate into a spectrometer with an effective solid angle of 28.6 msr (APPENDIX B) would be $\underline{1\ sec^{-1}}$. In the complete absence of an "giant" component to the delta (solid curves of Fig. 31), the predicted cross sections are a factor of about 300 lower. This

situation would produce about 1 count every 6 minutes, so that data with 10% statistics could still be accumulated in 10 hours.

The cross sections for elastic photon scattering from lighter nuclei decrease roughly with Z^2. Furthermore, targets of one radiation length become impractically long because of their decreased density. For example, for $^{12}C(\gamma,\gamma)$ measurements, the maximum useful target thickness is about 8 g/cm^2. The scattering cross sections for θ_γ between 60^o and 120^o are expected to be about 30 nb/sr in the absence of any collective enhancements (Mo82). This would produce a scattered flux of about 2 hour^{-1} in a 10.8 MeV interval of γ ray energy, requiring 50 hours of data taking to obtain 10% statistics. Since the data would be collected over the full dynamic range from 175 MeV to 300 MeV simultaneously, such running time requirements are not excessive. The existence of a giant-delta resonance in ^{12}C could enhance the cross section by up to 2 orders of magnitude, and lead to corresponding reductions in running time.

B. Total Photoabsorption measurements

The total photonuclear absorption cross section of light nuclei such as ^{16}O is about 6 mb (Fig. 34) in the region of the Δ, while the atomic photoabsorption is about 600 mb (Ah75). To ensure efficient rejection of atomic events (APPENDIX A), target thicknesses would be limited to about 0.01 radiation lengths (0.36 g/cm^2 for H_2O). In the standard mode of operation there would be an average of 4.3×10^5 photons in each 2.7 MeV inteval of γ-ray energy defined by the tagging spectrometer. Since the efficiency of the absorption detector is unity (APPENDIX A), the nuclear absorption by ^{16}O would produce

35 events-sec^{-1} in each 2.7 MeV interval. At the same time the absorption detector must contend with a total rate of 160 KHz from atomic processes. This is not expected to pose any problems for the system described in APPENDIX A.

There is no available data in the region of the delta for nuclear absorption by targets heavier than ^{16}O. Nonetheless, the cross sections should increase roughly with A so that, for ^{208}Pb, 25 mb might be reasonable near 300 MeV (Fig. 31a). However, the atomic absorption increases only slightly slower than Z^2 (Ah75). This might strain the atomic rejection system described in APPENDIX A, were it not for the constraint to limit the target thickness to 0.01 radiation lengths. For ^{208}Pb this corresponds to 0.06 g/cm^2 and, with the standard flux of 2×10^7 tagged photons, would again produce a total rate of about 160 KHz from atomic processes. At the same time, the nuclear absorption rate would be 1.9 sec^{-1} in each 2.7 MeV interval of photon energy.

C. Coherent π^o photoproduction

From Figs. 37 and 38, the cross section for the coherent process $^{12}C(\gamma,\pi^o)^{12}C^{g.s.}$ at 240 MeV is about 100 μb/sr in the region of θ_{π^o} between 20° and 60°. Since the π^o is detected by its decay into 2 γ rays, the target could be relatively thick. However, an extended source would introduce an additional uncertainty in the opening angle of the γ rays, and hence in the resolution of the π^o. For this experiment, a target of about 2 g/cm^2 is optimal. For 240 MeV photons, the kinetic energy of the π^o is about 100 MeV, and the corresponding efficiency-solid-angle product of one of the π^o

spectrometers is 1.25 msr (TABLE CV-APPENDIX C). The coherent components would be extracted by analyzing the data in the 2.7 MeV steps defined by the tagging spectrometer, although the final results could again be combined into 10.8 MeV intervals. The flux of 1.7×10^6 photons-sec^{-1} in each of these 10.8 MeV intervals during standard operation leads to a data rate of 1.3 events per minute in each interval. Measurements at large angles would of course take longer (Figs. 37 and 38).

D. Critical Opalescence in (γ, π^+)

The enhancement from the opalescence effect shown in Fig. 40 is strongest at about 90° where the cross section for the $^{12}C(\gamma, \pi^+)$ reaction is expected to be about 1 μb/sr, and the π^+ energy is about 100 MeV. The efficiency-solid-angle product of the pion spectrometer (APPENDIX D) for T_π=100 MeV is 34.6 msr. The energy loss of 100 MeV pions in carbon is 1.8 MeV/g-cm^{-2}. The energy resolution near 90° will be determined by the pion energy loss across the horizontal extent of the photon beam (~1 cm). To minimize this effect, an active target (plastic scintillator), segmented in 1 mm layers parallel to the beam, can be utilized to reduce the pion energy loss contribution to <0.2 MeV. When combined with the 1.1 MeV intrinsic resolution of the spectrometer and the 2.7 MeV spread of the photon beam, this leads to a net π resolution of 2.9 MeV. This will allow the excitation energy in the final ^{12}B to be determined with a modest accuracy. Combining the final data in 10.8 MeV intervals of excitation energy, each containing an average of 1.7×10^6 photons-sec^{-1} in the standard operating mode, leads to a data rate of 21 events per hour, using a

target which is 2 g/cm^2 thick to the beam. Thus, 10% statistics can be accumulated in 5 hours. In the absence of an opalescence effects, the 90^o cross sections would be about an order of magnitude lower, and 2 days would be required to obtain a comparable accuracy. The contribution of pions from hydrogen in the scintillator is expected to be very small in the region of coherent production from ^{12}C. [The $^{12}C(\gamma,\pi^-)^{14}N$ reaction should manifest the same sensitivity to critical opalescence, and is completely free from contributions due to hydrogen.] If a possible opalescence effect were observed, other reactions such as $^{10}B(\gamma,\pi^-)^{10}C$ or $^{14}N(\gamma,\pi^+)^{14}C$ for which the pion resolution is sufficient to separate decays to the ground states of the residual nuclei, could be investigated with a narrower target and longer running times.

E. (γ,γ)-Delbrück scattering

The largest deviations (Mo60) between measured and calculated values for Delbrück scattering have been observed at medium energies (~100 MeV) and very forward angles, $\theta_\gamma \sim mc^2/E_\gamma$. To minimize nuclear scattering from the delta, these measurements would best be done at the lower end of our energy range, E_γ~200 MeV, where mc^2/E_γ would correspond to 2.5 mrad. This is an order of magnitude larger than the divergence of the photon beam. With the pair spectrometer of APPENDIX A positioned 10 meters from the target, γ rays from Delbrück scattering could be measured at angles down to 1 mrad. The reduced efficiency of a thin-radiator + pair-spectrometer as a γ-ray detector ($\varepsilon\Omega$~0.1 msr) is more than compensated by the large forward angle cross sections: ~100 b/sr from a Uranium target (Mo60). Thus, even when an

0.01 radiation length target (0.05 g/cm^2 for ^{238}U) is used to reduce shower production, the counting rate in a 10.8 MeV interval of γ ray energy during standard operation would still be ~2 sec^{-1}. At larger angles where the Delbrück amplitudes are considerably smaller ($\theta_\gamma > 1^o$) the high efficiency NaI-based spectrometers of APPENDIX B could be used.

F. Asymmetry in $(\vec{\gamma}, e^+e^-)$ from Neutral Currents

The addition of a quarter-wave plate to the laser optical transport (Fig. 19) will allow production of circularly polarized γ rays, although only the highest energy photons will be completely polarized. In the standard mode of operation, the flux in the two highest energy-resolution intervals of γ ray energy (292.6 MeV < E_γ < 298.0 MeV) is about 10^6 sec^{-1}. Pair production cross sections can be measured with the magnetic spectrometer of APPENDIX A. With an 0.5 radiation length target, an average of about one e^+e^- pair will be produced per photon. The helicity of the γ ray beam can be flipped with a polarization rotator in the laser optical system. If the production asymmetry with right (R) and left (L) circularly polarized photons $A=(d\sigma_R - d\sigma_L)/(d\sigma_R + d\sigma_L)$ is near the Weinberg-Salam-Glashow (WSG) limit of ~10^{-5}, then 10^{12} events are needed for a 10% statistical accuracy. This is accumulated in about 278 hours. Running times much longer than this are rather impractical. However, if the two orders of magnitude enhancement over the WSG prediction reported by Ziegler (Fig. 43) is indeed due to neutral currents, the pair-production asymmetry should become apparent very quickly.

G. Dibaryon structures in $^2H(\vec{\gamma},p\pi^-)P$

The resonance structure observed at Saclay with $E_\gamma \simeq 400$ MeV is displayed in Fig. 44 in terms of the quasi-free $\gamma+n \rightarrow p+\pi^-$ cross section. From Ref. (Ar78), this converts to a pion production cross section of about 25 μb/sr for the kinematic conditions of Fig. 44. In these measurements, a bremsstrahlung spectrum was used, so that both energy and angle determinations for both detected particles were necessary to reconstruct the energy of the photon that initiated the decay. Two magnetic spectrometers were used in these measurements (Ar81) with solid angles of 3.36 msr for the pions and 2.25 msr for the protons, respectively. For the conditions of Fig. 44, the pions carry away about 150 MeV of kinetic energy. The spectrometer of APPENDIX D has a solid angle that is more than an order of magnitude larger than the Saclay detector, 37.7 msr at T_π=150 MeV. Furthermore, since the energy of the γ rays from the proposed facility are known by tagging, the proton energy will not have to be measured. To determine the kinematics, it is sufficient to measure the proton angle. This can be done with large area multiwire proportional counters: $\Delta\theta \sim 45^\circ$, $\Delta\phi \sim 40^\circ$ with a net solid angle of about 425 msr. This will allow data over a large range of P_R (the momentum of the unobserved proton) to be collected simultaneously. The liquid-deuterium target is being designed and constructed at Frascati. From previous experiences (Ar75), an effective target thickness of 1 g/cm^2 is readily achievable. This thickness also keeps the energy loss of the protons and pions down to a reasonable level. With the PHASE III flux of 10^6 photons-sec^{-1} in a 10.8 MeV interval, the net coincidence counting rate will be about <u>40 per hour</u> in each interval of the dynamic range extending up to 480 MeV.

IV.3 Experimental Equipment

The medium-energy physics experiments outlined in the previous sections have been designed around existing experimental hardware. No major new pieces of equipment will be required for this initial research program. The existing high-energy γ-ray spectrometers are described in APPENDIX B. They would be utilized not only in photon scattering measurements, but also as the key elements of two independent π^o spectrometers (APPENDIX C). An existing large acceptance dipole magnet (transferred to BNL from the SREL facility) along with two large aperture quadrupoles (obtained from the AGS at BNL) would be used for the charged pion spectrometer described in APPENDIX D. Another large acceptance dipole magnet (also obtained from SREL) would be utilized in the pair spectrometer described in APPENDIX A. The rest of the components necessary to complete an absorption detector (APPENDIX A) will be supplied by Frascati National Laboratories.

As outlined in Section V, the costs required to complete these spectrometers are very minimal. Nonetheless, the designs for each of the detector systems described in the appendices represent much more than the premium utilization of existing hardware. In each case they reflect a significant improvement over current detector technology. When combined with the unique γ-ray beams from the proposed facility, they are expected to yield a diversified and very fruitful program of medium-energy research.

APPENDIX A: Absorption Detector

Measurements of total photoabsorption cross sections with the proposed facility can be carried out by simply counting the number of tagged photons reaching the target that are not transmitted through the target. Not all of the tagged flux will reach the target area. Some will lie outside the acceptance of the γ-beam defining collimator (#2 in Figs. 25 and 26). For a given collimation, the fraction of tagged flux that does reach the target is dependent upon the angular divergence of the electrons in the interaction straight. This fraction is shown as a function of collimator half-angle in Fig. 16 for the OPTICS tune. For absorption measurements it is necessary to reject those tagged photons that do not reach the target, and this will be done by using a single active Pb-glass collimator at the position of #2 in Figs. 25 and 26 (#1 will not be used here) to define the γ-ray beam. A tagged electron in anticoincidence with this active collimator signals the arrival of a photon of known energy at the target. An additional anticoincidence with a γ ray detector after the target signals an absorption event.

The total photoabsorption cross section is the sum of atomic and nuclear components, $\sigma^{TOT} = \sigma^{At} + \sigma^{Nu}$, and it is only the nuclear absorption σ^{Nu} that is of interest here. However, the contribution from atomic processes σ^{At} is always much larger than σ^{Nu}. For example, at E_γ=300 MeV the nuclear absorption cross sections on ^{16}O is about 6 mb (Fig. 34), while the atomic cross section is 600 mb (Ah75). The low background and small size of the γ ray beams from the proposed facility, accompanied by tagging signals for all γ rays that strike

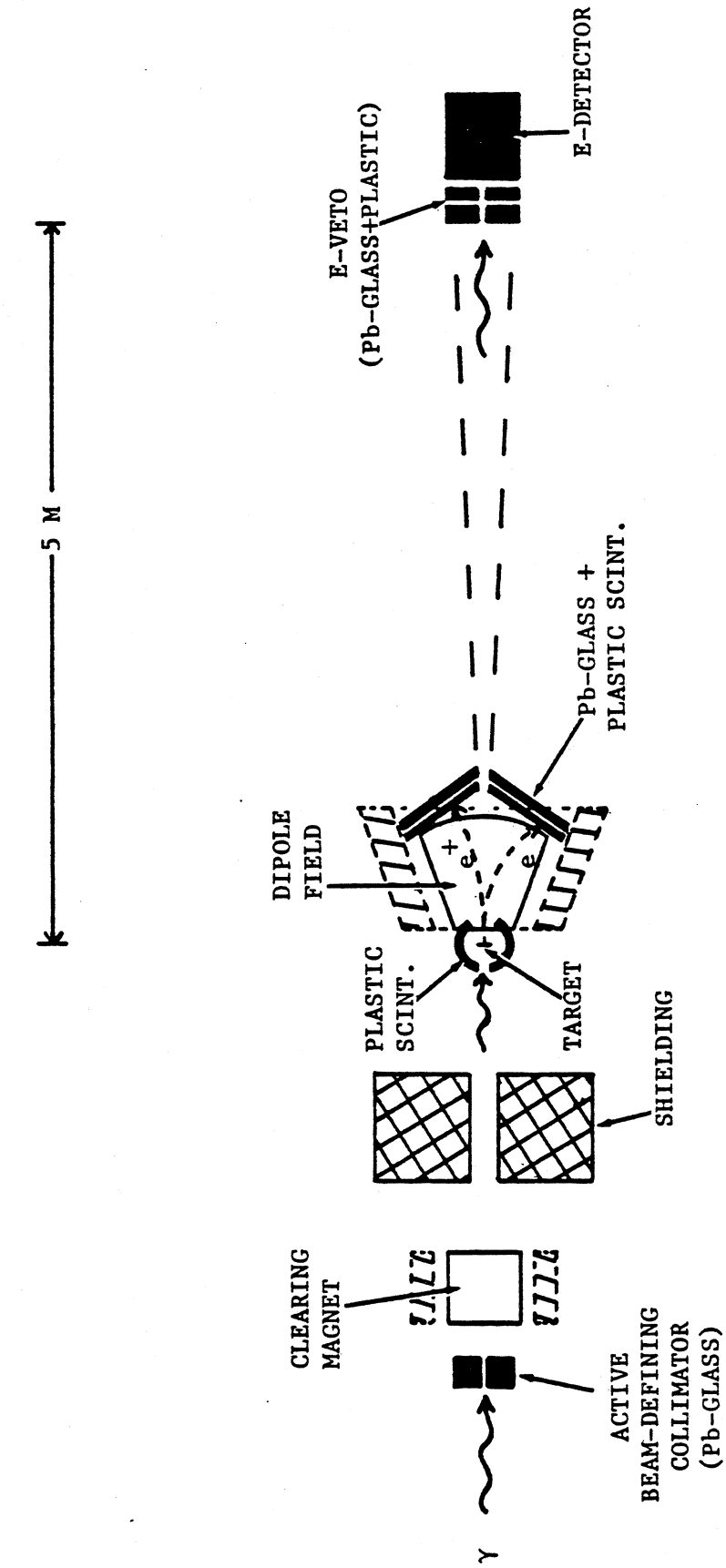

FIG. A1 : ABSORPTION DETECTOR

the target, will permit the electronic rejection of atomic absorption events with an efficiency sufficient to yield a direct measurement of σ_{Nu}.

The planned absorption detector is shown schematically in Fig. A1. The counter labeled E-VETO consists of Pb-glass and plastic scintillator disks with coaxial holes just big enough to pass the primary γ-ray beam. A photon that has passed through the target without interaction will trigger the Pb-glass total energy E-detector in anticoincidence with E-VETO.

In the energy range of the proposed facility atomic absorption in the target occurs mostly through pair production, with a small additional contribution from Compton scattering. The angular distribution of e^+e^- pairs produced by high energy γ rays is extremely forward peaked. A Monte-Carlo calculation of the e^+/e^- distribution created by 100, 200, and 300 MeV photons traversing one radiation length of lead is shown in Fig. A2. The mean opening angle of the pairs decreases with increasing photon energy, from $\pm 1.2^{\circ}$ at 100 MeV to $\pm 0.7^{\circ}$ at 300 MeV. A large aperture dipole magnet (0.4 m horizontal acceptance with an 0.4 m gap) immediately follows the target. Electrons and positrons emerging within $\pm 14^{\circ}$ are deflected by the magnetic field and detected in coincidence on opposite sides of the γ-ray beam axis with Pb-glass and plastic scintillators. At photon energies between 100 and 500 MeV an average of one e^+e^- pair is created in 0.5 radiation lengths (Lo75). Thin targets, about 0.01 radiation lengths, would be used to eliminate multiple pair production and reduce multiple scattering to an acceptable level. These target thicknesses drastically reduce the bremsstrahlung of the e^+e^- pairs and effectively prevent the generation of a cascade shower.

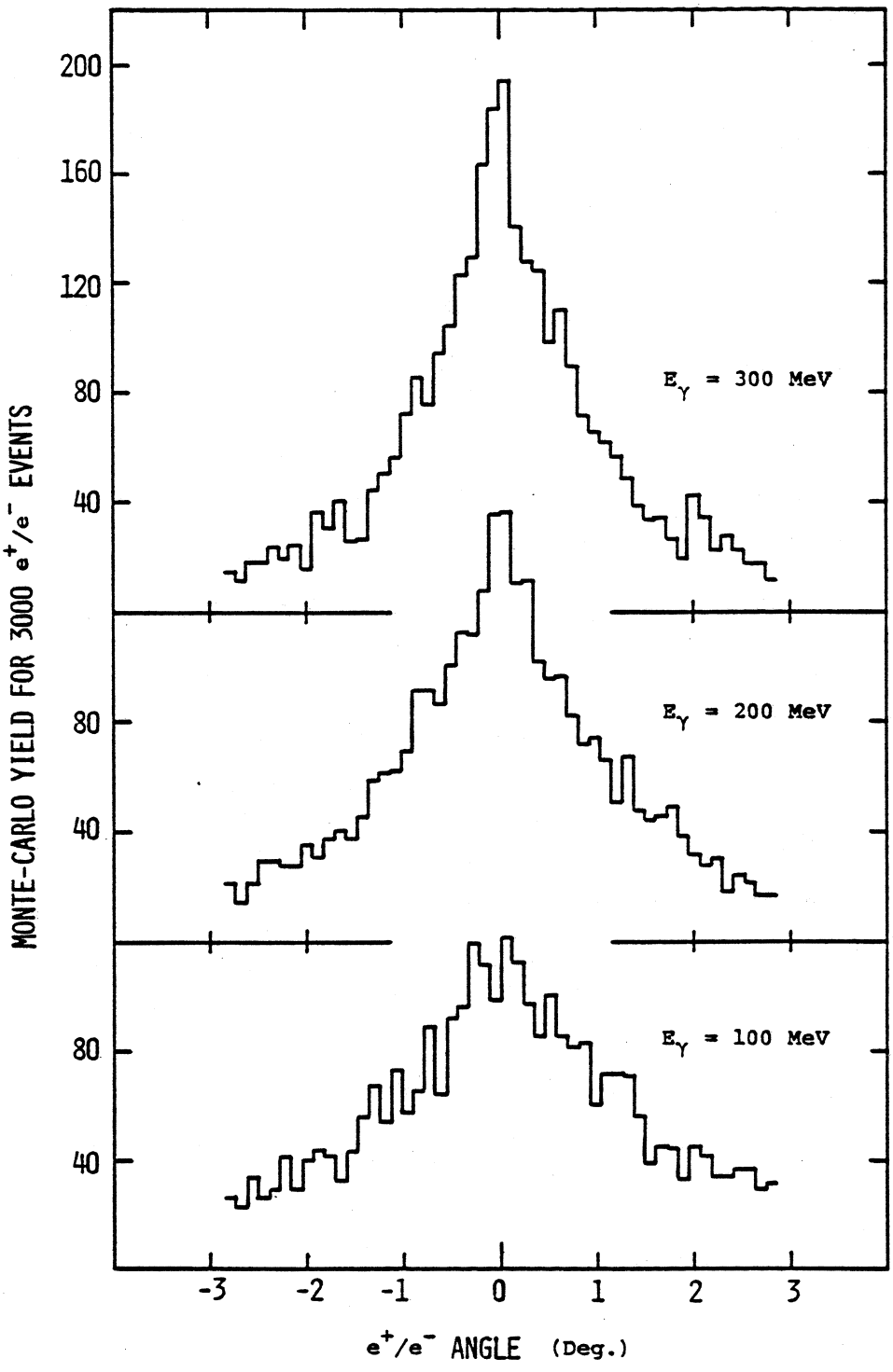

FIG. A2: Monte-Carlo calculation of the angular distribution of electrons and positrons, pair-produced by high-energy gamma rays in one radiation length of Pb.

Atomic Compton scattering is also very forward peaked, with a FWHM of $\pm 2.3^{\circ}$ at 300 MeV. Although the Compton cross section is much smaller than that of pair production, it is still comparable to or greater than the nuclear absorption of interest and must be effectively rejected. Most of the Compton scattered γ rays will strike the E-VETO counter. Those emitted at large angles are very low in energy ($E_{\gamma}<4$ MeV for $\theta_{\gamma}>30^{\circ}$) and will be detected in plastic scintillators surrounding the target (Fig. A1). The only atomic Compton events that cannot be rejected are those that pass through the 0° hole in the E-VETO detector. To minimize the number of such events, one can make use of the fact that the Compton scattering distribution is diverging from the target very much faster than the primary photon beam. In particular, with the photon beam collimation and the E-VETO detector aperture chosen from the minimum divergences of the OPTICS tune (Fig. 13), $\theta_x = 2.4\times10^{-4}$ rad and $\theta_y = 5\times10^{-5}$ rad, and with the E-VETO detector located 5 meters from the target and 30 meters from the center of the laser-electron interaction region, the unobservable Compton scattering through the E-VETO hole is $Z(1.4\times10^{-4})$ mb. This is negligible, even for targets of relatively high Z.

The true nuclear absorption events result almost entirely in the production of protons, neutrons, and charged pions. The charged particles will produce signals in the counters designed to reject atomic absorption. However, they can be readily distinguished from electrons and photons by their energy losses in plastic and Pb-glass. The only events which will not appear in the resulting atomic-rejected nuclear absorption cross section σ^{Nu} are those involving nuclear photon scattering. However, these form a very small part of σ^{Nu}

(less than 1%) and can be neglected. The signature of the various possible events in the detectors of Fig.A1 are sufficiently unique that, for the most part, hardware cuts and fast electronic coincidences will be sufficient to select out nuclear absorption. For events not satisfying these constraints, energy signals from all of the detectors of Fig. A1 would be recorded for off-line analysis. The rate of such ambiguous events is expected to be quite low, enabling this absorption detector to utilize the maximum available tagged flux.

APPENDIX B: Gamma Ray Spectrometers

The Brookhaven MARK-III spectrometer represents the current state of the art in high energy gamma ray detectors. An exploded view of this spectrometer is shown in Fig. B1. Photons from the target are collimated by a lead aperture onto a high resolution large volume (24x36 cm) NaI(Tl) crystal. This detector has been fabricated by Bicron Corp., using new techniques developed in conjunction with BNL. The NaI is housed in a 1 cm thick ^{6}LiH neutron shield and surrounded by 10 cm of plastic scintillator, used in anticoincidence to reject cosmic rays and events where part of the high energy shower produced by a γ ray escapes from the NaI. The plastic shield is split into a slab in front of the NaI and an array of 6 optically isolated sections that are contained in a common thin-walled stainless steel cylinder. Active transistor-stabilized bases on each of the seven NaI phototubes compensate for fluctuations in counting rate, and a monitoring system controls the conditions under which gain corrections are automatically applied. In addition, pulses of light from an externally stabilized LED are distributed to each photomultiplier tube by a system of fiber optics, and an active amplifier is used to correct for variations in the position of this peak due to this light.

The response of this detector to isolated high energy γ rays in the 20 to 50 MeV range is shown in Fig. B2. The indicated line width represents an improvement of almost a factor of 2 over the previous generation of γ ray spectrometers. The stabilization electronics maintains this resolution as well as the system gain (to 0.1%) at extremely high counting rates (~1 MHz). The dependence of the resolution upon γ-ray energy is shown in Fig. B3. Above 15 MeV the

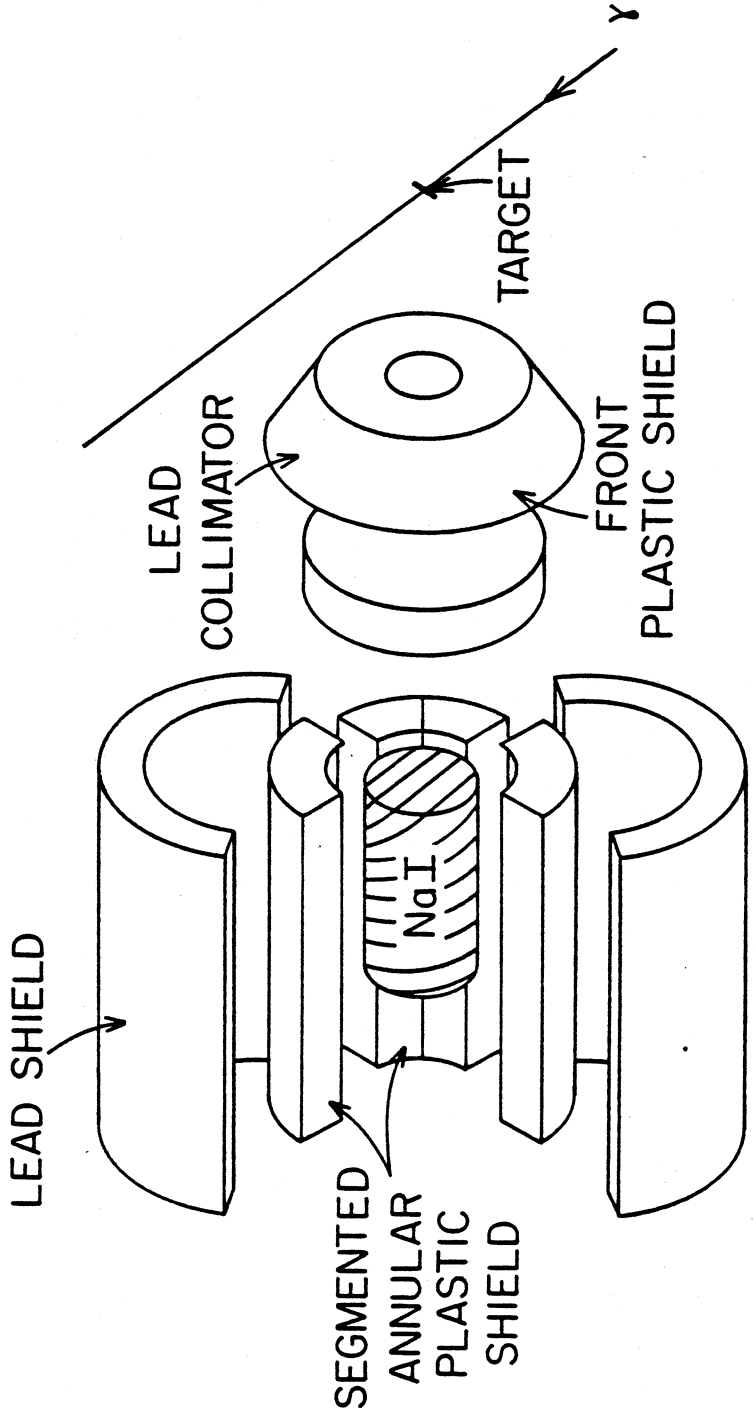

FIG. B1: Exploded view of the BNL-MARK III high energy γ-ray spectrometer.

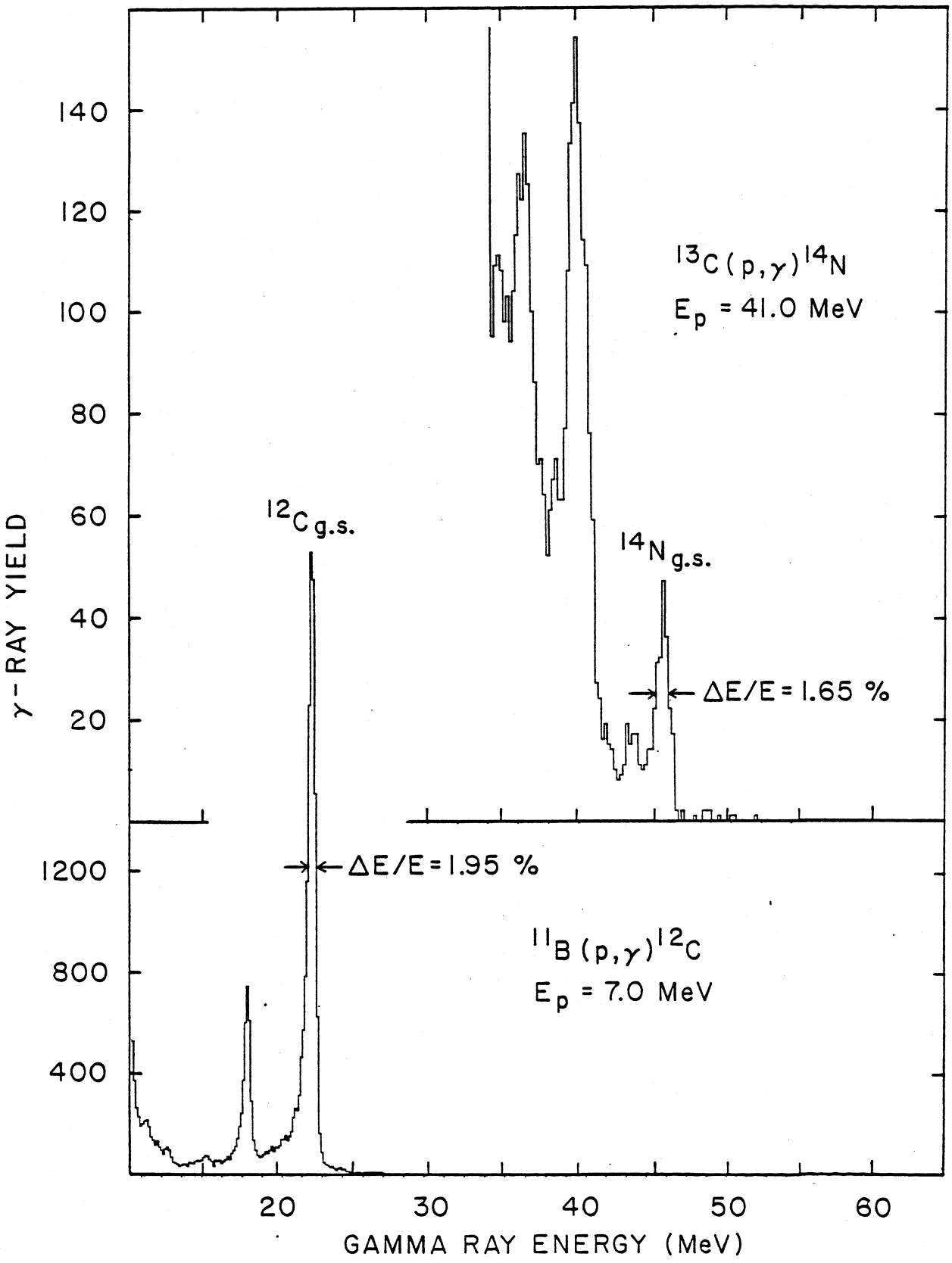

FIG. B2: Response of the BNL-MARK III spectrometer to isolated high-energy gamma rays.

resolution improves with $(E_\gamma)^{-1/3}$. The line shapes of Fig. B2 are asymmetric because the plastic anticoincidence shield is not 100% efficient. Thus some γ ray showers, in which either bremsstrahlung or 511 keV annihilation radiation escapes the NaI, are not rejected. At lower energies ($E_\gamma \lesssim 12$ MeV) the one-escape peak is resolved as a separate line. This line merges into the primary peak at higher energies. If the higher energy γ ray lines are treated, not as single peaks but as unresolved doublets, primary and one-escape, with the position of the one-escape fixed at .511 MeV below the primary, and with its area fixed at that fraction of the primary (15%) determined from lower energy measurements where the two are resolved, then the resolution of the primary peak decreases with $(E_\gamma)^{-1/2}$ over the measured range from 15 to 45 MeV. This indicates that the resolution of this detector is limited entirely by photon statistics (contrary to popular folklore).

Extrapolations of the curve of Fig. B3 to 300 MeV predict resolutions of about 0.8%. An $(E_\gamma)^{-1/2}$ dependence would predict an even lower value. A continuing improvement with higher energy has been reported with the SPEAR-Crytal-Ball detectors (Ch77), that are only slightly deeper (40 cm) than the BNL MARK-III crystal. Their energy resolution decreases as $(E_\gamma)^{-1/4}$ up to the GeV range, although their starting point at 50 MeV is very much worse (6% FWHM).

We expect a continued superior performance of the BNL MARK-III detector at high energies. To be conservative in planning the medium energy physics program, we have assumed that its resolution does not improve but rather remains constant at the value of 1.65% measured at E_γ=45 MeV. Even at this level, the resolution is quite adequate while the efficiency-solid-angle product, measured as 28.6 msr at 45 MeV, is

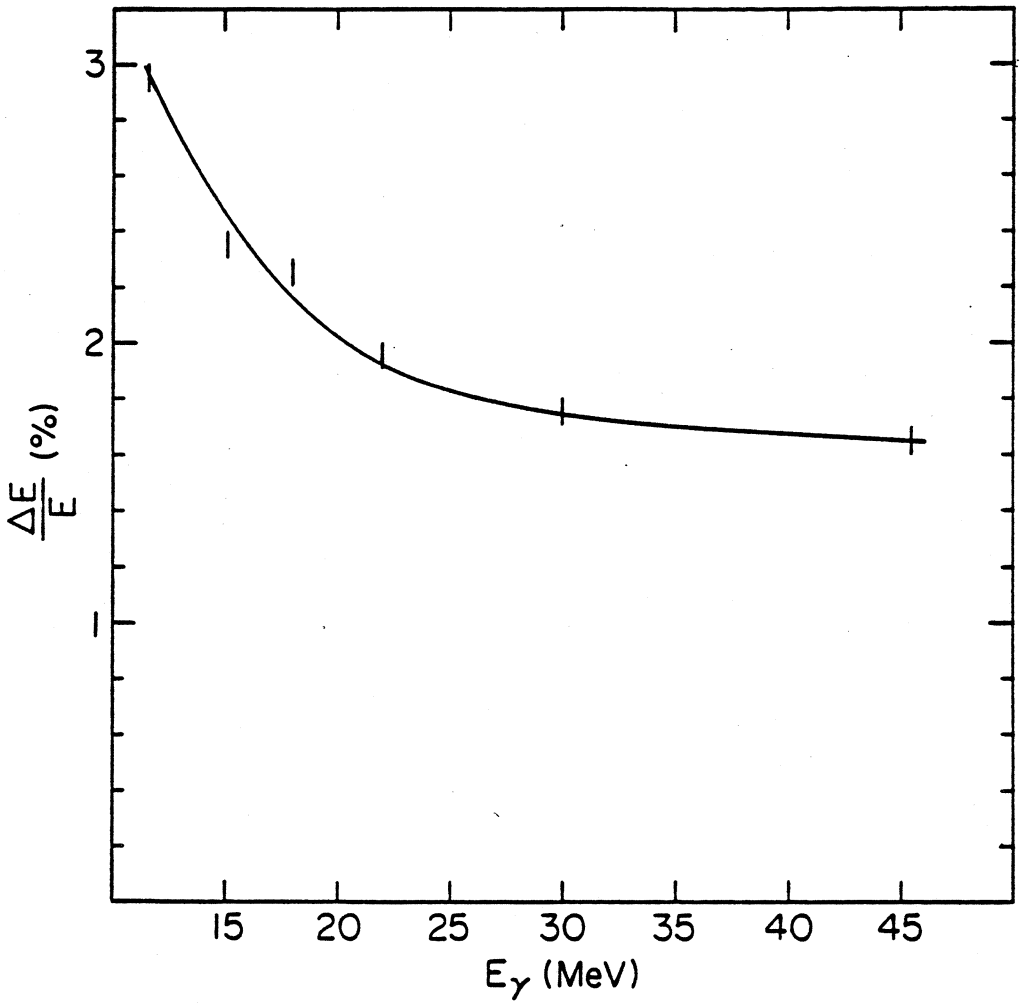

FIG. B3: Resolution of the BNL-MARK III spectrometer as a function of gamma-ray energy.

very much larger than can be achieved with a pair spectrometer.

The BNL MARK-II detector is identical to the MARK-III except for the NaI crystal itself. The MARK-II achieves only 3.2% resolution at 20 MeV. This crystal will be replaced by a MARK-III-caliber detector in PHASE III, thus completing two state-of-the-art high-energy γ-ray spectrometers.

APPENDIX C: π^o-Spectrometer

The π^o decays instantaneously ($\tau_{\pi^o} = 0.84 \times 10^{-16}$ sec) into 2 isotropic gammas which have a relative angle of 180^o and equal energies in the rest frame of the π^o. The Lorentz transformations substantially modify the lab energies of the γ rays, even at very modest pion kinetic energies. The "forward" gamma (closest to the pion momentum $\vec{P}_\pi$) is doppler shifted up and carries most of the total pion energy,

$$E_\pi = T_\pi + 135 \text{ MeV}, \tag{C1}$$

while the associated "backward" γ ray carries very little of this energy. The photon energies are given by

$$E_\gamma = \frac{E_\pi}{2}(1+\beta\cos\Theta), \tag{C2}$$

and their laboratory angles by

$$\tan\theta = \frac{\frac{1}{\gamma}\sin\Theta}{\cos\Theta+\beta} \tag{C3}$$

where βc is the pion velocity, γ the Lorentz factor, and Θ, θ are the angles of the gamma ray in the pion rest frame and in the laboratory, respectively, measured relative to the π^o direction. The extreme values of Eq. (C2), which occur when $\Theta = 0^o$ or 180^o, are listed for a few pion energies in TABLE CI.

In the past, two different strategies have been used to detect the π^o decay gammas. The first, due to Baer (Bae81) looks at the decay gammas which are emitted at equal angles in the laboratory. The

TABLE CI: Extreme decay gamma ray energies which occur when the photons are emitted along $\vec{P}_{\pi}$:

T_{π^o} (MeV)	$E_{\gamma_1}(0^o)$ (MeV)	$E_{\gamma_2}(180^o)$ (MeV)
20	116	39.4
50	156	29.2
100	214	21.3
200	321	14.2

TABLE CII: Performance parameters for the Baer-type (Bae81) π^o spectrometer for R=50 cm:

T_{π^o}	$\Omega g \cdot P_x^*$ (geometric acceptance in msr)	Ω_{eff} (msr)	ΔE_{π^o} (FWHM in MeV)
50	2.4	0.53	1.5
100	2.2	0.49	1.8
200	2.2	0.49	3.3

*P_x is the fraction of coincident gammas which satisfy the energy-sharing cut $|x| \leq 0.1$.

gamma energies are measured in Pb-glass calorimeters to a precision of ~30% (FWHM). The gamma directions are determined by wire chambers (MWPCs) which follow Pb-glass shower converters. The poor resolution energy measurement is used, in this strategy, only to ensure that the two photon energies are not very different, i.e.,

$$|X| = \frac{E_1 - E_2}{E_1 + E_2} < 0.1 \qquad (C4)$$

The decay kinematics can be written in terms of the energy sharing, X, and the laboratory angle between the 2 gammas, η:

$$(E_{\pi^o})^2 = \frac{2(m_{\pi^o})^2}{(1-\cos\eta)(1-X^2)} \qquad (C5)$$

This cut on X places all of the burden of the pion energy measurement on an accurate measurement of the opening angle, η. In Table CII, some of the performance parameters expected for a Baer-type spectrometer are listed, for the case of R=50 cm, the distance to the front face of each detector arm. The effective solid angle is taken from the geometric acceptance of Fig. 9 in Ref. (Bae81), reduced to account for converter and wire plane efficiencies following Eq. 24 of (Bae81).

The second strategy is that of Bowles, et al. (Bol81). In this approach, the opening angle η is constrained to the vicinity of 180^o, the forward gamma being detected by a Pb-glass calorimeter, and the backward gamma by a large NaI spectrometer. In this geometry, the partition of energy between the γ rays is roughly that of TABLE CI and the pion energy resolution is given by

$$\frac{\Delta E\pi}{E_\pi} = \frac{-\beta\Delta E_\gamma}{E_\gamma} \qquad (C6)$$

Thus, the pion energy resolution is determined by the fractional energy resolution of the NaI detector. The performance characteristics of such a spectrometer are given in Table CIII, where a NaI spectrometer subtending a half angle of 10° ($\Delta\Omega_{eff}=\varepsilon\Delta\Omega=28.6$msr), and a Pb-glass detector subtending a half angle of 10° ($\Delta\Omega_{eff}=95$msr) have been assumed. The resolution of the NaI for the low energy γ ray was assumed to be 1.9%, from APPENDIX B.

We have considered several variations on these 2 strategies with the goal of retaining a good energy resolution with a greatly increased effective solid angle. There are two promising alternatives. The first utilizes the geometry of Bae81, but the Pb-glass detectors are now replaced by NaI spectrometers. However, unlike the Baer-type spectrometer, the angle η is not measured to high precision. Rather, the pion energy is constructed from the sum of the gamma energies. This approach has the effect of increasing the effective solid angle dramatically with increasing energy, as shown in Table CIV. Comparison with Table CII shows that the energy resolution is only slightly worse with this geometry.

Our second, and preferred, alternate geometry adapts that of Bowles, et al. (Bol81). Increasing the solid angle associated with the fore-aft geometry results in degraded energy resolution due to the uncertainty in opening angle η. Our solution to this problem is to detect the forward ($\sim 0^\circ$) high-energy gamma ray with a large NaI detector, subtending a half angle of 10°, with an effective solid angle of 28.6msr. The associated backward photon ($\sim 180^\circ$) detector

TABLE CIII: Performance of a Pb-glass (0^o) - NaI (180^o) Bowles-type (Bo181) spectrometer:

T_{π^o} (MeV)	$\Delta\Omega$ (msr)	ΔE_π(NaI) (MeV)	ΔE_π(angle) (MeV)	ΔE_{TOTAL} (MeV)
20	0.59	1.45	1.24	1.90
50	0.22	2.40	0.91	2.57
100	0.092	3.65	0.68	3.72
200	0.036	5.83	0.49	5.85

TABLE CIV: Performance of a symmetric angle spectrometer comprised of 2 NaI detectors. NaI energy resolution was assumed to be 1.6% (APPENDIX B), and the effective solid angles, $\Delta\Omega_{eff}$, were taken to be 28.6 msr.

T_{π^o} (MeV)	E_γ (MeV)	$\theta_1\theta_2$ (deg)	$\Delta\Omega_{Tot}$ (msr)	ΔE_{π^o} (MeV)
20	78	60^o	0.60	1.75
50	92	47^o	0.92	2.08
100	118	35^o	1.55	2.67
200	168	24^o	3.06	3.80

would be a thin plate of NaI (half-angle = 45^{o}) which measures position in a manner similar to that of an Anger camera (An67). This arrangement is shown schematically in Fig. C1. A doppler-shift correction would be applied to the high energy γ rays, based on the angle measurements from this low energy detector. The remaining uncertainty in angle is limited to the 10^{o} acceptance of the forward detector. The performance of such a spectrometer is given in Table CV. (The energy resolution of the "forward" NaI detector is assumed to be 1.6% - APPENDIX B.)

The energy resolution for this proposed spectrometer is equal to, or slightly better than, that of the design of Bae81. The solid angle is almost an order of magnitude larger than that of either Bae81 or Bol81. The solid angle for this design (TABLE CV) complements our alternate symmetric angle geometry in that it is largest at low energies, while the solid angle of the spectrometer of Table CIV is larger for high pion energy.

In view of the interest here in moderate energy pions, the second proposed design (Table CV) is clearly the most suitable. Furthermore, the use of the existing high-resolution NaI spectrometers described in APPENDIX B, makes the cost of implementing this pion spectrometer very nominal. Only two angle measuring "180^{o}" detectors will be required to complete two independent π^{o} detectors.

π° SPECTROMETER

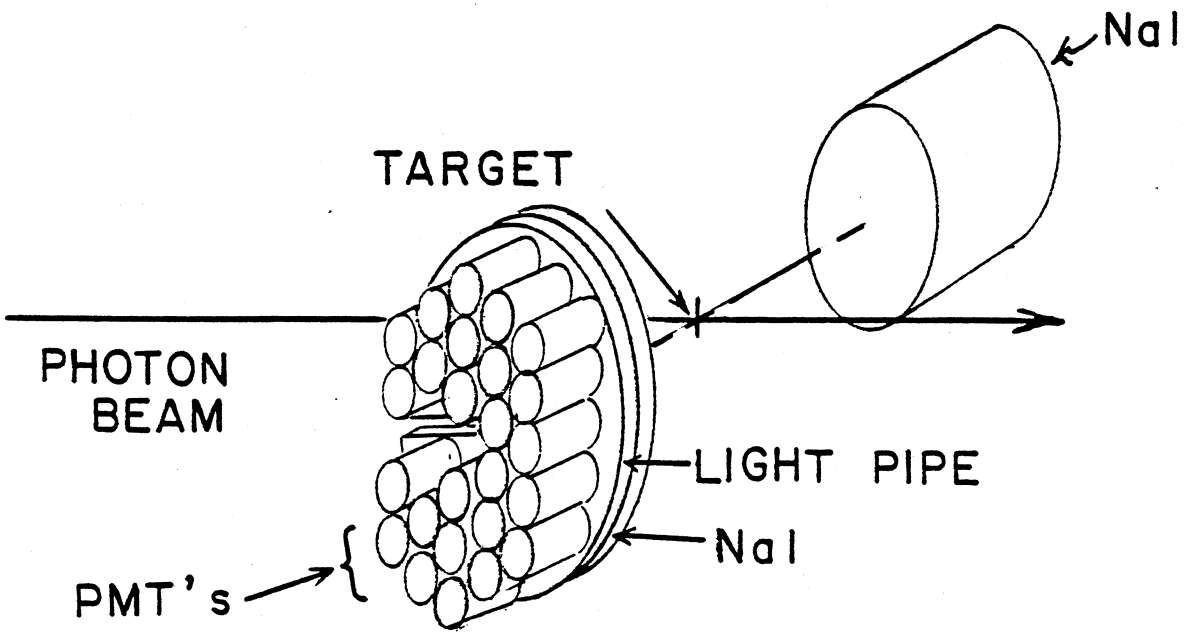

FIG. C1: A schematic representation of the π° spectrometer. The 24 cm x 36 cm NaI crystal is shown without its plastic anticoincidence annulus. The rear angle-measuring counter is comprised of a NaI plate, light pipe and an array of photomultipliers. The notch in the rear assembly allows measurements at extreme forward angles.

TABLE CV: Performance of a fore-aft spectrometer using a high resolution NaI (at~0^{o}) to measure gamma energy, and a position-sensitive NaI crystal (at ~180^{o}) to measure angle. Position determination from the latter is assumed to be $<<10^{o}$.

T_{π^o} (MeV)	E_γ(forward) (MeV)	$\Delta\Omega_{eff}$ (msr)	ΔE_{π^o} (MeV)
20	116	3.84	1.26
50	156	1.90	2.04
100	214	1.25	3.09
200	321	0.48	4.92

APPENDIX D: $\pi^{\pm}$ Spectrometer

A design for a charged-pion spectrometer has been completed. This design utilizes existing large aperture magnetic elements, and provides a momentum resolution of 0.68% at a solid angle of 50 msr, over a momentum range of 10%.

A layout of this QDQ spectrometer is shown in Fig. D1. The second quadrupole, which is a current-sheet device with a large rectangular aperture similar to the design of (Ha59), makes possible the QDQ arrangement which is responsible for the large solid angle achieved here. The efficiency of the device is determined by the fraction of pions which traverse the 4 m path length from the target to the focal plane without decay. The resulting effective solid angle is shown in Table DI.

Calculations for this design were performed with the code TRANSPORT (Br70). The spectrometer solid angle is determined by a $\Delta\theta = \pm 50$mr, $\Delta\phi = \pm 250$mr geometrical acceptance. The limiting charged particle envelopes in the x (dispersive) and y (transverse) directions are shown in Fig. D2. The important matrix elements relevant to this design are listed in Table DII. The resolving power, in first order, is determined by the ratio of the dispersion to the product of magnification and spot size on target: $D/(MX_{target})=205.3$, for $X_{target}=1$ cm. As can be seen from Table DII, the contribution from the second-order term $(x|\theta^2)$ dwarfs the image size calculated in first order. This aberration can be corrected by ray-tracing. In order to reduce the second order term so that its contribution is equal to the first-order spot size, an angular resolution at the entrance to the

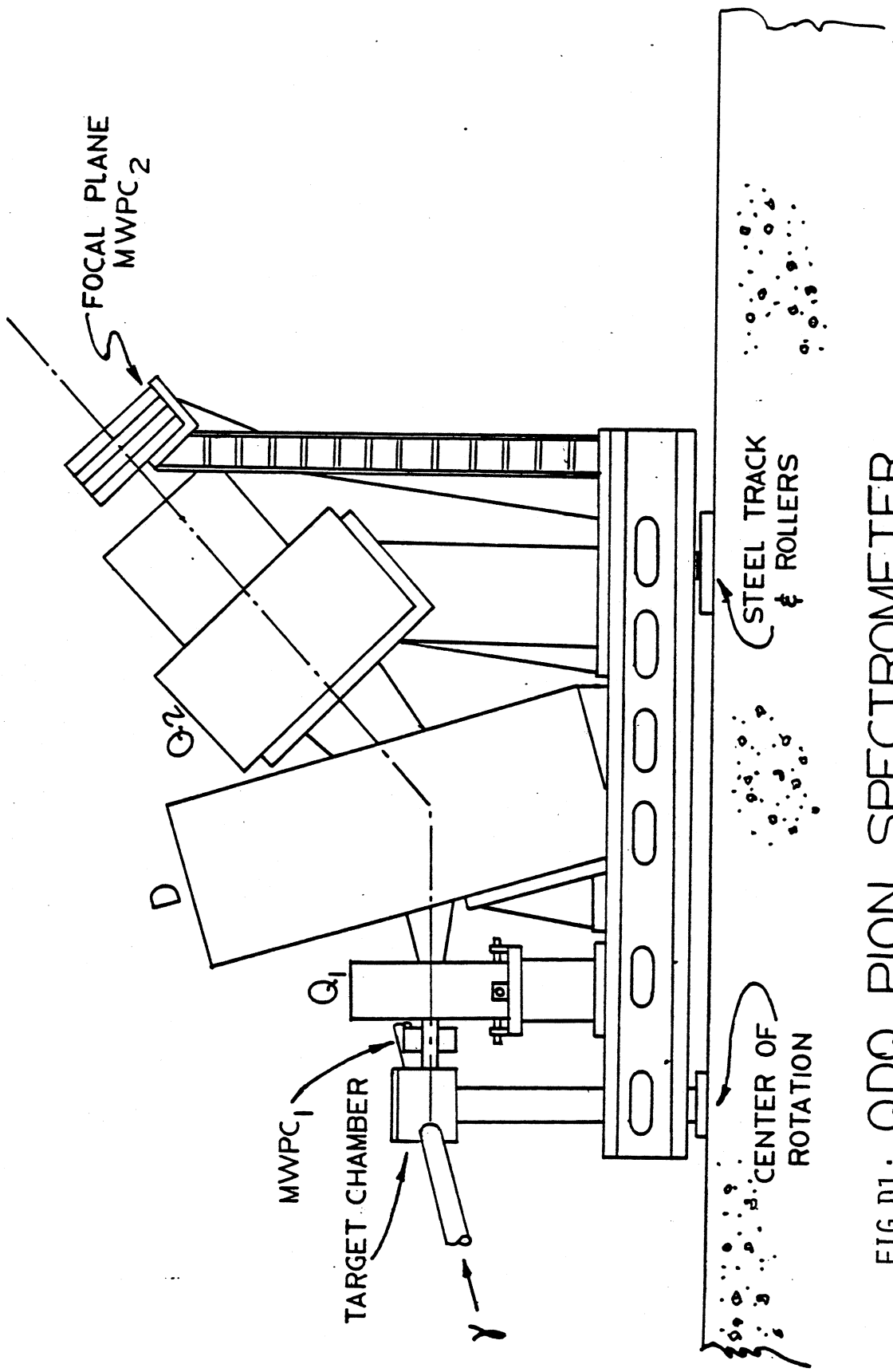

FIG.D1: QDQ PION SPECTROMETER

TABLE DI: Energy resolution and efficiency of the QDQ spectrometer for several values of the pion kinetic energy.

T_π(MeV)	p(MeV/c)	$\varepsilon \cdot \Delta\Omega$(msr)	ΔE(MeV)
25	87.2	22.0	0.31
50	128.3	28.6	0.59
75	163.0	32.2	0.84
100	194.7	34.6	1.08
150	253.7	37.7	1.51
250	363.7	41.1	2.31

TABLE DII: Transport matrix elements for the QDQ spectrometer. A target spot size of 1 cm has been assumed in the last column. Units are cm, mr, %.

Element	Calculated Value	Contribution to Spot Size (cm)
$(x\|x) \equiv M$	-0.226	0.226
$(x\|\delta) \equiv D$	0.464	---
$(x\|\theta^2)$	-4.22×10^{-4}	1.06
$(x\|x^2)$	-0.105	2.6×10^{-2}
$(x\|\phi^2)$	-2.87×10^{-6}	0.18
$(x\|\theta\delta)$	5.78×10^{-3}	---
$(y\|y)$	-18.6	---
$(\phi\|\phi)$	-0.211	---

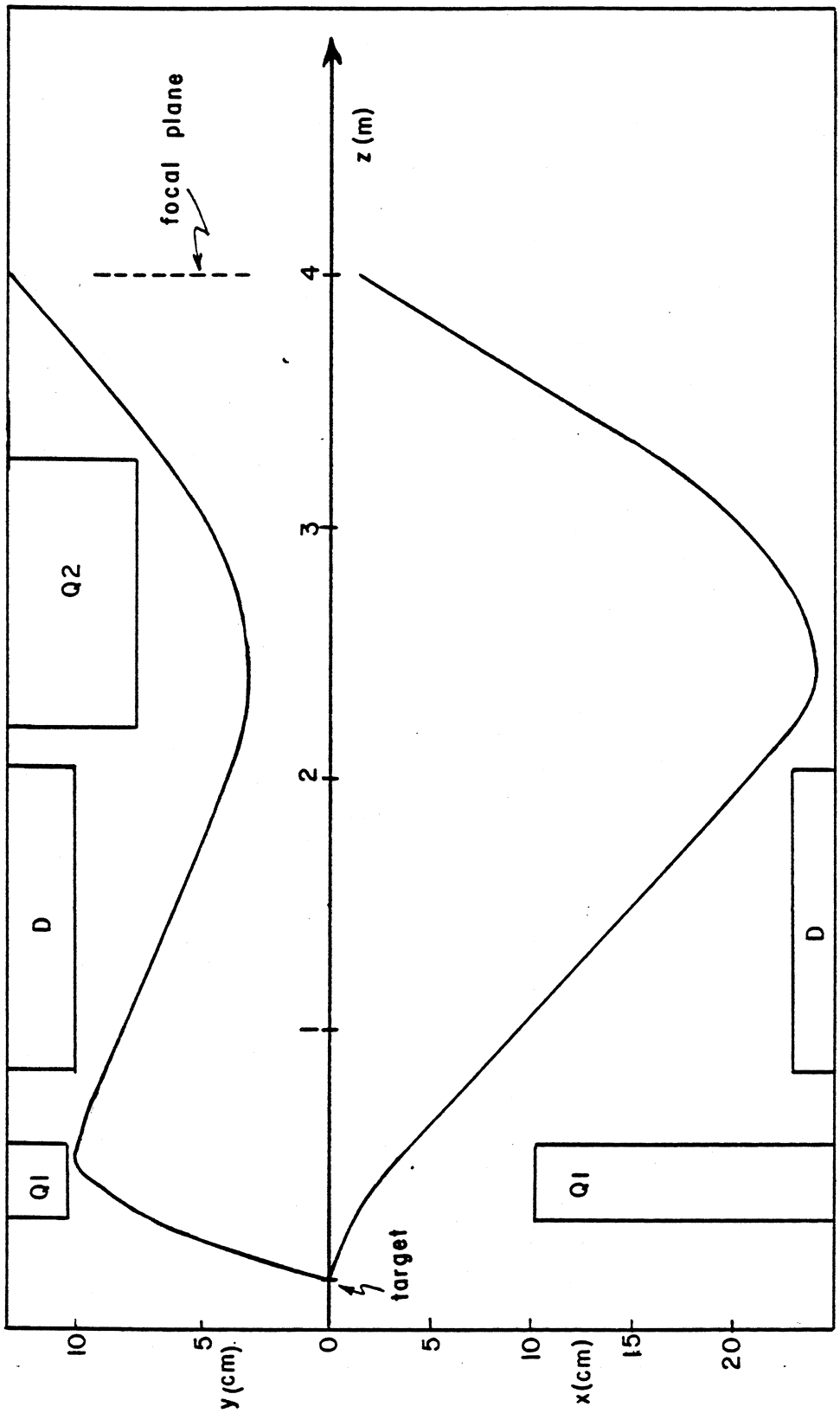

FIG. D2: Beam envelopes for the QDQ spectrometer, calculated to second order, for $\Delta\theta = \pm 50$mr, $\Delta\phi = \pm 250$mr, $\Delta p/p = 0$.

spectrometer of $\Delta\theta=0.3^{o}$ is required. However, angles measured near the focal plane are larger than those at the target by the inverse of the horizontal magnification, 1/M. Thus, the angular accuracy required at the exit of the spectrometer is 1.3^{o}. This will be measured by two multiwire proportional counters (MWPC's). (Multiple scattering in the first MWPC windows introduce errors of only 0.1^{o}). Similarly, ray tracing to determine $\Delta\phi$ can be done to sufficient accuracy to make the $(x|\phi^{2})$ term vanish. As can be seen from Fig. 2, the MWPC's required are of modest dimensions, 30 cm (y) by 5 cm (x), with resolution $\simeq$0.1 cm (x) by 0.5 cm (y), and are sufficient for the required ray tracing assuming a 30 cm separation between planes. The momentum resolution, resulting from this system, $\Delta p/p=0.68\%$, has been used to calculate the pion energy resolution shown in the last column of Table DI. This resolution is limited by the spot size on target. If necessary, the resolution can be improved by decreasing the γ-ray beam defining apertures, although not without a reduction in flux (Fig. 16).

The effect of path length differences through the spectrometer ($\pm$12 cm) is negligible, yielding a contribution to the time resolution of <2 nsec FWHM.

Some of the muons from the in-flight decays of the pions will reach the focal plane. To reject such events, a pair of wire chambers will be installed at the entrance to the spectrometer, allowing the angles θ and ϕ to be measured to $<1^{o}$ (FWHM). Since the muons lie within a 10^{o}-30^{o} cone of the initial pion momentum, most of them can be vetoed by comparing angles at the entrance and exit of the spectrometer. The multiple scattering resulting from these additional

detectors is estimated to be ~0.15°. Taking into account the horizontal magnification, this spread translates to ~0.75° at the focal plane. This angular uncertainty is small compared with the 1.3° necessary to correct the higher-order aberrations.

The dipole and quadrupole elements assumed in this design are all available at BNL. Only the vacuum chamber, a mechanical support for the spectrometer, and the focal plane detectors remain to be constructed.

REFERENCES

(Ah75) J. Ahrens, H. Borchert, K.H. Czock, H.B. Eppler, H. Gimm, H. Gundrum, M. Kröning, P. Riehn, G. Sita Ram, A. Zieger, and B. Ziegler, Nucl. Phys. A251, 479 (1975).

(An67) H.O. Anger, in "Instrumentation in Nuclear Medicine", Vol. 1, 485 (ed. G.J. Hine), Academic Press, New York (1967).

(Ar63) F.R. Arutyunian and V.A. Tumanian, Phys. Lett. 4, 176 (1963).

(Ar75) P.E. Argan, et al., Nucl. Phys. A237, 447 (1975).

(Ar78) P.E. Argan, et al., Nucl. Phys. A296, 373 (1978).

(Ar81) P.E. Argan, et al., Phys. Rev. Lett. 46, 96 (1981).

(Ar82) J. Arends, private communication.

(Ba69) J. Ballam, et al., Phys. Rev. Lett. 23, 498 (1969).

(Ba77) T. Bar-Noy and S. Kahane, Nucl. Phys. A288, 132 (1977).

(Ba78) C. Baltay, Proc. 19th Int. Conf. on High Energy Physics, (Tokyo, 1978), pg. 882, eds. S. Homma, et al.

(Ba80) D.E. Bainum, et al., Phys. Rev. Lett. 44, 1751 (1980).

(Ba81) B. Banerjee, N.K. Glendenning, and M. Gyulassy, Nucl. Phys. A361, 326 (1981).

(Bae81) H.W. Baer, et al., Nucl. Inst. Meth. 180, 445 (1981).

(Bai77) P. Baird, M. Brimicombe, R. Hunt, G. Roberts, P. Sandars, and D. Stacey, Phys. Rev. Lett. 39, 798 (1977).

(Be65) C. Bemporad, et al., Phys. Rev. 138B, 1546 (1965).

(Be80) H. Beil and R. Bergere, Saclay Report No. CEA-N-2144 (1980).

(Be82) B.L. Berman, R. Bergere, P. Carlos, Phys. Rev. C26, 304 (1982).

(Bj64) J.D. Bjorken and S.D. Drell, "Relativistic Quantum Mechanics", McGraw Hill Co. (1964).

(Bl81) J.P. Blewett, L. Blumberg, A.J. Campillo, R.P. DiNardo, H.D. Hsieh, S. Krinsky, A. Luccio, C. Pellegrini, J. Schuchman, P.Z. Takacs, A. van Steenbergen, IEEE Trans. Nucl. Sci. NS28, 3166 (1981).

(Bo81) A. Bohr and B.R. Mottelson, Phys. Lett. 100B, 10 (1981).

(Bo82) J.D. Bowman, private communication.

(Bol81) T.J. Bowles, et al., Phys. Rev. C23, 439 (1981).

(Br70) K.L. Brown and S.K. Howry, SLAC report No. 91 (1970).

(Br81) G.E. Brown, Nucl. Phys. A358, 39C (1981).

(Ca82) P. Carlos, H. Beil, R. Bergere, B.L. Berman, A. Lepretre, and A. Veyssiere, Nucl. Phys. A378, 317 (1982).

(Ce73) CERN-Gargamelle Collaboration, Phys. Lett. 46B, 121 (1973).

(Ch77) Y. Chan, et al., Proc. "Nuclear Science Symp. on Scintillation and Semiconductor Counters", San Francisco (1977).

(Ch80) P. Christillin, in Proc. of the Workshop on "Intermediate Energy Nuclear Physics with Monochromatic and Polarized Photons", Frascati (1980), p. 88.

(Cl74) A.S. Clough, et al., Nucl. Phys. B76, 15 (1974).

(Co74) J.S. Colonias, "Particle Accelerator Design: Computer Programs", Academic Press, N.Y., p. 15-39 (1974).

(Co79) R. Conti, P. Bucksbaum, S. Chu, E. Commins, and L. Hunter, Phys. Rev. Lett. 42, 343 (1979).

(Da59) G. Davidson, Ph.D. thesis, Massachusetts Institute of Technology, 1959 (unpublished).

(De81) W. DelBianco, et al., Phys. Rev. Lett. 47, 1118 (1981).

(El76) L.R. Elias, W.M. Fairbank, J.M. Madey, H.W. Schwettman, and T.I. Smith, Phys. Rev. Lett. 36, 717 (1976).

(El80) R. Ellis and B. McKellar, J. Phys. G: Nucl. Phys. 6, 1 (1980).

(Fe48) E. Feenberg and H. Primakoff, Phys. Rev. 73, 449 (1948).

(Ga82) G.T. Garvey, private communication.

(Ge54) M. Gell-Mann, M.L. Goldberger, and W. Thirring, Phys. Rev. 95, 1612 (1954).

(Gl82) N. Glendenning and P. Hecking, LBL-14141 (1982); submitted to Physics Letters.

(Ha59) L. Hand and W. Panofsky, Rev. Sci. Inst. 30, 927 (1959).

(Hi77) M. Hirata, F. Lenz, and K. Yazaki, Ann. of Phys. 108, 16 (1977); M. Hirata, J. Koch, F. Lenz, and E.J. Moniz, Phys. Lett. 70B, 281 (1977); and Ann. of Phys. 120, 205 (1979).

(Hu80) M.G. Huber and K. Klingenbeck, Proc. Workshop on Intermediate Energy Nuclear Physics with Monochromatic and Polarized Photons, Frascati, 1980, (ed. by G. Matone and S. Stipcich).

(Ja62) J.D. Jackson. "Classical Electrodynamics," John Wiley & Sons, Inc. (1962).

(Ja76) C. Jarlskog and P. Salomonson, Nucl. Phys. B107, 285 (1976).

(Ja82) JADE Collaboration, W. Bartel, et al., Phys. Lett. 108B, 140 (1982).

(Jd80) J. Delorme, in Proc. of the Workshop on "Intermediate Energy Nuclear Physics with Monochromatic and Polarized Photons", Frascati (1980), p. 154.

(Jd81) J. Delorme, Nucl. Phys. A358, 73C (1981).

(JMa73) J.M. Madey, H.A. Schwettman, and W.E. Fairbank, IEEE Trans. Nucl. Sci. NS20, 980 (1973).

(JMa74) J.M. Madey, J. Appl. Phys. 42, 1906 (1974).

(Kl29) O. Klein and Y. Nishina, Z. Physik 52, 853 (1929).

(Ko79) J. Koch and E.J. Moniz, Phys. Rev. C20, 235 (1979).

(Ko82) J. Koch and E.J. Moniz, private communication.

(Kr79) S. Krinsky, in Proc. of the Workshop on Beam Current Limitations in Storage Rings, BNL(1979); BNL No. 26668.

(Ku64) O.F. Kulikov, et al., Phys. Lett. 13, 344 (1964).

(Ku82) M. Kutschera, Phys. Lett. 108B, 229 (1982).

(Le77) L. Lewis, J. Hollister, D. Soreide, E. Lindahl, and E. Fortson, Phys. Rev. Lett. 39, 795 (1977).

(Le81) R. Leicht, M. Hammen, K.P. Schelhaas, and B. Ziegler, Nucl. Phys. A362, 111 (1981).

(Le81) A. Lepretre, H. Beil, R. Bergere, P. Carlos, J. Fagot, A. de Miniac, and A. Veyssiere, Nucl. Phys. A367, 237 (1981).

(LK81) A. Luccio and S. Krinsky, in Proc. of Quantum Electronics Workshop, Sun Valley(1981) - to be published as "Free Electron Generators of Coherent Radiation" by Addison-Wesley (ed. S.F. Jacobs and G.T. Moore); BNL No. 30078.

(Lo75) E. Longo and I. Sestili, Nucl. Inst. and Meth. 128, 283 (1975).

(Lu81) A. Luccio, in Proc. of Quantum Electronics Workshop, Sun Valley(1981) - to be published as "Free Electron Generators of Coherent Radiation" by Addison-Wesley (ed. S.F. Jacobs and G.T. Moore); BNL No. 30108.

(Ma70) D. Maydan, J. Appl. Phys. 41, 1552 (1970).

(Ma77) G. Matone, et al., Lecture Notes in Phys. 62, 149 (1977); G. Matone, Proc. Workshop on Intermediate Energy Nuclear Physics with Monochromatic and Polarized Photons, Frascati, 1980, (ed. by G. Matone and S. Stipcich); L. Federici, et al., Il Nuovo Cimento 59B, No. 2, 247 (1980).

(Ma82) MARK-J Collaboration, B. Adeva, et al., Phys. Rev. Lett. 48, 1701 (1982).

(Me79) B.A. Mecking, Lect. Notes in Phys. 108, 382 (1979).

(Mi63) R.H. Milburn, Phys. Rev. Lett. 10, 75 (1963).

(Mi82) J. Miller, private communication.

(Mo60) J. Moffat and M.W. Stringfellow, Proc. Roy. Soc. A254, 242 (1960).

(Mo82) E.J. Moniz, private communication.

(NS82) "NSLS DESIGN HANDBOOK", available from the National Synchrotron Light Source, Brookhaven National Laboratory; and S. Krinsky, private communication.

(Ol80) O.E. Olsen, H.A. Olsen, and P.G. Flo, Phys. Rev. D22, 2132 (1980).

(Os79) E. Oset and W. Weise, Nucl. Phys. A319, 477 (1979).

(Os81) E. Oset and W. Weise, Nucl. Phys. A368, 375 (1981).

(Pa68) G. Palazzi, Rev. Mod. Phys. 40, 611 (1968).

(Pa75) P. Papatzacos and K. Mork, Phys. Reports 21C, 81 (1975).

(Pe80) C. Pellegrini, in Proc. of the Int. School on Quantum Electronics, Erice(1980) - to be published by Plenum Press.

(Pr78) C.Y. Prescott, et al., Phys. Lett. 77B, 347 (1978).

(Re78) A. Renieri, in Proc. of the Enrico Fermi School of Phys., LXXIV, Varenna (1978) - published by North Holland in 1980 (ed. C. Pellegrini).

(Re79) A. Renieri, IEEE Trans. Nucl. Sci. NS26, 3827 (1979).

(Ro80) H. Rost, Ph.D. thesis, University of Bonn, 1980 (unpublished).

(Sa68) L.M. Saunders, Nucl. Phys. B7, 293 (1968).

(Sa81) A.N. Saharia and R.M. Woloshyn, Phys. Rev. C23, 351 (1981).

(Sc82) B. Schoch, private communication.

(Se81) K. K. Seth, Proposal to the Centre d'Etude Nucleaire de Saclay to "Measure the Longitudinal Quadrupole Transition Probability for the Electron Induced Transition: Nucleon Delta", Depart. of Physics, Northwestern University, Illinois (1981).

(Sp82) J. Speth, S. Krewald, F. Osterfeld, and T. Suyuki, Proc. of Int. Symposium on "Nuclear Fission and Related Collective Phenomena and Properties of Heavy Nuclei", Bad Honnef (Oct. 26-29, 1981); to appear in Lect. Notes in Phys.

(Ta80) M. Tannenbaum, Proc. of "Symp. on High Energy Physics with Polarized Beams and Polarized Targets", Lausanne, Switzerland (1980).

(Ta82) TASSO collaboration, R. Brandelik, et al., Phys. Lett. 110B, 173 (1982).

(Th81) C.E. Thorn, C. Chasman, and A.J. Baltz, IEEE Trans. on Nucl. Sci. NS28, 2089 (1981).

(va80) A. van Steenbergen, XIth Int. Conf. on High Energy Accelerators, Geneva, Switzerland, July 1980; BNL #28013.

(We73) W. Weise, Phys. Rev. Lett. 31, 773 (1973).

(We81) W. Weise, Nucl. Phys. A358, 163C (1981).

(Wo78) R.M. Woloshyn, Phys. Rev. C18, 1056 (1978).

(Yo80) A. Yokosawa, Phys. Reports 64, 47 (1980).

(Zi79) B. Ziegler, Lect. Notes in Phys. 108, 382 (1979).

(Zi82) B. Ziegler, Z. Phys. C (1982) - accepted for publication.

V. Time Schedule and Cost Estimates

The goals of this project, as outlined in section I.2, divide the activity into three distinct phases, each of which culminates in specific milestones for the development of the high-energy γ-ray facility. In PHASE I the 300-MeV tagged-γ-ray beam is developed and tested with preliminary scattering and aborption measurements. In PHASE II the NSLS building is extended to provide a γ-ray lab area, spectrometers are erected, and medium-energy physics begins in earnest with an ultra-high-power laser. In PHASE III the coupling of the VUV and X-RAY storage rings is developed to provide up to 500 MeV tagged photons. The approximate time schedule for the various components of these three phases is given in TABLE IV. There is some temporal overlap, particularly between PHASES II and III when the Free Electron Laser transport is being constructed and tested.

The capital expenditures for the different phases of this project, including the production of the tagged γ-ray beams as well as the instrumentation required for the medium-energy physics program, are summarized in TABLE V.

The scientific staff members currently involved in this project are listed in Section I.3, together with their affiliation. It is our desire to attract a larger body of users from the international medium-energy and photonuclear communities, and this will undoubtedly occur as the high-energy γ-ray beam becomes available. In particular, it is expected that additional members of the LADON collaboration in Frascati, other than those listed in Section I.3, will take part in some of the medium-energy physics experiments during the latter stages of this project.

TABLE IV. APPROXIMATE TIME SCHEDULE

PHASE I

	01/83	4/83	7/83	10/83	1/84	4/84	7/84	10/84	1/8
TAGGING SPECTROMETER	|	CONSTRUCTION		| INSTALL					
MODIFIED VACUUM BOXES		| CONSTRUCTION	| INSTALL |						
LASER			| TEST |		| INSTALL |			
γ ABSORPTION DETECTOR		| CONSTRUCTION |			| INSTALL |			
γ RAY PRODUCTION					| 1st BEAM |				
PHASE I EXP.					| 1st σ(ABS,) EXP.,	1st $\sigma(\gamma,\gamma)$ EXP. |			
EXTERNAL γ LAB						| CONSTRUCTION |			

PHASE II

MOVE TO γ LAB

TABLE IV. TIME SCHEDULE (CONT.)

PHASE II

	10/84	1/85	4/85	7/85	10/85	1/86
ULTRA HIGH POWER LASER	| TEST & INSTALL |					
γ SPECTROMETERS		| INSTALL |				
PHASE II EXP.			| $\sigma(\gamma,\pi^+)$, $\sigma(\gamma,\pi^0)$, DELBRÜCK SCATT., $(\vec{\gamma},e^+e^-)$ |			

PHASE III

FEL OPTICAL TRANSPORT	| TEST |		| INSTALL |			
γ RAY PRODUCTION FROM COUPLED STORAGE RINGS				| BEAM TESTS |		
PHASE III EXP.					| σ(ABS), ^{2}H(γ,Pπ) |	

To maintain an effective utilization of the unique capabilities of the proposed facility, the BNL-based staff will increase during the second and third phases of development. The BNL operating budgets for FY83, 84 and 85 are summarized in TABLE VI. Support for the salaries and travel expenses of our INFN-Frascati collaborators is provided by an ongoing grant from the Italian government.

TABLE V: CAPITAL EXPENDITURES* (1982 DOLLARS)

1st Year Costs	
Laser (SP171) modifications[1]	$ 18K
Optical transport	46K
Microprocessor controls for optics	16K
Modifications to X-RAY ring vacuum system	26K
γ-ray beam line and vacuum system	56K
Tagging spectrometer line and vacuum system	46K
Tagging spectrometer magnets	95K
Tagging spectrometer power supplies (magnets, septa and cooling pumps)	55K
Modifications to ring-Sextapole return yoke	18K
Microprocessor control for dipole supplies, septa and trim coils[2]	14K
Tagging electron focal-plane counter and electronics	47K
γ-ray collimator clearing magnets and power supplies	24K
γ-ray beam dump magnet and supply	9K
Two angle-measuring (Anger-type) NaI detectors to complete π^o spectrometers	44K
Data acquisition computer with CAMAC interface	35K
CAMAC electronics	22K
	$571K

2nd Year Costs	
Ultra-high power laser (SP921-171 with beam combiner)	$160K
FEL optical transport and associated controls	76K
Extended beam line, scattering chambers and vacuum system	35K
Mount for π^o spectrometers[3]	14K
Mount for $\pi^{\pm}$ spectrometer[3]	28K
$\pi^{\pm}$ spectrometer power supplies (Dipole and quadrupoles)	177K
$\pi^{\pm}$ detectors and electronics (entrance-angle wire chambers and focal plane counters)	68K
Computer expansion (additional memory, tape drive and hard copy units)	27K
	$585K

*Funds on the order of $300K will be requested separately for modifications to the NSLS experimental area to provide for the expanded γ-ray lab.

TABLE V (continued)

3rd Year Costs	
Large area proton detector	$ 28K
Electronics	20K
High resolution NaI crystal	42K
Cryogenic Handling system for Liquid-^{2}H target[4]	45K
	$135K

[1] Initial Ar-Ion Laser supplied by Frascati National Laboratories is tuned for the visible line at 5145Å and requires a new plasma tube for UV operation at 3511Å.

[2] Tagging spectrometer magnets must be off during injection and, once the stored beam has reached 2.5 GeV, the magnets must be ramped up with the septa and trim coils in such a way as to maintain cancellation of the fringing fields in the vicinity of the stored beam.

[3] Based on existing BNL equipment (APPENDICES B, C, AND D).

[4] Liquid-^{2}H target supplied by Frascati National Laboratories.

TABLE VI: OPERATING COSTS (1983 DOLLARS)

FY83:	3	Scientists	
	1	Research Associate	
	1	Technician	
		Supplies and Miscellaneous	
			$350K
FY84:	4	Scientists	
	1	Research Associate	
	1	Technician	
		Supplies and Miscellaneous	
			$460K
FY85:	5	Scientists	
	1/2	Visiting Scientist	
	2	Research Associates	
	2	Technician	
		Supplies Miscellaneous	
			$625K

TABLE VI: OPERATING COSTS (1983 DOLLARS)

FY83:	3	Scientists	
	1	Research Associate	
	1	Technician	
		Supplies and Miscellaneous	
			$350K
FY84:	4	Scientists	
	1	Research Associate	
	1	Technician	
		Supplies and Miscellaneous	
			$460K
FY85:	5	Scientists	
	1/2	Visiting Scientist	
	2	Research Associates	
	2	Technician	
		Supplies Miscellaneous	
			$625K

TABLE VI: OPERATING COSTS (1983 DOLLARS)

FY83:	3	Scientists	
	1	Research Associate	
	1	Technician	
		Supplies and Miscellaneous	
			$350K
FY84:	4	Scientists	
	1	Research Associate	
	1	Technician	
		Supplies and Miscellaneous	
			$460K
FY85:	5	Scientists	
	1/2	Visiting Scientist	
	2	Research Associates	
	2	Technician	
		Supplies Miscellaneous	
			$625K

TABLE VI: OPERATING COSTS (1983 DOLLARS)

FY83:	3	Scientists	
	1	Research Associate	
	1	Technician	
		Supplies and Miscellaneous	
			$350K
FY84:	4	Scientists	
	1	Research Associate	
	1	Technician	
		Supplies and Miscellaneous	
			$460K
FY85:	5	Scientists	
	1/2	Visiting Scientist	
	2	Research Associates	
	2	Technician	
		Supplies Miscellaneous	
			$625K

TABLE VI: OPERATING COSTS (1983 DOLLARS)

FY83:	3	Scientists	
	1	Research Associate	
	1	Technician	
		Supplies and Miscellaneous	
			$350K
FY84:	4	Scientists	
	1	Research Associate	
	1	Technician	
		Supplies and Miscellaneous	
			$460K
FY85:	5	Scientists	
	1/2	Visiting Scientist	
	2	Research Associates	
	2	Technician	
		Supplies Miscellaneous	
			$625K